KU LEUVEN

FACULTY OF SCIENCE

Microlensing of Gravitational Waves in a field of Microlenses

Astha

Supervisor: Prof. Dr. Tjonnie Guang Feng Li
Department of Physics & Astronomy
Department of Electrical Engineering, KU Leuven

Thesis presented in
fulfillment of the requirements
for the degree of Master of Science
in Astronomy and Astrophysics

Academic year 2022-2023

Acknowledgement

During the course of my thesis, I have gained significant academic insights and personal growth. The journey has been marked by various challenges and achievements, and I extend my heartfelt appreciation to all those who have contributed to the fruition of this work.

Foremost, I am deeply thankful to my supervisor, Prof. Tjonnie Li. His invaluable guidance and perspectives have greatly influenced both the trajectory of this thesis and my own development as an independent researcher. His supervision has also granted me the opportunity to collaborate with numerous individuals, an experience that has enriched my understanding and horizons.

I wish to convey my sincere gratitude to Simon Yeung (affiliated with University of Wisconsin-Milwaukee, Milwaukee, WI 53202, US) for generously offering his time amidst his busy commitments to provide me with consistent guidance and constructive feedback throughout the project. His insights have been instrumental in refining the quality of my work and understanding of this subject. I am also very thankful to the PhDs and postdocs from IVS and the theoretical physics department for affording me the opportunity for discussions, as well as for offering their invaluable support and guidance whenever needed.

My appreciation extends to my fellow students, whose unwavering support has been a cornerstone of my journey. I am very grateful to my companions, especially Anirudh and Pieterjan, with whom I have engaged in illuminating discussions and shared memorable moments.

My deepest gratitude is reserved for my parents, Mrs. Anita and Mr. Jayendra Chaubey. Their unwavering faith in my capabilities has been a wellspring of motivation. Despite the geographical distance, I am constantly enveloped in the warmth of their blessings. I cannot overlook the support of my brother, Ganesha, whose humorous attitude has consistently maintained a positive atmosphere throughout this endeavor.

Finally, my gratitude extends to the wonderful universe, whose awe-inspiring beauty and complexity have consistently inspired and humbled me throughout the process.

Contribution Statement

The candidate developed and implemented the code to analyse the impact of microlensing by a population of microlenses on a strongly lensed gravitational wave signal from type 1 macroimage. The code has been developed using available code for microlensing by single microlens. The candidate performed all the analysis leading to the results, often inspired by the methodologies of the referenced papers and and created all figures unless explicitly mentioned otherwise. The work in the thesis is an independent study that draws inspiration from and builds upon prior literature studies. In addition to the code development and independent investigation, this work is an important contribution to the existing literature with the comprehensive and systematic analysis of the parameters being used for the quantification of the microlensing effects.

Scientific Summary

Just like electromagnetic waves, gravitational waves generated by binary black hole mergers are also subject to lensing by galaxy mass lens, called macrolens which can lead to the formation of multiple images/signals of the source. These signals on possible detection by the current gravitational wave detectors like aLIGO have exciting applications in the intrinsic and extrinsic parameter investigation. However, error in the same is heavily dependent on a clean environment devoid of systematic errors induced due to lensing by stellar mass objects, called microlensing. Therefore, this thesis aims to investigate and quantify the impact of a population of microlenses on the macrolensed signal from type 1 macroimage, which is signal from one of the images very likely to be formed in the event of macrolensing .

To achieve this, a code for simulating the population of microlenses around the Type 1 macroimage, extending the available code for microlensing by for single microlens has been developed. Drawing inspiration from existing literature, influence of microlensing has been analysed by varying several parameters, including surface density of microlenses, source position, stellar initial mass function (IMF), total mass, and mass ratio of the binary system producing gravitational waves. The analysis extensively explores the impact of these parameters and quantifies microlensing effects by calculating mismatch and effective micro-amplification, which serve as quantifiable indicators of the variances introduced by microlensing in the estimation of intrinsic source parameters and the measurement of luminosity distance from gravitational wave signals respectively.

The findings from mismatch analysis show that when the macroimage magnification is small, population of microlenses are less likely to impact measurement of intrinsic source parameters. Effective micro-amplification analysis shows that microlensing always leads to net amplification of the original macrolensed waveform from type 1 macroimage and hence microlensing can introduce error in the cosmological investigations in strong lensing studies. Among all the parameters investigated, the most significant contributor to microlensing effects is the source position (macroimage magnification), and large microlensing effects can also be expected for high surface density of microlenses, low-mass binaries, and a mass ratio of source binary being unity for a relevant IMF for masses of microlenses.

Beyond code development and independent research, this work serves as a noteworthy contribution to the existing literature due to its comprehensive and systematic quantification of the effect of microlensing. The detailed analysis of each parameter space presented in this work can be directly applied to existing literature studies on strong lensing and can serve as a foundation for further investigations into microlensing effects.

Summary for a General Audience

Gravitational waves are disturbances that propagate through the very fabric of spacetime, much like the ripples that radiate across a pond when a pebble is tossed in. However, these spacetime waves are generated by the motion of celestial objects, such as two stars orbiting each other and gradually losing energy in the form of these gravitational waves during their orbital dance. As these gravitational waves journey toward us, they can encounter and be influenced by various celestial objects along their path, including galaxies and stars. This phenomenon is known as gravitational lensing. The effect of this bending by the galaxies often leads to multiple images of the source as we look in the sky. These images are what we detect using the relevant instrument.

However, this phenomenon of gravitational lensing by galaxies is also influenced by the stars, like Sun that lie closeby to the galaxies. These stellar objects can impact the signals from lensing by galaxies detected by our instruments, potentially introducing complexities in the analysis of these signals. Therefore it is essential to investigate how a population of these stellar objects stars affects the lensed signal from the massive galaxies. To achieve this objective, a code has been developed specifically for simulating the presence of a population of these stellar objects (ranging from 0.08 to 1.5 times the mass of the sun) in close proximity to the massive galaxy (mass $\sim 10^{10}$ times the mass of sun). This code builds upon existing methods used to model gravitational lensing caused by a single star. Additionally, two key parameters have been used to systematically quantify the impact of microlensing, changes in which affect the measurement of the parameters one can infer from the Gravitational wave observations. Within the setup of this work, for the signal which is weakly magnified due to lensing by the galaxy lens, it has been found that the population of these stellar mass objects are less likely to significantly impact the measurement of the parameters such as mass and spin of the source producing gravitational waves in the observation. However, the effective amplitude of the original gravitational wave signal lensed by the galaxy is likely to be amplified due to the presence of a population of these stellar mass objects, which holds significant importance in cosmological investigations associated with lensing studies.

In addition to the coding related aspect, this research also contributes to the existing literature by systematic quantification of the lensing effects of a population of these stellar mass objects. The insights derived from this thesis and the code developed possess the potential for application in existing literature studies and in the extended exploration of the effect.

Acronyms

aLIGO Advanced Laser Interferometer Gravitational Wave Observatory.

Arcsec Arcsecond.

CBC Compact Binary Coalescence.

Cumulative Distribution Function CDF.

EM Electromagnetic.

FLRW Friedmann-Lemaitre-Robertson-Walker.

Freq Frequency.

GR General Relativity.

GW Gravitational Wave.

IMF Initial Mass Function.

ISCO Innermost Stable Circular Orbit.

LIGO Laser Interferometer Gravitational Wave Observatory.

Mpc Mega Parsec.

NS Neutron Star.

Power Spectral Density Power Spectral Density.

SIS Singular Isothermal Sphere.

List of Figures

List of Tables

Contents

Chapter 1

Introduction

According to the theory of General Relativity, the compact concentrations of energies should curve spacetime and when these energy concentrations change the shape, it generates distortions, in the form of oscillations in spacetime. These propagating disturbances in the fabric of spacetime are called gravitational waves. These waves are expected to have a wide range of frequencies, from $\sim 10^{-18}$ Hz to 10^4 Hz for ripples in the cosmic background to the creation of neutron stars in supernova explosions respectively, as explained in (1). Herman Bondi gave the first precise mathematical explanation of these waves in 1962 (2) and Hulse and Taylor provided first indirect evidence for the existence of these waves with the discovery of the binary pulsar PSR 1913+16 in 1974 (3). The year 2015 marked the first ever detection of the gravitational waves by aLIGO (4). Since then, the worldwide network has identified over 80 black hole mergers, along with some neutron star mergers and potential black hole - neutron stars mergers (5). The frequency range for the operation of aLIGO spans from 10 Hz to 10^4 Hz (6).

Another consequence from the theory is the concept of gravitational lensing, which posits that the light rays are deflected when they propagate through a curved space time. Because of this bending there can be multiple ways for the light to travel from the source to the observer, which creates one or several deformed or magnified image(s) of the source (7). An intervening mass acts as a lens and deflects the light from the source, called a gravitational lens. The gravitational waves, like the electromagnetic rays are subject to gravitational lensing (8) (7) (9).
For the purpose of this study, two types of gravitational wave lensing, depending on the source and properties can be distinguished : Strong Lensing and Microlensing (10).
In strong lensing, the lens is a large mass (typically a galaxy/galaxy cluster $\sim 10^{10} M_\odot$ (11)) and the lensing produces mulitple images of the source, with the typical image separations in of the order of arcsec (12). [1].The lens associated with the strong lensing is called macrolens and the corresponding images produced due to lensing are called macroimages and the corresponding image magnification due to lensing is called macro-magnification. In comparison to strong lensing, the microlensing is caused by the objects in the mass range $10^{-6} \leq m/M_\odot \leq 10^6$ (13). The microlenses embedded in a galaxy can have angular separation between the images of the order of microarcsec (12)(thus small as compared to strong lensing). The lens associated with the microlensing lensing is called microlens,

---

[1] In some special cases the alignment of the source and the lens will be such that light will be deflected to the observer in a ring called "Einstein ring."

the corresponding images produced due to lensing are called microimages and the corresponding image magnification due to lensing is called micro-magnification.

With the growing number of gravitational wave detections, the detection of lensed gravitational waves is a possibility (14). The likelihood of approximately one strongly lensed event per year at aLIGO design sensitivity, as reported by (15), (16), and (17). The latest 03a run suggests one in approximately every thousand events to be lensed (18). Numerous compelling scientific scenarios have been suggested for these strongly lensed events. For instance, these strongly lensed events are more effective in the localisation studies than unlensed events (the events not subjected to lensing), however the error in localisation studies involving the gravitational waves is heavily dependent on a clean environment devoid of errors induced due to microlensing by stars (19)(14) (20). The impact of microlensing is significant, as a substantial portion of the error in localization studies is attributed to this phenomenon (19). Due to diffraction effects (as will be discussed later), the microlensing leads to frequency dependent modulations in the amplification and phase shift of the signal (8),(12). If the signal-to-noise ratio (SNR) is higher than 30, we can distinguish the effects of microlensing on parameter estimation with reasonable accuracy as discussed in (21). For such high SNR, microlensing can thus change the estimated values of binary parameters such as the spin and mass, as illustrated in (8). Thus it becomes interesting to study and quantify the effect of microlensing on strongly lensed signals.

Most of the microlensing studies have been considering a single point mass lens affecting the macrolensed signal (8), (21),(22), however in realistic scenario the strongly lensed signal will be affected by a population of microlenses (12) (23) (24).
The population of microlenses was studied the first by (12). In this study, the authors discuss the effect of microlensing for the surface stellar density $12 M_{\odot} pc^{-2}$ and for very high image magnification due to strong lensing, the conditions that make microlensing inevitable as will be explained later in the study. These conditions may however not always hold as the image magnification due to strong lensing or the surface densities might not be very high, or atleast be different.
A detailed study of the effect of a population of microlenses on the strongly lensed signal in the aLIGO/Virgo frequency band has been conducted in (23), where the authors examined a broad range of parameter space associated with the effect of microlensing on the strongly lensed signal. It was investigated how various factors such as macro-magnifications, stellar densities, IMFs, source properties, etc affect microlensing. The investigation in the study has been conducted for the specific values of densities, strong lensing magnification and the strong lens properties, which can be found around type 1 macroimage. (one of the multiple images formed by the macrolensing; more about it can be found in section 3.6.)
The foundation established by the existing literature for the corresponding study of microlensing by a single microlens [(22), (8)] and a population of microlenses [(12), (23)] play a key role in shaping both the structure and the goal of the thesis as discussed in the next section.

1.0.1 Goal of this Thesis

The goal of this thesis is to analyse and quantify the impact of microlensing by a population of microlenses on a strongly lensed gravitational wave signal from type 1 macroimage. The thesis is an independent study inspired by the exploration of the parameter space previously undertaken in (23). The investigation encompasses several critical parameters namely the surface density of microlenses around the Type 1 macroimage, variations in the source position, the Stellar IMF (Initial Mass Function), total mass and mass ratio of the binary producing gravitational waves. Through systematic analysis of these factors, this thesis aims to deepen our understanding of the effect of these parameters in the microlensing of Type 1 macroimage.

For the purpose of the thesis I develop a code to simulate the population of microlenses around type 1 macroimage (3.6), since minima represent one of the most frequently observed types of lensed images in galaxy-scale lenses (23),(12), using the available code for microlensing by a single microlens (git repository - (25)). In addition to this, I also build upon the two parameters to quantify the effect of microlensing: the micro-amplification (the net signal amplification due to microlensing) and mismatch (to quantify the net observational difference in the signal waveform due to microlensing,5.3). A portion of the research procedure will also involve the utilization of LensingGW (11): a PYTHON package for lensing of gravitational waves.

In addition to the methodology, a significant distinction from (23) arises from the comprehensive analysis of the mismatch and micro-amplification associated with each parameter under consideration.

The structure of the thesis is as follows: Chapter 2 provides an introduction of a few preliminary concepts essential to understand the developments present in this work. Building on the same, Chapter 3 focuses on conceptual and mathematical description of the phenomenon of gravitational lensing for the electromagnetic radiation, as the concepts for the same also apply in the lensing of gravitational waves. Likewise, Chapter 4 provides a comprehensive understanding of the phenomenon of gravitational waves including their mathematical description, astrophysical sources, detection mechanism and importantly elucidates the key concepts related to the macrolensing and microlensing of gravitational wave signals. Chapter 5 is dedicated to describing the general lensing setup, the parameters employed for quantification of microlensing effects and the methodology employed for the same. The subsequent Chapter 6 is devoted to presenting and analysing the results where the impact of microlensing caused by a population of microlenses will be studied and analysed for the relevant parameters in consideration. This work finishes with a conclusion in chapter 7, along with an outlook on the future for research on microlensing of gravitational waves by a population of microlenses.

Chapter 2

Some Introductory Concepts

2.1 Goals of this Chapter

The objective of this chapter is to revisit fundamental principles, establishing a necessary foundation for comprehending the content of this thesis. While these principles would not be the central focus, they play a crucial role in grasping the more significant concepts that follow.

2.2 An introduction to General Relativity

Developed by Albert Einstein in the early 20th century, General relativity is a fundamental theory of gravity that is based on the principle of equivalence which states that the effect of gravity is indistinguishable from the effect of acceleration. Matter causes spacetime to curve and the space time causes matter to move. (we will also see this mathematically later in the section). The theory has been successful in explaining a wide variety of phenomenon including gravitational lensing and gravitational waves which are the focus of this thesis. This section is largely based on (9), (7) and (26) and I invite the interested reader to have a look into the reference for more details.

The theory defines the concept of spacetime - a four dimensional continuum that combines three axes of space and one axes of time. An event in the space time is defined by the coordinates

$$x^{\mu} = (x^0, x^1, x^2, x^3), \tag{2.1}$$

where $x^0 = t$ is the time coordinate and x^i are the spatial coordinates ranging from 0 to N where the dimensions of the spacetime are given as N+1. The units c= 1 and G= 1 units will be used throughout the thesis unless explicitly specified.

The notion of distance in the spacetime is defined by the metric tensor $g_{\mu\nu}$,

$$ds^2 = g_{\mu\nu} dx^{\mu} dx^{\nu}, \tag{2.2}$$

where ds^2 represents the spacetime interval and $dx^{\mu} dx^{\nu}$ represent the infinitesimal changes in the spacetime coordinates, where the summation convention is used (the repeated indices μ and ν) are summed over. The components of $g_{\mu\nu}$ depend on distribution of matter and energy in the spacetime which affects the curvature of spacetime. The metric tensor can vary throughout the spacetime which allows for the description of events such has

gravitational lensing and waves.
In addition to the metric tensor, there also exists an inverse metric satisfying the equation which allows to raise and lower indices in the tensor equation. The inverse metric can also be deifned as $g_{\mu\alpha}\ g^{\mu\beta} = \delta^{\beta}_{\alpha}$ where δ is the Kronecker delta.
Through the utilization of the metric tensor, we can categorize trajectories in spacetime into three types: the time-like trajectories distinguished by $ds^2 < 0$, space-like trajectories featuring $ds^2 > 0$ and finally, null trajectories characterized by ds^2 =0, Notably, phenomena such as light propagation and the transmission of gravitational wave radiation align with null trajectories.

For the Minkowski space (the space with no curvature/flat space), the metric is given as

$$\eta_{\mu\nu} = \text{diag}(-1, 1, 1, 1). \tag{2.3}$$

The metric around a spherically symmetric mass (such as a black hole or a star) is given as the Schwarzchild metric,

$$g_{\mu\nu} = \text{diag}\left(-\left(1 - \frac{2M}{r}\right), \left(1 - \frac{2M}{r}\right)^{-1}, r^2, r^2 \sin^2\theta\right) \tag{2.4}$$

where M is the mass of the gravitational source and r, θ and ϕ are the spatial coordinates. The curvature of the spacetime is related to the metric and this relationship is captured in a tensor called Riemann Tensor. The spacetime is flat if the Riemann tensor is null. Thus, for the Minkowski spacetime the curvature is 0 or the space is flat. Using the Riemann Tensor, Ricci Tensor and Ricci scalar are defined as

$$\begin{aligned} R_{\mu\nu} &= R^{\alpha}{}_{\mu\alpha\nu} \\ R &= g^{\mu\nu} R_{\mu\nu} \end{aligned} \tag{2.5}$$

The relation between the matter and the spacetime is given by Einstein equation as

$$G_{\mu\nu} + \Lambda g_{\mu\nu} = 8\pi T_{\mu\nu}, \tag{2.6}$$

where Lambda is the cosmological constant is a special term that Einstein added to his theory to describe a possible energy inherent to space itself. $G_{\mu\nu}$ is called the Einstein tensor, representing the curvature of spacetime in differentiated form) and $T_{\mu\nu}$ is the stress energy tensor representing the sources of gravity. This simple equation tells how a gravitational field represented by the curvature of spacetime is produced by the sources of gravity. In vacuum $T_{\mu\nu} = 0$. Solving the equation above allows the determination of the metric or the spacetime.

2.3 Cosmological Dynamics : The Cosmological Models, Redshift and Distances

This section will focus on describing some cosmological concepts namely some cosmological models, redshift and the concept of distances. This section is based on (27), (9) and (7).

2.3.1 Cosmological Models and Friedmann Equations

The cosmological principle asserts that the universe is homogeneous (the same in all positions) and isotropic (the same in all directions). The homogeneity, ensures consistency in the metric throughout the manifold (manifold is a space that, on a local level, resembles Euclidean space, but globally, it might have a more intricate and curved structure), while isotropy dictates that the spatial configuration remains consistent from any viewpoint One of the most significant implications of this principle and the Einstein's equation is the understanding that the universe is expanding. The cosmological constant Λ plays a role in this expansion, counteracting the attractive force of gravity and causing the universe to accelerate. The spacetime metric for the expanding universe can be written as

$$ds^2 = -dt^2 + a(t)^2 \left(\frac{dr^2}{1-kr^2} + r^2 d\theta^2 + r^2 \sin^2\theta \, d\phi^2 \right), \tag{2.7}$$

which is called the Friedmann-Lemaître-Robertson-Walker (FLRW) model where $a(t)$ is the scale factordefined as $a(t = t_0) = 1$ for t_0 being present time. k is the curvature parameter where $k = -1, 0, 1$ for open, flat, and closed universes respectively, and t, r, θ, and ϕ are the spatial coordinates.

Using FLRW metric and making appropriate assumptions for $T_{\mu\nu}$, the Einstein equations can be written to obtain the Friedmann equations as (restored G,c units being used here)

$$\begin{aligned} \left(\frac{\dot{a}}{a}\right)^2 &= \frac{8\pi G}{3}\rho - \frac{k}{a^2} + \frac{\Lambda}{3} \\ \frac{\ddot{a}}{a} &= -\frac{4\pi G}{3}(\rho + 3p) + \frac{\Lambda}{3} \end{aligned} \tag{2.8}$$

where the scale factor in the Friedmann equations is related to the Hubble parameter as

$$H(t) = \frac{\dot{a}(t)}{a(t)}. \tag{2.9}$$

Friedmann model is uniquely determined by four parameters, known as the cosmological parameters, given as

$$H_0 = \frac{\dot{a}(t_0)}{a(t_0)}, \quad \Omega_M = \frac{8\rho}{3H_0^2}, \quad \Omega_\Lambda = \frac{\Lambda}{3H_0^2}, \quad \Omega_k = -\frac{k}{a(t_0)^2 H_0^2}, \tag{2.10}$$

where and the value of Hubble parameter at the present time H_0 is called the Hubble constant, Ω_M quantifies the fraction of the critical density contributed by matter, Ω_Λ represents the fraction contributed by the cosmological constant, and Ω_k accounts for the contribution of spatial curvature to the total energy density of the universe.

The Friedmann equation 2.8 can be written in terms of cosmological parameters as

$$\Omega_M + \Omega_\Lambda + \Omega_k = 1 \tag{2.11}$$

and the current estimates (28) show that

$$H_0 = 69.7 km/s \quad \Omega_M \sim 0.3, \quad \Omega_\Lambda \sim 0.7, \quad \Omega_k \sim 0 \tag{2.12}$$

which means that the the Universe is spatially flat and expanding. FLRW cosmology with a cosmological constant, and no curvature, called the Flat Lambda CDM Model. Flat Lambda CDM Model model with the appropriate values of current estimates listed above will be used throughout in the thesis.

2.3.2 Cosmological Redshift

[The description of this section involves the terminology associated with light however the concepts discussed are equally applicable to gravitational waves].

As the universe expands the wavelength λ_{em} of the emitted photon from a distant object at time t is observed with a higher wavelength λ_{obs} at time t_0. The relation between the emitted and the observed wavelengths can be expressed in terms of the scale factor at at emission $a(t)$ and the observation $a(t_0)$ as,

$$\frac{\omega_{obs}}{\omega_{em}} = \frac{a(t)}{a(t_0)} \tag{2.13}$$

The redshift, defined as the fractional change in wavelength, can also be expressed in terms of the scale factors as,

$$z = \frac{\lambda_{obs} - \lambda_{em}}{\lambda_{em}} \tag{2.14}$$

The redshift can also be expressed in terms of the scale factor as

$$z = \frac{(a(t_0) - a(t))}{(a(t))}. \tag{2.15}$$

As $a(t_0) = 1$, the relation becomes

$$\begin{aligned} z &= \frac{1 - a(t)}{a(t)} \\ a &= \frac{1}{1+z}. \end{aligned} \tag{2.16}$$

2.3.3 Distances

The concept of distances may become rather complicated as a result of the expansion. Here are a couple cosmologically relevant distances.

- Proper Distance: It is the distance between the two events measured using a reference frame in which they occur simultaneously. (or the distance between the two objects measured at a particular instance of time). In a flat Universe, at the present time, the proper distance is just comoving distance r_0, which is the Eucledian distance. The proper distance at any time can be defined as $d_p(t) = a(t)r_0 = r_0/(1+z)$. Both the proper distance and the comoving distance cannot be measured.

- Luminosity distance: This is the distance inferred from the luminosity of the object and apparent brightness defined. It can be written in terms of comoving distance and the redshift as $d_L = r_0(1 + z)$.

- Angular Diameter Distance: It is defined as the ratio of the physical size D of an object to its angular size θ as $D_A = D/\theta$ and is related to the comoving and luminosity distance as
  $D_A = \frac{d_L}{(1+z)^2} = \frac{r_0}{1+z}$.

Chapter 3

Gravitational Lensing : Basic Concepts

3.1 Goals of this chapter

The objective of this chapter is to provide a theoretical overview of gravitational lensing concepts. The explanations will be made in the context of light rays however the learnings of this chapter will be directly applicable in understanding of the lensing of gravitational waves as we will see in chapter 4. The chapter commences with an explanation of the fundamental configuration of gravitational lensing and introduction to lensing equation. Subsequently, it delves into various concepts such as deflection angle, lensing potential, magnification, time delay, types and number of images formed by lensing. Finally, the chapter covers some of the significant lens models relevant to the thesis. Overall, this chapter aims to equip the reader with a solid theoretical foundation of the gravitational lensing. This chapter is largely based on (29), (13) and I invite the interested readers to have a look at these references for more details.

3.2 Introduction to Basic Lensing Configuration and Lens Equation

This section focuses on the mathematical description of the phenomenon in the flat space. For more details, please refer to (9), (29).

Figure 3.1 shows a typical lensing configuration with the source, lens and the observer. The thin lens approximation is assumed to hold, meaning that the dimensions of the lens are small compared to the distances between the source, lens, and observer. This assumption allows us to consider lensing to occur in the plane of the lens, known as single-plane lensing. We assume the source to lie in the source plane and the lens to lie in lens plane where the images form as a result of lensing. The axis that crosses O and L is chosen as the reference axis for measuring angles and the angular positions on both the lens and source planes. The source's displacement from the line of sight (O-L axis) is given by $\vec{\eta}$ and it is placed at an angular position $\vec{\beta}$. The relation between the two can be expressed as $\vec{\eta} = D_S \ \vec{\beta}$. The angular position of the source in the source plane due to lensing is given by $\vec{\theta}$, and the impact parameter of the light ray (lensed image of source)

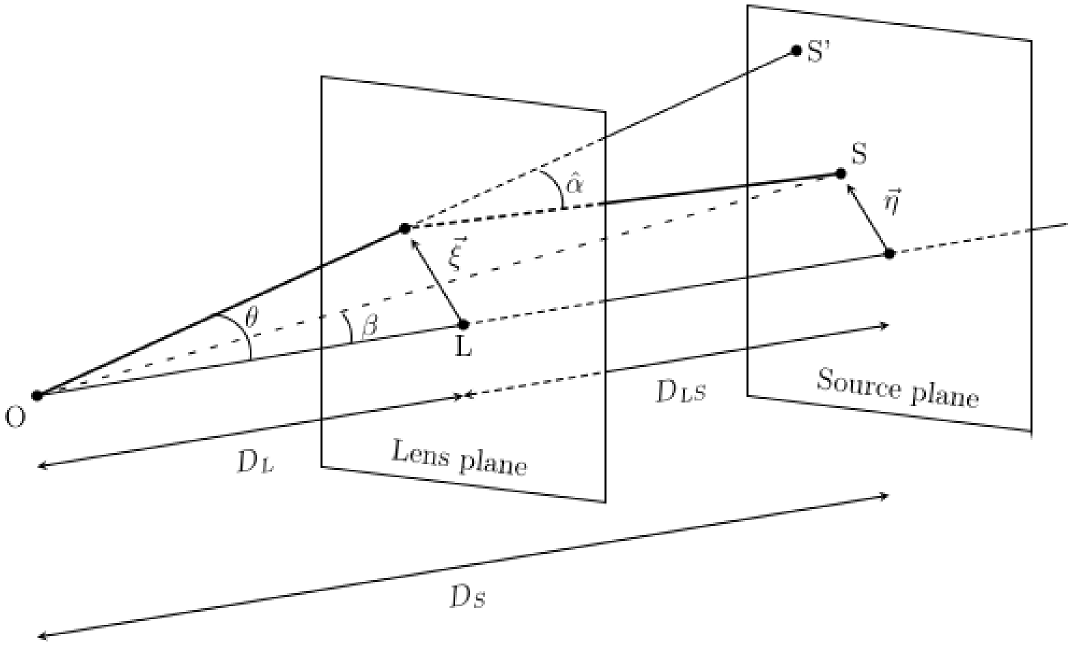

Figure 3.1: A sketch of lensing configuration, by (30) where observer, source and the lens at located at points O,L and S, in their respective planes. The lensing configuration is described by the source displacement from the line-of-sight $\vec{\eta}$, the angular diameter distance from the observer to the source D_S, to the lens D_L, and from the lens to the source D_{LS}, as well as by the relative position of the image in the image plane $\vec{\xi}$.

on the lens plane is $\vec{\xi} = D_L\ \vec{\theta}$, Additionally, we define the deflection angle $\widehat{\vec{\alpha}}$ as the angle between the deflected light ray's path due to lensing and the trajectory it would have had it not been deflected. These angles using the angular distance between the apparent and true source positions as can be related as

$$D_S\vec{\theta} = D_S\vec{\beta} + D_{LS}\widehat{\vec{\alpha}}, \tag{3.1}$$

where the reduced deflection angle is defined as

$$\vec{\alpha}(\vec{\theta}) = \frac{D_{LS}}{D_L}\widehat{\vec{\alpha}}(\vec{\theta}). \tag{3.2}$$

Using the information above, the lens equation can be written as

$$\vec{\beta} = \vec{\theta} - \vec{\alpha}(\vec{\theta}). \tag{3.3}$$

Introducing the following dimensionless quantities: $\vec{x} = \frac{D_L\vec{\theta}}{\xi_0}$, $\vec{y} = \frac{D_L\vec{\eta}}{D_S\xi_0}$, where ξ_0 is the length scale in the lens plane, the lens equation can be further modified as

$$\vec{y} = \vec{x} - \vec{\alpha}(\vec{x}). \tag{3.4}$$

For simplicity reasons, one converts to the units standardized by the Einstein radius, which is defined as

$$\begin{aligned} R_0 &= \theta_E D_L\ , \\ \theta_E &= \sqrt{\frac{4M_L D_{LS}}{D_L D_S}}, \end{aligned} \tag{3.5}$$

where M_L is the total lens mass, θ_E is the Einstein angle while other symbols have their usual meanings. The significance of the Einstein radius can be analysed as if the source is directly behind the lens, i.e. $\beta = 0$, the image of the source is spread in a circular ring called Einstein ring which makes an angle $\theta = \theta_E$.

3.3 Lensing Potential

To illustrate the impact of gravitational lensing, consider a perturbed FLRW metric (1,(23))as the underlying background:

$$ds^2 = -(1+2U)dt^2 + a(t)^2(1-2U)d\vec{r}^2 = g_{\mu\nu}dx^\mu dx^\nu \tag{3.6}$$

where $U \equiv U(\vec{r}) = -M/r$ is the gravitational potential of the lens, with $\vec{r}$ being the spatial vector. It is assumed that $U << 1$, thus considering a weak field.
The expression for effective lens potential is given by projecting the three dimensional potential U on the lens plane as (29)

$$\hat{\Psi}(\vec{\theta}) = 2\frac{D_{LS}}{D_L D_S}\int U(D_L\vec{\theta}, Z)dZ. \tag{3.7}$$

The dimensionless lensing potential is defined as,

$$\Psi(\vec{x}) = 2\frac{D_{LS}D_L}{D_S R_0^2}\int U(\vec{x}, Z)dZ, \tag{3.8}$$

where again the integration is done outside the lens plane.
For a two-dimensional mass distribution, using the thin-lens approximation, the source for the potential is the matter distribution described using the surface density $\sum(\vec{x})$ as

$$\sum(\vec{x}) = \int \rho(\vec{x}, Z)dZ, \tag{3.9}$$

where ρ is the three-dimensional density.

It satisfies two important properties (29):

- The gradient of Ψ is equal to the scaled deflection angle:

$$\vec{\nabla}_{\vec{x}}\Psi(\vec{x}) = \vec{\alpha}(\vec{x}). \tag{3.10}$$

- The Laplacian of Ψ is equal to the convergence

$$\triangle_{\vec{x}}\Psi(\vec{x}) = 2\kappa(\vec{x}), \tag{3.11}$$

  where convergence is defined as: $\kappa(\vec{x}) = \frac{\sum(\vec{x})}{\sum_{cr}}$ where $\sum_{cr} = \frac{1}{4}\frac{D_S}{D_{LS}D_L}$ is the critical surface density (more about convergence and critical density will be discussed in the upcoming sections).

3.4 Magnification

Gravitational lensing of the source can lead to the magnification/de-magnification or distortion of the images of the source, due to different rays being deflected at different distances from the lens, especially when the source has non-negligible apparent size[1]. Liouville's theorem says that the surface brightness of a ray in empty space is conserved, thus the surface brightness is conserved along the ray and the gravitational lensing only affects the direction and cross-section of a bundle of the light rays. The magnification μ is defined as the ratio of the flux of lensed to the unlensed source. Since the surface brightness is conserved, the magnification can be written as the ratio of the solid angle subtended by the lensed image $d\Omega_L$ to the that of the unlensed source, $d\Omega_o$ as (7),

$$\mu = \frac{d\Omega_L}{d\Omega_o} = \frac{D_S^2 dA_L}{D_L^2 dA_S}, \tag{3.12}$$

where the ratio of the two solid angles is related to the ratio of infinitesimal area on the lens plane dA_L to the corresponding area on the source plane dA_S. It can be shown that (29),

$$\frac{d\Omega_o}{d\Omega_L} = \left|\det \frac{\partial \vec{y}}{\partial \vec{x}}\right| \tag{3.13}$$

and thus, the magnification is

$$\mu = \left|det \frac{\partial \vec{y}}{\partial \vec{x}}\right|^{-1} \tag{3.14}$$

or,

$$\mu(\vec{x}) = \frac{1}{(\det A(\vec{x}))}, \tag{3.15}$$

where

$$A(\vec{x}) = \frac{\partial \vec{y}}{\partial \vec{x}}, A_{ij} = \frac{\partial y_i}{\partial x_j} \tag{3.16}$$

is Jacobian matrix for the lensed equation 3.4 and y_i and x_i represent the ith component of $\vec{x}$ and $\vec{y}$ on the lens plane.
Using the lens equation 3.4, and 3.10, A can be written as

$$A_{ij} = \delta_{ij} - \frac{\partial^2 \Psi(\vec{x})}{\partial x_i \partial x_j}. \tag{3.17}$$

For simplification, we write, $\frac{\partial^2 \Psi(\vec{x})}{\partial x_i \partial x_j}$ as Ψ_{ij} where x_i denotes the i-th component of $\vec{x}$ on the lens plane. The matrix notation plays a key role in the definition of magnification using convergence and shear.
The shear matrix quantifies the distortion of the background source by representing the projection of the gravitational tidal field. It is an anti-symmetric and trace-free matrix, characterized by the isotropic component of the Jacobian as (29),

---

[1] the angular size of the source is smaller than the angular size over which the properties of the lens change.

$$
\begin{aligned}
(A - \frac{1}{2}trA.I)_{ij} &= \delta_{ij} - \Psi_{ij} - \frac{1}{2}(1 - \Psi_{11} + 1 - \Psi_{22})\delta_{ij} \\
&= -\Psi_{ij} + \frac{1}{2}(\Psi_{11} + \Psi_{22})\delta_{ij} \\
&= \begin{pmatrix} -\frac{1}{2}(\Psi_{11} + \Psi_{22}) & -\Psi_{12} \\ -\Psi_{12} & \frac{1}{2}(\Psi_{11} + \Psi_{22}) \end{pmatrix}
\end{aligned} \tag{3.18}
$$

The vector $\vec{\gamma} = (\gamma_1, \gamma_2)$, is called shear, where γ_1, γ_2 are given as

$$
\begin{aligned}
\gamma_1(\vec{x}) &= \frac{1}{2}(\Psi_{11} - \Psi_{22}) \\
\gamma_2(\vec{x}) &= (\Psi_{21} = \Psi_{12}).
\end{aligned} \tag{3.19}
$$

and the eigen values of 3.18 are

$$
\pm\sqrt{\gamma_1^2 + \gamma_2^2} = \pm\gamma. \tag{3.20}
$$

As a result there is a coordinate rotation wirh angle ϕ, (29) such that

$$
\begin{pmatrix} \gamma_1 & \gamma_2 \\ \gamma_2 & \gamma_1 \end{pmatrix} = \gamma \begin{pmatrix} cos(2\phi) & sin(2\phi) \\ sin(2\phi) & cos(2\phi). \end{pmatrix} \tag{3.21}
$$

The trace of the Jacobian matrix can be used to derive convergence κ as,

$$
\begin{aligned}
\frac{1}{2}trA &= [1 - \frac{1}{2}(\Psi_{11} - \Psi_{22})]\delta_{ij} \\
&= (1 - \frac{1}{2}\Delta\Psi)\delta_{ij} \\
&= (1 - \kappa)\delta_{ij}.
\end{aligned} \tag{3.22}
$$

Thus the Jacobian matrix A takes the form,

$$
\begin{pmatrix} 1 - \kappa - \gamma_1 & -\gamma_2 \\ -\gamma_2 & 1 - \kappa + \gamma_1 \end{pmatrix} = (1 - \kappa)\begin{pmatrix} 1 & 0 \\ 0 & 1 \end{pmatrix} - \gamma \begin{pmatrix} cos(2\phi) & sin(2\phi) \\ sin(2\phi) & -cos(2\phi) \end{pmatrix} \tag{3.23}
$$

From equation 3.23 it can be seen that the shear measures the anisotropic stretching of the image (31) , on the other hand, the distortion due to convergence is isotropic, i.e. constant in all the directions. This can also be well represented by Fig. (3.2). Using the expressions for convergence and shear, we can write the magnification as,

$$
\mu = [(1 - \kappa)^2 - \gamma^2]^{-1}. \tag{3.24}
$$

Thus, gravitational lensing introduces convergence and shear at the location of the image, which defines the magnification of the lensed image of the source.

The curves on the lens plane which satisfy $\det A = 0$ are called critical curves, where the magnification is ideally infinite. The critical curve mapped to the source plane (obtained by mapping from $\vec{x} \rightarrow \vec{y}$, using the lens equation) are called caustics. These play an important role in discussion of the types and number of images in 3.6.

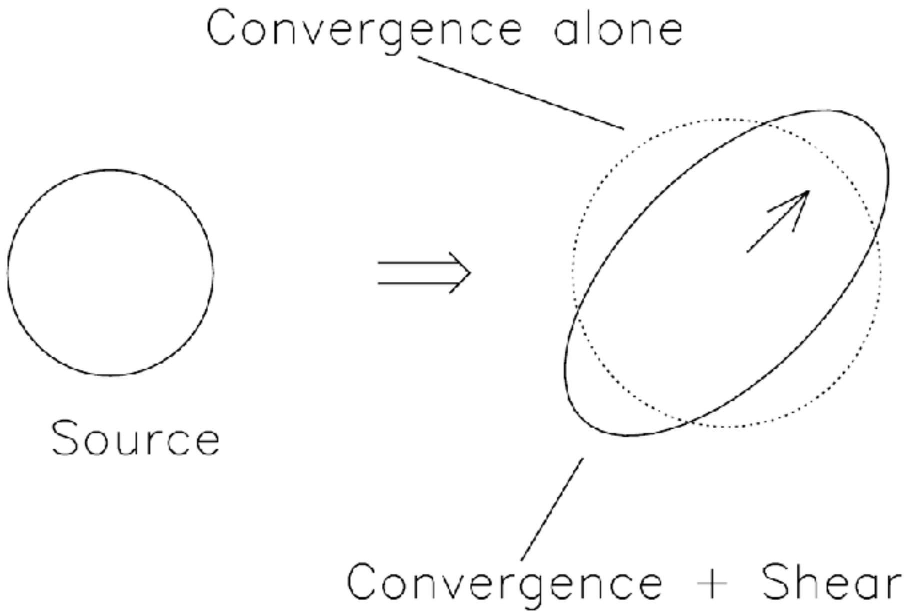

Figure 3.2: Illustraion of the effect of convergence and shear on the image of the source. Fig. credits: (32)

3.5 Time Delay

In addition to the magnification, one of the most significant characteristic of the gravitational lensing is the introduction of a time delay in the arrival of the signal to the observer. The time delay t_d has two components

$$t_d = t_{geom} + t_{grav}, \tag{3.25}$$

where t_{geom} is the geometrical time delay due to lensed ray having different path length as compared to the unlensed ray and t_{grav} is the potential or Shapiro time delay introduced because of the slowing down of the radiation as it travels through the gravitational potential of the lens ((9),(29))
For the lens at redshift z_L, the time delay is defined as, (33)

$$t_d(\vec{x},\vec{y}) = \frac{(1+z_L)R_0^2 D_S}{D_L D_{LS}}[\frac{1}{2}|\vec{x}-\vec{y}|^2 - \Psi(\vec{x}) - \phi_m(\vec{y})] \tag{3.26}$$

We also define Fermat potential $T_d(\vec{x},\vec{y})$ as,

$$T_d(\vec{x},\vec{y}) = [\frac{1}{2}|\vec{x}-\vec{y}|^2 - \Psi(\vec{x}) - \phi_m(\vec{y})]. \tag{3.27}$$

where $\phi_m(\vec{y})$ in both the expressions is a constant independent of lens properties (23). For the time delay between the lensed and the unlensed ray $\phi_m(\vec{y})$ is zero.

The light rays travel along null geodesics. This important property has been be utilised in the study of gravitational lensing as 'Fermat's Principle'. The fermat's principle as mentioned in the book (13) states that for all the null curves going from a source S to a time-like observer 0, the light ray travels the path for which t_d is an extremum for all the paths considered.

which implies,

$$\delta t_d = 0 \tag{3.28}$$

or,

$$\vec{\nabla}_{\vec{x}}[t_d(\vec{x},\vec{y})] = 0 \tag{3.29}$$

using Fermat's principle and equation 3.26, one obtains,

$$(\vec{x}-\vec{y}) - \vec{\nabla}\Psi_{\vec{x}}(\vec{x}) = 0 \tag{3.30}$$

which after substituting to lens equation, 3.4 gives, 3.10.

3.6 Types and Number of Images formed by Lensing

From equation 3.29, it can be referred that the images of the source are located at the stationary points of the time delay function 3.26.
To determine whether the image forms at the minimum, maximum or saddle point of the time delay function, one has to compute the Hessian matrix of this surface given as,

$$T_{ij} = \frac{\partial^2 t_d(\vec{x},\vec{y})}{\partial x_i \partial x_j}. \tag{3.31}$$

This matrix represents the local curvature of the time delay surface where the time delay surface is given by equation 3.26. Lesser curvature in one direction implies the surface is flatter or "less bent" along that direction at the position of the image and results in a larger magnification of the image for observers in the same direction.
Using equation 3.30 one can write,

$$T_{ij} = (1+z_L)\frac{D_S D_L}{D_{LS}}(\delta_{ij} - \Psi_{ij}) \propto A. \tag{3.32}$$

Thus, the sign of the hessian matrix should be the same as the sign of A.
The three images can be distinguished (29):

- Type I Images: They appear at the minima of time delay surface, which requires the Hessian matrix and hence A to be both positive, hence $\det A > 0$ and $trA > 0$. Thus, the magnification has a positive value which means that the image gets magnified.

- Type II Images: These appear at the saddle point of the time delay surface. This requires the eigenvalues of A to have opposite signs, which implies, $\det A < 0$. The magnification is negative and the parity of the image is flipped as compared to the source.

- Type III Images: These appear at the maxima of the time delay surface. This requires $\det A > 0$ and $trA < 0$. As $\det A > 0$, these images also have positive magnification.

The upcoming paragraph gives a comprehensive description of the number and types of images, relevant for this study. A detailed description is beyond the scope of this work, however, I invite the interested to the references (29) and (13) for more details.

The properties of the time delay surface are closely related to respective alignment of the source position and the lens position as it affects the time delay function as can be shown in Figure 3.3 which demonstrates the profile of the time delay function for an axially symmetric lens with a core having radius x_c[2]. The lens has a smooth surface density it decreases faster than $|\vec{x}|^{-1}$ as $|\vec{x}| \to \infty$.

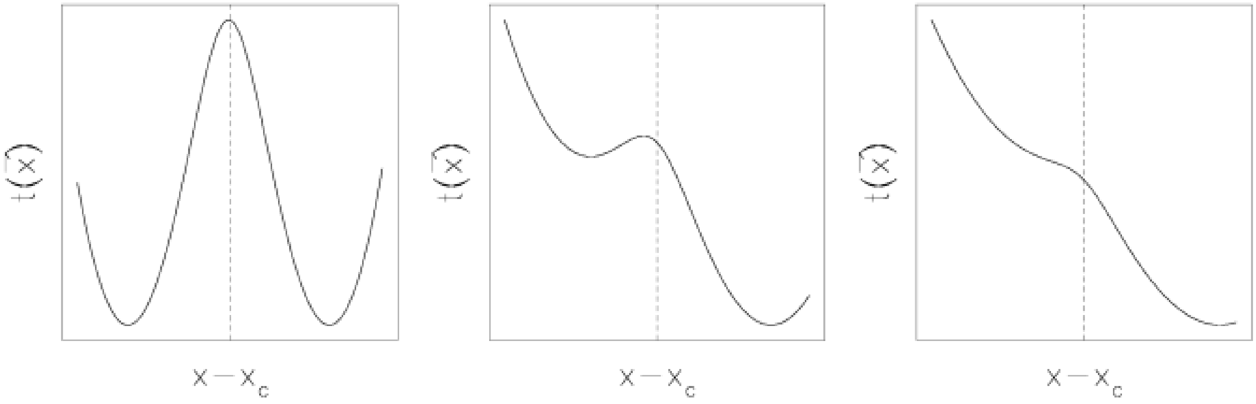

Figure 3.3: Profile of the time delay function for an axially symmetric lens with core. The source and the lens are aligned with the reference axis passing through the lens center in the leftmost plot and the source moving further away, increasing its distance from the reference axis as we move from left to right in the panels. Fig. credits: (29).

- The Left Panel: The panel displays the curvature of the time delay surface in case of the perfect alignment between the lens and the source. In this case, the maximum occurs at the center of the lens (Type III Image) and the minima of the time delay surface, i.e. the Type I Image exhibits an axial symmetry around the lens, forming the famous Einstein Ring. The Type III image is typically de-magnified due to the significant curvature of the time delay surface in this region.
- The Middle Panel: As the source moves away from the reference axis, the axial symmetry in the time delay surface breaks and the surface deforms. This results in the breaking of the ring to the form of Type I and Type II images at the minima and saddle point of the function, respectively. This results in a total of three images.
- The Right Panel: As the source moves further away, the minima and saddle point images approach each other. At a very far distance, they merge and disappear, leaving only the minima, i.e. Type I image.

---

[2] An axially symmetric lens refers to a type of gravitational lensing system in which the mass distribution causing the lensing effect possesses rotational symmetry around a specific axis, more about its properties will be discussed in the next section

In the absence of lensing potential, the time delay surface is a parabola having a single minimum, thus a Type 1 image, which can be viewed as the extreme case of the right panel in fig. 3.3. Thus, a Type 1 image always exists and the additional extrema (Type 2 and Type 3) always occur in pairs as illustrated by the central and the right panel of the Fig. 3.3, consisting of a maximum and a saddle point and therefore, the total number of images must always be odd.
As the $\det A < 0$ for the saddle and $\det A > 0$ for minima/maxima, the critical lines, marked by $\det A = 0$ act as boundaries that separate these pairs of multiple images. The pair of extrema (Type 2 and Type 3) merge and vanish at the critical lines, creating distinct regions with varying image multiplicities.
Similar to the critical curves it can also be demonstrated that the number of images changes by two when a source crosses a caustic. It can also be shown that $\sum_{cr}$ is the critical surface density which is sufficient but not necessary to have multiple images (13).

3.7 Lens Models

The section will focus on the two lens models that will be used in the study :
The Point Mass lens model and the Singular Isothermal Lens Model. The discussion is based on (13) and (29).

3.7.1 Point Mass

This lens model will be utilized to describe the microlenses. This lens model is axially symmetric i.e. the surface density is constant for the change in the position angle with respect to the center of the lens. Taking the axially symmetric model reduces the lens equation to one dimensional model which further simplifies the analysis.
For a point mass lens of mass M, the deflection angle can be expressed as, (26)

$$\widehat{\vec{\alpha}}(\vec{\xi}) = 4M\frac{\vec{\xi}}{\left|\vec{\xi}^2\right|} \tag{3.33}$$

$$\left|\widehat{\vec{\alpha}}(\vec{\xi})\right| = \frac{4M}{\xi} \tag{3.34}$$

where the symbols have their usual meanings as explained.[3]
The lensing potential for the point mass lens is

$$\Psi(\vec{\theta}) = \frac{4MD_L D_{LS}}{R_0^2 D_S} ln|\vec{\theta}| \tag{3.36}$$

---

[3] As deflection angle depends linearly on mass M of the lens, the deflection angle of multiple lenses can be superimposed as (29)

$$\widehat{\vec{\alpha}}(\vec{\xi}) = \sum_i \widehat{\vec{\alpha}}(\vec{\xi} - \vec{\xi}_i) = 4\sum_i \frac{M_i(\vec{\xi} - \vec{\xi}_i)}{\left|(\vec{\xi} - \vec{\xi}_i)\right|^2} \tag{3.35}$$

where M_i is the mass of each lens, and $\vec{\xi}_i$ represents the position of each point mass lens such that $(\vec{\xi} - \vec{\xi}_i)$ is the impact parameter of each point mass lens.

where R_0 is the Einstein radius (3.5) of the point mass lens of mass M.
Calculating the reduced deflection angle by substituiting equation 3.10 in equation 3.2, the lensing equation 3.4 can be written as (the vector notation can be dropped due to axial symmetry),

$$\begin{aligned}\beta &= \theta - \frac{4MD_{LS}}{D_L D_S},\\ \beta &= \theta - \frac{R_0^2}{\theta}\end{aligned} \tag{3.37}$$

where symbols have their usual meanings.
Converting to the units normalised by the Einstein radius, the equation 3.37 can be written as,

$$y = x - \frac{1}{x}, \tag{3.38}$$

solving which leads to the two solutions,

$$x_{\pm} = \frac{1}{2}[y \pm \sqrt{y^2 - 4}]. \tag{3.39}$$

This shows that the point mass lens forms two images of the source due to lensing independent of the position y of the source. It does not form 3 images as discussed in section 3.6 as the deflection potential is singular at $\theta = 0$ (equation 3.36) because of which the time delay surface is not deformed continuously.
If $y = 0$, $x_{\pm} = \pm 1$ which means that the image of the source is spread in a circular ring called Einstein ring as discussed in 3.2. However if $y >> 1$, $x_+ \rightarrow y$ and $x_- \rightarrow 0$, thus reaching no lensing limit.
From (29), the magnification for the point mass (equation 3.15) is given as

$$\mu_{\pm} = \frac{1}{2} \pm \frac{y^2 + 2}{2y\sqrt{y^2 + 4}}. \tag{3.40}$$

This shows that the image x_+ is always magnified ($\mu_+ \geq 1$) while the image x_- can be magnified or de-magnified depending on the source position.
The total magnification due to lensing by point mass is

$$\mu = \mu_+ + \mu_- = \frac{y^2 + 2}{y\sqrt{y^2 + 4}}. \tag{3.41}$$

3.7.2 Singular Isothermal Sphere

Not only this lens model is simpler due to its axial symmetry, it is also widely used to describe the rotation curves of the galaxies. This lens model will be used in the thesis for the macrolens.
The surface density for this model is given as

$$\sum(\vec{\xi}) = \frac{\sigma^2}{2\xi}, \tag{3.42}$$

where σ is the velocity dispersion of the particles of the gas[4].
The einstein radius of the lens is given by equation 3.5, where M is taken to be the mass

---

[4] with the gas taken in thermal and hydrostatic equillibrium.

of the SIS lens. The deflection potential of the lens is,

$$\Psi(x) = |x|. \tag{3.43}$$

using which the lens equation 3.4 yields,

$$y = x - \frac{x}{|x|}. \tag{3.44}$$

The solutions of the lens equation above are dependent on y as follows:

- If $y < 1$, the lens equation has two solutions: $x_{\pm} = y \pm 1$, occurring on the opposite side of the lens center.
- If $y > 1$, there is only one solution : $x = y + 1$.

Again the number of images are not odd because as discussed in the section 3.7.1, there is a singularity in surface density at $\xi = 0$ (equation: 3.42).
The images at $x > 0$ are Type 1 while those at $x < 0$ are Type 2 ((29), 3.6)
From (29) , the magnification for the point mass (equation 3.15) is given as

$$\mu = \frac{|x|}{|x| - 1} \tag{3.45}$$

For $y < 1$, the magnification of the two images x_+ and x_- is

$$\mu_+ = 1 + \frac{1}{y}, \quad \mu_- = 1 - \frac{1}{y}. \tag{3.46}$$

If $y \rightarrow 1$, the magnification of the image $\mu_- \rightarrow 0$ and at $y = 1$ this image completely disappears. However if $y \rightarrow \infty$, i.e. for the source at large distance from the lens $\mu_{\pm} \rightarrow 1$.

Chapter 4

Gravitational Lensing of Gravitational Waves

4.1 Goals of this Chapter

Building upon the introduction of the concept of lensing of gravitational waves in Chapter 1, the objective of this chapter is a comprehensive understanding of the concept of gravitational lensing of gravitational waves. The chapter commences with discussion about gravitational waves, including their mathematical description, astrophysical sources and detection mechanism. Subsequently, the chapter delves into a theoretical discussion about the concept of lensing of gravitational waves where we will discuss strong lensing and microlensing and derive the expression for amplification factor in the realm of wave optics and geometrical optics.

4.2 Mathematical Description of Gravitational Waves

This section offers a concise mathematical description of Gravitational Waves. The developments in this chapter are based on (9) and the discussion in 2 and I invite the interested reader to check the reference for more details.

The mathematical expression of these waves is obtained by perturbing the background metric, $\tilde{g_{\mu\nu}}$ which is a solution to the Einstein's equations, as described by 3.6 by small perturbation $h_{\mu\nu}$ ($|h_{\mu\nu}| << 1$) as

$$g_{\mu\nu} = \tilde{g_{\mu\nu}} + h_{\mu\nu}, . \tag{4.1}$$

This can be understood as as a two-index symmetric tensor $h_{\mu\nu}$ propagating in space described by the metric $\tilde{g_{\mu\nu}}$. A simple explanation of these waves is obtained by considering the gravitational field to be weak, such that we can view the perturbation in Minkowski space as $g_{\mu\nu} = \tilde{\eta_{\mu\nu}} + h_{\mu\nu}$. The gravitational field is not static and there are no restrictions on the particle motion in the field (velocity of particle $\sim c$). Using these approximations, the linearized Einstein field equations can be obtained as $G_{\mu\nu} = 8\pi T_{\mu\nu}$.

Using some mathematical manipulations such as gauge invariance and transformation (similar to electromagnetism (9)) and taking the energy-momentum tensor equal to zero

$(T_{\mu\nu} = 0)$,the linearized field equations in vacuum are

$$\Box\bar{h}_{\mu\nu} = 0, \tag{4.2}$$

where $\Box\bar{h}_{\mu\nu}$ is the trace-reversed perturbation defined as $\bar{h}_{\mu\nu} = h_{\mu\nu} - \frac{1}{2}\eta_{\mu\nu}h$ and $\Box = \eta^{\rho}\partial_{\lambda}\partial_{\rho}$ is the D'Almbertian operator (9).
This a classical wave equation, very similar to the electromagnetic equation, with plane waves as a solution:

$$\bar{h}_{\mu\nu} = C_{\mu\nu}e^{ik_{\sigma}x^{\sigma}}, \tag{4.3}$$

where $C_{\mu\nu}$ is the polarization tensor, giving the amplitude of the gravitational wave components and k_{σ} is the wave vector using which it can be deduced that these waves travel at the speed of light. The time-like component of the wave-vector gives the frequency ω for the oscillations of these waves. Applying the conditions for the transverse traceless gauge (9), two degrees of freedom can be imposed on the perturbation tensor and it is denoted by $h^{TT}_{\mu\nu}$. By aligning the z-axis with the direction of propagation, both degrees of freedom can be fully characterized by the amplitudes of the perturbation in the $x-y$ plane. These degrees of freedom are commonly referred to as "plus" and "cross" polarizations and the gravitational wave solution is characterized as

$$h^{TT}_{\mu\nu}(t,z) = \begin{pmatrix} 0 & 0 & 0 & 0 \\ 0 & h_{+} & h_{X} & 0 \\ 0 & h_{X} & -h_{+} & 0 \\ 0 & 0 & 0 & 0 \end{pmatrix} cos[\omega(t-z)]. \tag{4.4}$$

The line element ds^2 can be written as

$$ds^2 = -dt^2+dz^2+dx^2[1+h_{+}(cos[\omega(t-z)])]+dy^2[1-h_{+}(cos[\omega(t-z)])]+2dxdy[h_{X}(cos[\omega(t-z)])]. \tag{4.5}$$

Therefore, for the gravitational wave travelling in z direction, h_{+} and h_{X} represent the plus and cross polarization or oscillations of gravitational wave in x and y direction which can also be understood using a simple illustration in Fig. 4.1.

4.3 Gravitational Radiation from Sources

We will now focus our attention to the generation of gravitational waves by sources. The explanation in this section is based on (9) and (35).

Using some mathematical manipulations such as gauge invariance and transformation (9), the linearized Einstein's equations coupled with the matter is obtained as

$$\Box\bar{h}_{\mu\nu} = -16\pi T_{\mu\nu}, \tag{4.6}$$

where $T_{\mu\nu}$ is again the energy momentum tensor.
The solution to this equation is obtained using the Green's function. The solutions are called retarded or advanced depending upon whether they represent the waves travelling forward or backward in time. The retarded Green's function represents the accumulated

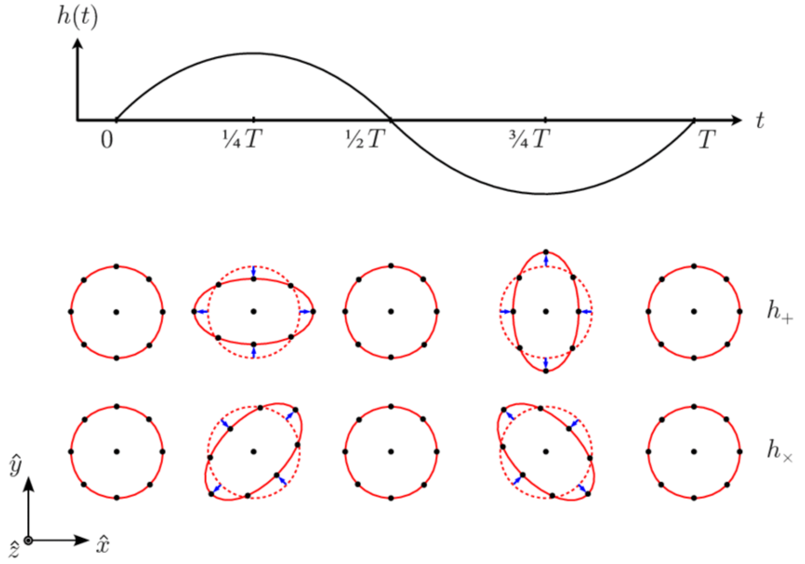

Figure 4.1: Illustration of the h_+ and h_X polarization of the gravitational wave signal $h(t)$ with $\omega = \frac{2\pi}{T}$ propagating along z direction on a ring of freely falling particles. Figure credits : (34).

effect of signals from the past on the point currently under examination. The expression for the retarded Green's function is as follows:

$$\bar{h}_{\mu\nu}(t, \vec{x}) = 4 \int \frac{1}{|\vec{x} - \vec{y}|} T_{\mu\nu}(t - |\vec{x} - \vec{y}|, \vec{y}) d^3y \tag{4.7}$$

where $\vec{x} = (x^1, x^2, x^3)$ and $\vec{y} = (y^1, y^2, y^3)$ are the spatial vectors, $t = x^0$ and and $t_r = t - |\vec{x} - \vec{y}|$.

With the assumption that the source is isolated, slowly moving (the radiation travels much faster than the objects or particles that emit it) and far away, the quadrupole moment tensor I_{ij} of energy density of the source is given as

$$I_{ij}(t) = \int y^i y^j T^{00}(t, \vec{y}) d^3y \tag{4.8}$$

using which

$$\bar{h}_{ij}(t, \vec{x}) = \frac{2}{r} \frac{d^2 I_{ij}}{dt^2}(t_r) \tag{4.9}$$

where r is the spatial distance from the source to the observer.
From the equation above, it follows that the gravitational wave generated by an isolated, non-relativistic object is directly related to the second derivative of the quadrupole moment of the energy density.
Furthermore, the power radiated due to the emission of the gravitational wave, hence the total gravitational luminosity can be written as

$$[\frac{dE}{dt}] = \frac{1}{5} < \dddot{Q}^{TT}_{ij} \dddot{Q}^{TT}_{ij} > \tag{4.10}$$

where $\dddot{Q}_{ij}^{TT}$ is the traceless part of I_{ij}:

$$Q_{ij} = I_{ij} - \frac{1}{3}\delta_{ij}\delta^{kl}I_{kl} \tag{4.11}$$

The learning above can be applied to study the gravitational wave radiation emitted due to the orbital decay of the binary composed of compact objects such as neutron stars and black holes (35).

4.3.1 Gravitational Waves from Compact Binary Systems

Compact binary systems consist of compact objects such as black holes or neutron stars, orbiting each other due to their mutual gravitational attraction. An initial approach to the emission of gravitational waves by binary systems involves assuming circular Keplerian orbits and utilizing the quadrupole approximation (equation 4.8) for the resulting gravitational wave signal.

Considering the Newtonian approximation and the center-of-mass frame, for a binary system made of two compact stars of mass m_1 and m_2, orbiting in the orbital radius R, we define, $M = m_1 + m_2$ is the total mass of the binary, $q = m_2/m_1 \in (0, 1]$ the mass ratio, where $m_1 \geq m_2$. The reduced mass μ is defined as $\mu = m_1m_2/M$. The combined kinetic and potential energy of the orbit, expressed as $E_{orbit} = E_{kin} + E_{pot} = -m_1m_2/2R$. Using Kepler's law, the orbital frequency of the binary can be written as,

$$\omega_s^2 = \frac{M}{R^3}. \tag{4.12}$$

The above energy relationship suggests that as the energy is lost to gravitational waves (GWs), R must progressively decrease over time but we will assume that the transition of the orbit is slow and adiabatic and thus binaries are slowly in 'inspiral' towards each other and hence this phase is called the inspiral.

The gravitational wave strain expressions for the plus and cross polarizations for binary coalescence can be derived from equation 4.9 as (35)

$$\begin{aligned} h_+(t) &= \frac{4}{r}\mu\omega_s^2R^2\frac{1+cos^2\theta}{2}cos(2\omega_st), \\ h_X(t) &= \frac{4}{r}\mu\omega_s^2R^2cos\theta sin(2\omega_st), \end{aligned} \tag{4.13}$$

where r is again the distance between source and observer. From the equation above, it can be deduced that the wavelength of the gravitational wave is twice the orbital period of the binary or $\omega_{gw} = 2\omega_s$.

Another expression to describe the gravitational wave emission is the chirp mass defined as,

$$M_c = \frac{(m_1m_2)^{3/5}}{(m_1+m_2)^{1/5}}. \tag{4.14}$$

For the mass ratio q, the chirp mass can be expressed as

$$M_c = \left(\frac{q}{(1+q)^2}\right)^{3/5} M. \tag{4.15}$$

Chirp mass is an important quantity as the frequency (f_{gw}) of the gravitational wave signal can be expressed using the same as (35)

$$f_{gw}^{-8/3}(t) = \frac{(8\pi)^{8/3}}{5}(M_c)^{5/3}(t_c - t), \tag{4.16}$$

where t_c is the coalescence time for the binary, meaning that chirp mass is an observable quantity.

From equation 4.17, the total power radiated by the emission of gravitational waves from binary as they are inspiraling towards each other is given by (35)

$$P = \frac{dE}{dt} = \frac{32}{5}\left(\frac{M_c\omega_{gw}}{2}\right)^{10/3}, \tag{4.17}$$

where E is the radiated energy and other symbols have their meanings as mentioned above.

The emission of gravitational waves results in the loss of energy, leading to a gradual decrease in the orbital radius over time ($E_{orbit} \propto -R^{-1}$). According to Kepler's third law, a decrease in the orbital radius (R) corresponds to an increase in the orbital angular frequency (ω_s). Conversely, an increase in ω_s leads to an increased power radiated (eq. 4.17), causing further reduction in R. This self-reinforcing process eventually leads to the coalescence of the binary system after a sufficiently long time-scale.

From the equations provided above, we observe that as the the binary system approach for coalescence, both the amplitude and frequency of the waveform increase. This phenomenon is commonly known as "chirping" [1].

Inserting the numerical reference values in the equation 4.16, will help us in giving more intuitive understanding of the time scales involved. The reference chirp mass for the binary has been chosen to be 1.21 $M_\odot$, with mass of each object to be 1.4 $M_\odot$ and τ is the time until coalescence (35).

$$\begin{aligned} f_{gw}(\tau) &= 134Hz\left(\frac{1.21M_\odot}{M_c}\right)^{5/8}\left(\frac{1s}{\tau}\right)^{3/8} \\ \tau &= t_c - t \\ \tau &= 2.18s\left(\frac{1.21M_\odot}{M_c}\right)^{5/3}\left(\frac{100\ Hz}{f_{gw}}\right)^{8/3} \end{aligned} \tag{4.18}$$

The detection of radiation at different frequencies can be analyzed. At 10 Hz, we get the radiation emitted about $\tau \sim 17$ mins before coalescence. At 100 Hz, the radiation from the last two seconds leading up to the merger is captured, and at 1 kHz, the radiation from the last few milliseconds is obtained. When the gravitational wave frequency (f_{gw}) is 1 kHz, the separation R between the two 1.4 $M_\odot$ bodies is estimated to be $\sim$ 33 kilometers (eq. 4.12). Such a small separation can only be achieved by extremely compact objects like black holes or neutron stars. Thus in the aLIGO frequency band, we focus on the gravitational wave radiation from compact binary objects (particularly binary black holes) for the thesis (1).

---

[1] because, when translated into air pressure waves, it resembles the sound produced by a bird's chirp

Also, the number of cycles N_{cycles} that can be detected by the instrument having the frequency sensitivity from f_{low} to f_{high}, given as

$$N_{cycles} = \frac{1}{32\pi^{8/3}}({M_c}^{-5/3})(f_{low}^{-5/3} - f_{high}^{-5/3}) \tag{4.19}$$

Thus, a low mas binary with say 25+25 $M_{\odot}$ will have more detectable cycles as compared to a higher mass binary with 100+100 $M_{\odot}$.

In the inspiral phase above, the calculations are performed in flat space-time background. However for the binary systems consisting of black holes and neutron stars, the Schwarzchild geometry exists and because of this, there is a minimum radial distance beyond which stable circular orbits are not permitted. Thus, there exists an Innermost Stable Circular Orbit (ISCO) located at r_{isco}, beyond gravitational fields are strong and cause the objects to plunge into each other. In Schwarzchild geometry,

$$r_{isco} = 6M \tag{4.20}$$

The orbital frequency at r_{isco} is given by

$$f_{isco} = \frac{1}{6\sqrt{6}(\pi)}\frac{1}{M} \tag{4.21}$$

which is about twice the orbital frequency at the ISCO. This expression is valid for non-spinning and non-eccentric black hole with equal mass binaries. f_{isco} is always inversely proportional to the total mass of the binary and decreases non-linearly with increasing mass ratio (36),(37).

Till now we did not take the cosmological expansion into account in our analysis, however taking cosmological expansion into account, for a source at redshift z, we have the following modifications:

- The chirp mass is replaced by

$$\mathcal{M}_c = (1+z)M_c. \tag{4.22}$$

- The observed frequency is redshifted with respect to the source frequency as

$$f_{obs} = f_s/(1+z). \tag{4.23}$$

- The factor $1/r$ in equation 4.13 in the amplitude is replaced by luminosity distance d_L as $1/d_L$.

This loss of energy in the inspiral phase (equation:4.17) causes the orbit to shrink over time, a process known as inspiral, whose physics has been explained above. Eventually, the binary system reaches a critical point where the objects merge together, resulting in a violent event known as a merger. This phase is separated with the inspiral phase by f_{isco} and relatively brief compared to the inspiral phase. The merger phase is not adiabatic and full GR equations must be solved in order to provide the representation of the system dynamics. Following the merger, the newly formed object undergoes a phase called ringdown, during which it settles into a stable state, emitting gravitational waves which is described by the calculations of the quasi-normal modes (38), (39) [2]. The ringdown phase is characterized by a rapidly decreasing amplitude (as shown in fig. 4.3) as the energy of the system is quickly dissipated. This phase is even shorter than the merger phase. The merger and the ringdown phase are roughly separated by a frequency f_{rd} called the ringdown frequency. Fig. 4.2 illustrates the waveform during the binary coalescence and fig. 4.3 plots the absolute value of the gravitational wave strain as a function of frequency for the different phases of the binary coalescence.

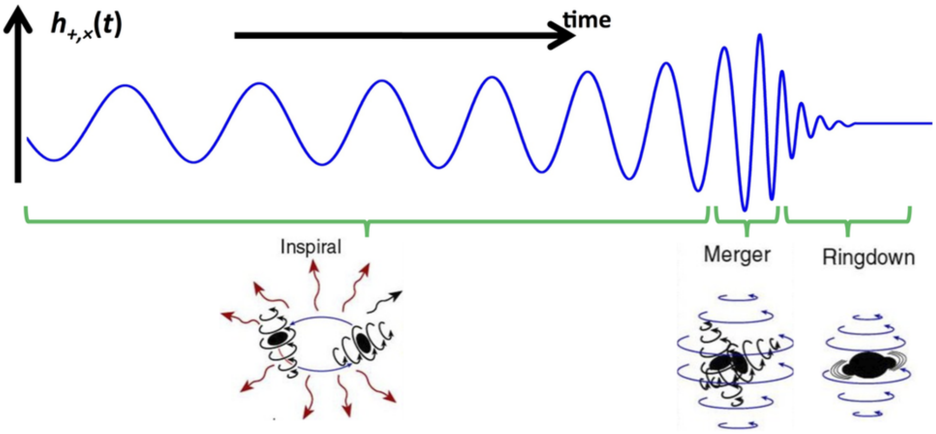

Figure 4.2: An illustration of the subsequent phases of binary coalescence: Inspiral, Merger and Ringdown. The blue curve represents the change in the gravitational wave strain amplitude $h_{+,x}(t)$ varying with time. Fig. credits : (40).

While it is beyond the scope of this thesis to provide an exact calculation of the quasi-normal modes, an important thing is to note that the ringdown frequency also depends inversely on the total mass M and increases with increasing mass ratio of the binary (42), (36).

4.4 Detection

While electromagnetic radiation is detected via its interaction with matter, gravitational waves are detected by the distortion they create in the fabric of spacetime itself. Gravitational wave detectors, such as the Advanced Laser Interferometer Gravitational-Wave Observatory (aLIGO), function as Michelson-Morley interferometer (43), (6) and is designed to detect the gravitational waves in the frequency range from 10 Hz to 10 kHz (1). The basic layout of a michelson interferometer is displayed in Fig. 4.4. The main components include a laser source, a beam-splitter, mirrors and a detector. The process begins with a laser beam that travels through a beam-splitter, splitting it into two similar beams. These beams then proceed in the two equal-length perpendicular arms towards the mirrors (each 4km for aLIGO (6)), where they are reflected. The laser beams retrace their paths and travel back to the beam-splitter, where they recombine and travel to

---

[2] the characteristic oscillations that occur in a physical system after it has been perturbed and then allowed to evolve towards equilibrium

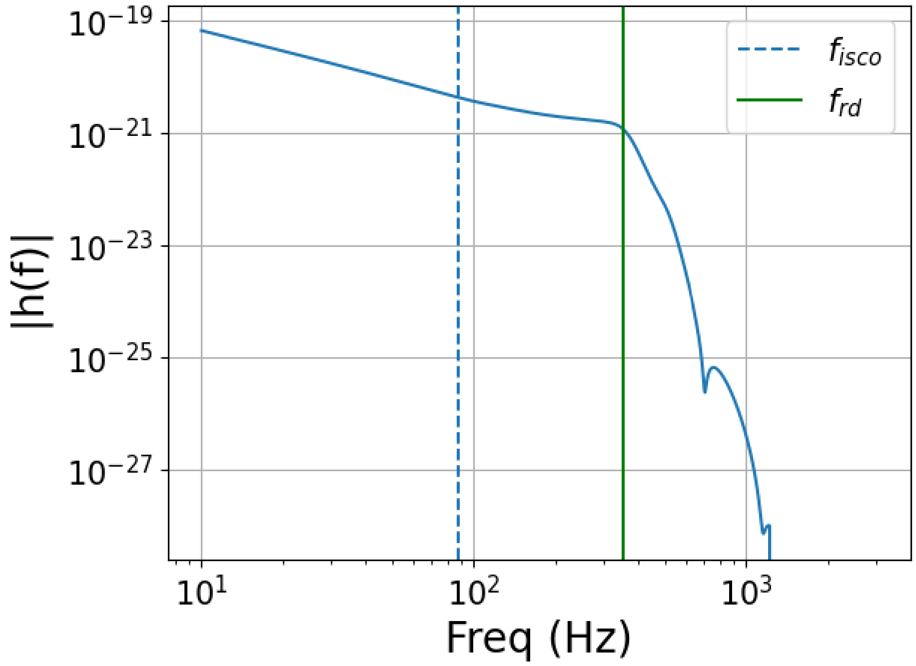

Figure 4.3: The absolute value of the fourier transform of the gravitational wave strain amplitude $|h(f)|$ plotted as a function of frequency for a 25+25 $M_{\odot}$ binary (blue solid line). Corresponding $f_{isco} \sim 87Hz$ and $f_{rd} \sim 354Hz$ have also been marked (blue dotted line and the green solid line). The gravitational waveform has been generated using IMRPhenomXPHM (41) waveform model as explained in section 5.3

the detector to create an interference pattern. When no gravitational waves is passing through Earth, the laser beams recombine in phase, resulting in constructive interference and a bright signal at the detector. However, when a gravitational wave passes through, it causes a slight stretching and squeezing of spacetime, altering the lengths of the arms and introducing a phase shift between the beams. This leads to destructive interference and a dimmer signal at the detector. The length variations caused by gravitational waves are incredibly small. For two masses separated by a distance L, the change in their distance is approximately:

$$\frac{\delta L}{L} \sim h \tag{4.24}$$

where h is the gravitational wave strain. For a black hole binary, each of 10 $M_{\odot}$, separated by the cosmological distance of 100 Mpc, $h \sim 10^{-21}$ (7).

These variations are comparable to just a thousandth of the width of a proton, resulting in a phase shift of the laser beams on the order of a trillionth of their wavelength, Detecting such minute changes requires a high level of sensitivity and noise reduction in the detectors (7).

Several developments have been made to the initial design of LIGO, resulting in aLIGO (6). These advancements aim to improve sensitivity, stability, and instrumentation. Notably, aLIGO is designed to provide a significant increase in strain sensitivity, with a factor of 10 improvement over a wide frequency range. Additionally, aLIGO extends the lower end of the frequency band to 10 Hz, compared to the previous limit of 40 Hz. These enhancements enable aLIGO to detect even fainter gravitational wave signals and capture

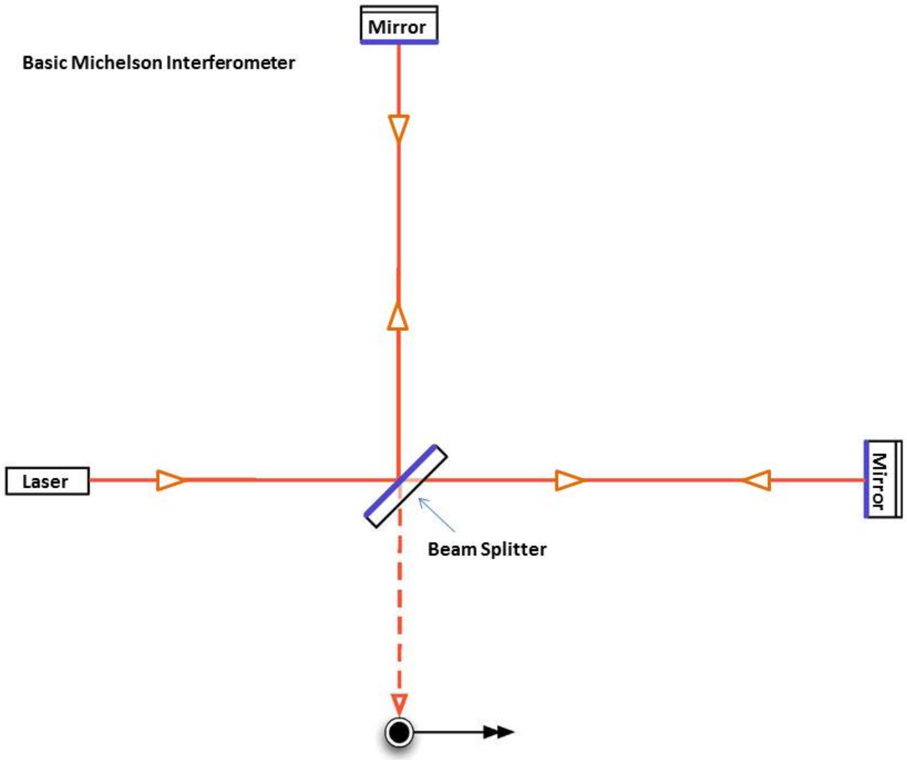

Figure 4.4: The diagram for a basic Michelson Interferometer. The Michelson Interferometer operates by splitting a single light beam from the laser into two using a beam-splitter. These two beams travel perpendicular paths, bounce off mirrors at the ends, and then recombine at the detector (shown in black). This simplified depiction outlines aLIGO's operational concept, but the actual design is intricately detailed in (6). Fig. credits : (44).

events at lower frequencies, expanding the capabilities of the observatory for studying the universe as also explained in (6).

Power Spectral Density

Despite the efforts to reduce noise, the output of the detector contains a significant amount of noise. The form of the gravitational wave signal, $h(t)$, must be known with an accuracy similar to the normal changes of the noise in order to recover a signal considerably smaller than the noise. To investigate it, we follow the discussion in (45). The output of the detector can be described as $s(t) = h(t) + n(t)$, where $h(t)$ represents the expected gravitational wave signal and $n(t)$ denotes the detector noise.
The power spectral density (PSD) of the detector output characterizes the distribution of average power of a signal in the frequency domain. Making some relevant assumptions [3], the noise can be fully characterized using the one-sided noise power spectral density

---

[3] To simplify the analysis, it is commonly assumed that the noise in the GW detector is stationary and follows a Gaussian distribution with a mean of zero as explained in (45).

(PSD) $S(f)$ as,

$$< \widetilde{n}(f)\widetilde{n^*}(f') >= \frac{1}{2}\delta(f-f')S(f). \tag{4.25}$$

where $< .. >$ represents an ensemble average over multiple noise realizations, $\widetilde{n}(f)$ is the fourier transform of $n(t)$ and $*$ denotes the complex conjugate while $\delta(f-f')$ denotes delta function.

As the detector input and output are both real function, $\widetilde{n}(-f) = \widetilde{n^*}(f)$ which implies that $S(f)$ is an even function.

Using Fourier transform and the property of even functions, PSD can be derived as :

$$|\overline{n(t)}|^2 = \int_0^\infty df S(f) \tag{4.26}$$

where $|\overline{n(t)}|^2$ is the mean square noise amplitude. Thus, the power spectral density (PSD) possesses a favorable characteristic in which its integration across all positive frequencies yields the average square amplitude of the noise within the detector.

Taking $n(t)$ to be dimensionless, the PSD should have the units for Hz^{-1}. A related quantity is the amplitude spectral density (ASD), which is the square root of the PSD and gives the amplitude of the signal as a function of frequency. It has the units $Hz^{-1/2}$ and is the most frequent plotted quantity in literature. The figure 4.5 plots the ASD for various LIGO runs.

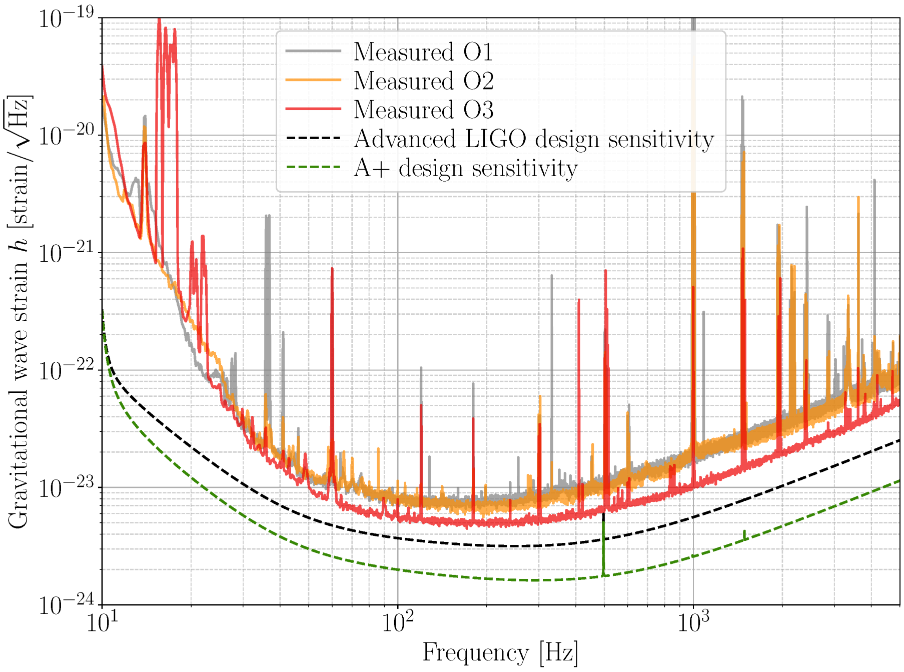

Figure 4.5: The plot shows the Amplitude Spectral Density (ASD) versus frequency for various LIGO runs, namely 01, 02, 03. The curve also plots the ASD for aLIGO and A+ upgrades. Fig credits: (46).

The sensitivity of earth-based detectors is limited with the lower limit imposed by seismic noise, the upper limit by "shot noise" (basically not having enough photons to sample the interferometer path difference at high frequencies). Further sensitivity upgrades to the current gravitational wave observatories and building of new observatories (47), (48) (49), (50) will help in increasing the detection probability of the lensed gravitational waves (12).

4.5 Lensing of Gravitational Waves : A Theoretical Approach

The gravitational waves and electromagnetic waves (EM) differ in their nature and main characteristics. While the electromagnetic radiation is produced by the motion of microscopic charges and are oscillations in the electromagnetic field, the gravitational waves are ripples propagating in the fabric of spacetime. The EM waves, produced by the motion of large number of microscopic charges are incoherent superposition of waves with dipolar structure, while the gravitational wave radiation, produced by the bulk motion of the masses give rise to coherent superposition of waves with quadrupolar structure as elucidated in (51). A notable benefit of gravitational waves in comparison to electromagnetic waves lies is that while electromagnetic waves can be subject to alterations due to interstellar gas or medium gravitational waves remain impervious to such interstellar conditions during their propagation.

Furthermore, regarding the lensed electromagnetic rays, the process of detection involves categorizing the lensed photons based on their respective angular orientations. The degree of accuracy achievable is constrained by the angular resolution capabilities of the optical detector. However for the gravitational waves, in addition to the completely different detection methodology with interferometer length difference measurement (as explained above in section 4.4), lensed events are statistically distinguished as identical events using GW templates and Bayesian analysis techniques (52), (19), (53) and the precision of this distinction is limited by the time resolution of the interferometer (54).

We focus on Gravitational Lensing of gravitational waves by CBCs with aLIGO. Just like electromagnetic radiation, the gravitational waves are also lensed by the intervening mass (7). The physics of lensing remains the same as we already discussed in Chapter 3, but only in certain approximation called Geometrical Optics approximation.
In this approximation, the lensed gravitational waves can be understood as propagating towards us along specific, discrete ray-like trajectories, i.e. all the wave effects such as diffraction are neglected. Geometrical Optics is valid for wavelength $\lambda << R_s$ where $R_s = 2M$, the Schwarzschild radius of the lens [4]. This can also be written as $ft_d >> 1$. This is generally true in the case of lensing by electromagnetic waves (23).

Within the frequency range of aLIGO, (10 Hz to 10 kHz), the wavelength of gravitational waves is significantly smaller than the size of a galaxy, as established by (55). As a result, geometric optics appropriately elucidates the behavior of the gravitational waves lensed by massive galaxy lenses (mass $\sim 10^{10}\ M_{\odot}$). Thus, geometrical optics is valid for the strong lensing of gravitational wave signals. The associated lens is called 'macrolens' and the corresponding images are called 'macroimages'. The lensing setup for the macrolens, involving the source position in the source plane, macrolens position and mass in the lens plane and the observer is hence called the macromodel setup. In case of strong lensing, the signal gets scaled by a factor $\sqrt{\mu}$ (4.5.1 and (22)) where μ is the magnification due to strong lensing, called macro-magnification, as introduced in 1.

---

[4] it can be seen as the length scale of the lens, for more please refer to (7)

However in the case of lensing of gravitational waves by objects in the mass range 10 to 10^4 $M_\odot$, (this mass range is for the isolated point mass (8)) in the aLIGO frequency band, the wavelength of gravitational waves is comparable to the Schwarzschild radius associated with the mass of the lens, $\lambda \geq R_s$ ($ft_d \leq 1$) (23),(8) which leads to the diffraction effects because of which the gravitational waves can no longer be considered as rays and the wave effects must be taken into account in the analysis. The associated lenses are called 'microlens' and the corresponding images are called 'microimages'.

4.5.1 Gravitational Lensing of Gravitational Waves: Considering Wave effects into account

As already discussed, the wave effects are needed to be taken into account for studying the effects of microlensing. In this and the consecutive sections we will delve deeper into the intricacies of microlensing of gravitational waves and thus, the wave optics.

The gravitational wave radiation emitted from the source is in principle coherent as the different radiation bundles emerge from the same source. The need of the wave optics can be understood as the two images are situated very close to the critical curve, their mutual time delay is very small (13). If this time delay happens to be shorter than the coherence time of the radiation, it is reasonable to anticipate the occurrence of interference. This is the regime of interest for this thesis as elaborated in 6. Thus this section will focus on deriving the equation for the amplitude of the lensed wave and the form it takes in both the wave optics and geometrical optics limit.

Derivation of Amplification Factor

This derivation is based on (56), (22) and (12). I invite the interested reader to look at these references for more details.

We consider a point source of radiation, emitting gravitational waves of frequency ω, which pass by a thin lens and reach the observer. For simplicity, consider the space-time to be Minkowskian with the inclusion of a minor perturbation resulting from the potential of the lens, where the influence of the gravitational potential is localised within a small region around the lens. The amplitude of the perturbation is $\phi(\vec{r}, t) = \tilde{\phi}(\vec{r})e^{-i\omega t}$ and the propagation equation for the same as be written as

$$(\nabla^2 + \omega^2)\tilde{\phi} = 4\omega^2 U \tilde{\phi}. \tag{4.27}$$

We consider a set of spherical coordinates (r, θ, Φ) with the origin centered on the source and the polar axis pointing towards the lens in order to characterize this system. The wave amplitude without lensing is calculated as $\tilde{\phi}_0(r) = Ae^{i\omega r}/r$ (56).

Assuming the lensing to be taking in a plane, the equation above can be solved using Kirchoff's integral (57) (33)).

As per (56), the amplification factor is defined as the ratio of the lensed and unlensed amplitude as,[5]

$$F(\vec{r}) = \frac{\tilde{\phi}(\vec{r})}{\tilde{\phi}_0(\vec{r})} \tag{4.28}$$

Using thin-lens approximation, the possible paths from source to observer could be restricted such that only the which go straight from the source to a deflection point (within the tiny region of $U(\vec{r}) \neq 0$) again go straight from to the observer contribute to the final expression, compared with the huge distances from the lens to the lens and the source from the observer. Thus performing the computations and taking relevant approximations, following diffraction integral formula is obtained for Amplification factor $F(f)$ (using the normalized units $\vec{x}, \vec{y}$ as introduced in section 3.2) (13):

$$F(f) = \frac{D_s R_E^2 (1+z_L)}{D_L D_{LS}} \frac{f}{i} \iint_{\mathbb{R}^2} d^2\vec{x} e^{2\pi f t_d(\vec{x},\vec{y})}. \tag{4.29}$$

As the function $F(f)$ is complex-valued, the total amplification, $|F|$, and phase shift, θ , can be obtained as $F(f) = |F|e^{i\theta f}$ and using the dimensionless frequency, $w = 8\pi M_L(1+z_L)f$ (22), and taking the Inverse Fourier transform, we obtain $F(t)$ as, (12)

$$F(t) = \int dxdy\delta(T_d(\vec{x}, \vec{y})) \tag{4.30}$$

The derived form for $F(f)$ or $F(t)$ above represents the amplification factor that corresponds to the interferences between the microimages, taking into account the effects of diffraction.

If $h(f)$ represents the unlensed waveform, the lensed waveform $h_L(f)$ is then (11)

$$h_L(f) = F(f)h(f) \tag{4.31}$$

Amplification factor in Geometrical Optics Limit: In the limit of Geometrical Optics, the integral 4.29 is a highly oscillatory (as $f >> t_d^{-1}$) and is only contributed by the stationary points of the time delay function t_d (56), which are the positions of the images as discussed in section (3.5). Thus, corresponding $F(f)$ can be written as

$$F(f) = \sum_j |\mu_j|^{1/2} e^{i\pi(2ft_{d,j} - n_j)}, \tag{4.32}$$

where j denotes the image position, μ_j is the image magnification and n_j are respective Morse indices for the images, being $0, \frac{1}{2}, 1$ for Type 1, Type II and Type III image respectively, corresponding to the overall phase shift of $n\pi$ ((33), (58)).

This means that the gravitational lensing introduces an extra phase of $e^{-i\pi/2}/e^{-i\pi}$ for Type II/Type III image with respect to Type 1 image (59). The corresponding phase shifts can used for the identification of strongly lensed gravitational wave signals (59) (60).

Similar to the wave optics, the corresponding lensed waveform is given as 4.31 where $F(f)$ for this case corresponds to the geometrical optics regime.

---

[5] this means that in no lensing limit $|F| = 1$

Chapter 5

Lensing Configuration and Analysis Techniques

5.1 Goals of this Chapter

Building upon the understanding of lensing of gravitational waves in the previous chapter, this chapter starts with outlining the lensing configuration setup to simulate the population of microlenses around type 1 macroimage, providing a detailed description of its components. Then we focus on the relevant expressions for quantitatively analysing the impact of microlensing on type 1 signal which are effective micro-amplification and mismatch. This will finally build up in elucidating the methodology employed for the relevant procedure which involves explaining the utilization of the software LensingGW and the calculation of the amplification factor $F(f)$.

5.2 Setup of the Lensing Configuration

The basic setup is done using the same lensing configuration as described in section 3.2. To summarize the system consists of a source, lens and observer plane, (with the respective objects being in their respective plane) and the thin lens approximation and the single-plane lensing are assumed. The FlatLambdaCDM model is assumed throughout the analysis (1 and (28)).

The source plane consists of a binary black hole and is located at the redshift $z_S = 1$. For simplicity, this work only considers gravitational waveforms from binary black hole systems that have non-spinning components and no orbital eccentricity, in the aLIGO frequency band (4.3.1). The lens plane is located at the redshift $z_L = 0.5$ and consists of a macrolens of mass 1e10 $M_{\odot}$. The SIS profile has been adopted for the macrolens (3.7.2). The einstein radius for the same is labelled as θ_{SIS}. In the source plane, the source is positioned at an angular separation of $\eta_{SIS} = x\theta_{SIS}$, referred to as the macro-impact parameter. This parameter signifies the location of the source relative to the center of the SIS macromodel.

With the basic description for macromodel (4.5) complete, following will be the characteristics for the distribution of the microlenses in the setup:

- The masses of the microlenses have been taken to be in the range [0.08 to 1.5] $M_\odot$. The lower limit of 0.08 $M_\odot$ was chosen because it is the minimum mass required for star formation as per literature (61),(62), (63). The upper limit of 1.5 $M_\odot$ is set because massive stars ($> 1.5M_\odot$) will complete their life in $\sim$ 1.5 Gyr and by restricting the lens masses to this value, the evolutionary effects on the stars during the light travel time from the source to the lens plane could be ignored. In addition, limiting the mass range in this way improves the computational efficiency of future calculations.

- The microlenses are assumed to be all Point Masses (as discussed in section 3.7.1)

- The stellar masses for the distribution were drawn from the IMF.
  For $\xi(m) = \frac{dN}{dm}$, specifying the the number of stars N formed initially in the mass range m to $m + dm$ (64) and the total number of lenses to be n_{tot}, the IMF is defined as a probability density function (PDF) $p(m) = \xi(m)/n_{tot}$, (equation 5.1) which follows
  $$1 = \int_{m_1}^{m_2} p(m)dm, \tag{5.1}$$
  where m_1 and m_2 are upper and lower mass limit.
  A number of investigations have been made to see if a single IMF can be used to characterize all early-type galaxies and if it changes with redshift, however there is currently no agreement on a universal form of IMF that can describe all early-type galaxies and the evolution of IMF with redshift, as highlighted in (23). However, Chabrier IMF is most commonly used to fit early-type galaxies, including those studied through strong lensing (65) (66) and is well established in the literature for modeling low mass stars (67) (68). Therefore, it is assumed to be universal for analysis in the thesis unless stated explicitly (68) (69)). The functional form of the Chabrier IMF (as PDF) is given by the formula below (70):
  $$p_{chabrier} = \begin{cases} N_1 \frac{1}{m} e^{-\frac{1}{2}\left(\frac{log_{10}m - log_{10}0.079}{0.69}\right)^2}, & m < 1M\odot \\ N_2 m^{-2.3}, & m \geqslant 1M\odot \end{cases} \tag{5.2}$$
  where N_1 and N_2 are normalization constants. The masses of microlenses from the IMF have been derived as follows:
  One normalisation constant is used to make the distribution continuous and the other was used to make the integral of probability density equal to one. The cumulative distribution function (CDF) is then defined for the probability density function and the Brent's method (71) has been used to invert the CDF which yields mass samples from the probability density function. Fig. 5.1 shows the probability density function for the IMF for the mass range taken.

  To strike a balance between the maximum number lenses that can be simulated and computational efficiency, 200 lenses have been considered for the analysis throughout the study 8.6 [1]

---

[1] The investigation of a particular study case was also done using 300 lenses. As the overall trend remains the same, we choose to use 200 lenses throughout the study. The computational time increases by 3+hrs for 300 lenses as compared to 200 lenses.

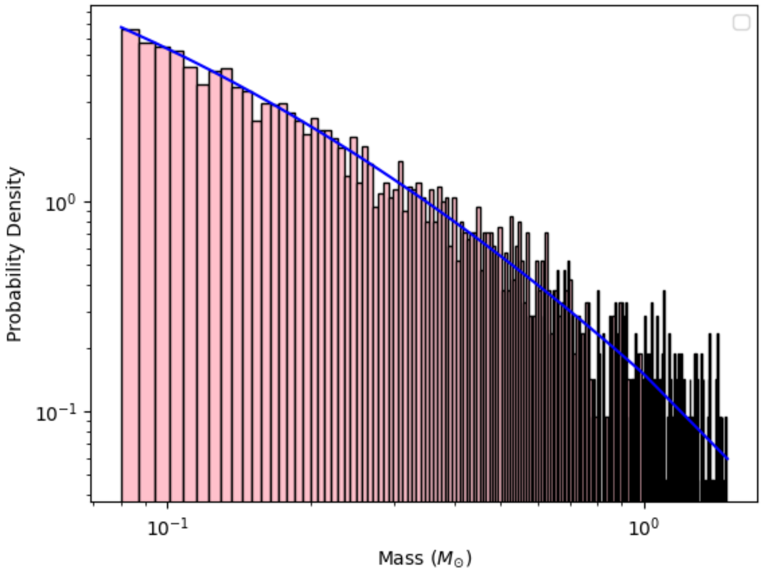

Figure 5.1: For an illustrative sample of 3000 masses drawn from Chabrier IMF, the blue line plot in shows the probability density function (eq. 5.2) and the histogram bins represent the probability density for the mass range m to $m + dm$.

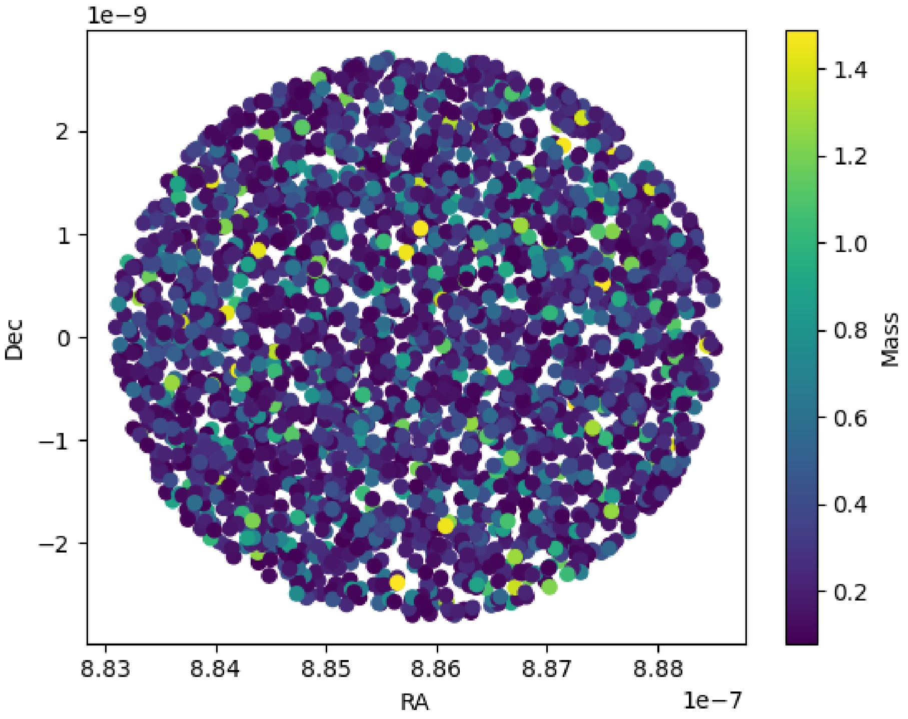

Figure 5.2: An illustrative sample of 3000 masses drawn from Chabrier IMF, distributed in using a sample surface density of 27 $M_\odot/\mathrm{pc}^2$ around the Type 1 macroimage. The masses of the individual lenses are represented in solar masses ($M_\odot$) and are depicted with the color plot. The Type 1 macroimage is taken to be located at the center with the Right Ascension and Declination [RA,DEC] in radians $\sim$ [8.86e-07 and -4.23e-22].

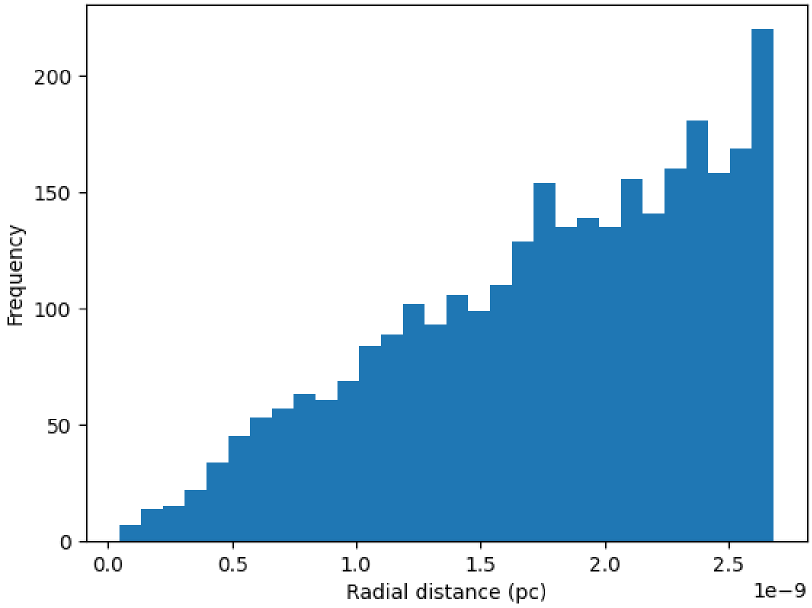

Figure 5.3: The uniformity of the distribution of the lenses can be well illustrated by plotting a histogram of the radial distance (in parsecs) from the center of macroimage position. As expected, the number of lenses increase with increasing the radial distance due to increase in the circumference as we move to larger radial distance.

- The distribution of the microlenses will be done around Type 1 macroimage. The type 1 macroimage is formed close to the critical curve and microlenses from the galaxy halo or intracluster medium play a significant role in terms of their net microlensing effect at close proximity to the critical curve (12),(72); (73), as also elucidated in section 6.2.2). Fig 5.2 and 5.3 shows a sample of 3000 masses drawn from the Chabrier IMF, uniformly distributed around Type 1 macroimage located at the center.

Figure 5.4 is a good conceptual illustration of the lensing configuration. However, in contrast to a single microlens surrounding the macroimage, the aim is to investigate multiple microlenses around type 1 macroimage.

This basic setup will be used throughout the thesis, with some modifications to study different parameter spaces. These changes will be explained when discussing the specific analyses. The implementation of microlensing setup described above for a population of microlenses is the key contribution to the existing code (git repository - (25)) for the microlensing by a single microlens.

5.3 Quantification of the effect of Microlensing

From the figure 5.4 it is evident that the presence of microlenses impacts the lensed gravitational wave signal from the macroimage. Subsequently, our attention turns towards

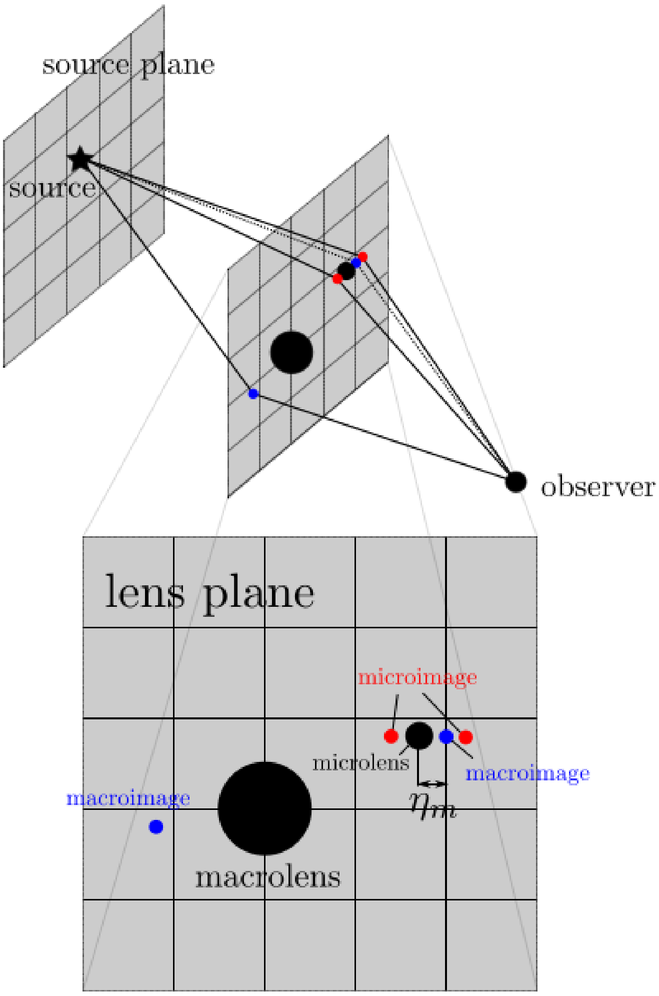

Figure 5.4: A visual representation of the microlensing of gravitational waves by a single microlens from (22). The source, lens and observer are shown in their respective planes. In the geometrical optics regime, the gravitational waves from the source can be treated as rays. In the absence of the microlens, lensing by macrolens can be treated in the geometrical optics regime. These rays being lensed by the macrolens (big black dot in the lens plane), take discrete paths, passing through the macroimage positions (blue dots in the lens plane) and arrive at the observer. However, in the presence of a microlens (small black dot on lens plane located at a distance η_m from the macroimage (called micro-impact parameter), the beam (shown in dotted lines) might split and pass through various points on the lens plane, corresponding to microimage positions (red dots). The microimage also occur at stationary points of time delay function (22)

quantifying the influence exerted by microlensing on the Type 1 macroimage.

The quantification of the effect of microlensing involves distinguishing the impact of microlensing from the macrolensing. Thus, for the same the lensing from the macromodel is considered first and then the consider the lensing by both the macrolens and the microlenses is considered together.
We can work in the geometrical optics regime for the macromodel due to the considerable mass of the lens as discussed in section 4.5. Given that the lensing by the macromodel

produces type 1 macroimage corresponding to the image magnification $\sqrt{\mu}$, the lensed waveform $h_{L,macro}$ including the effect of macrolensing by Type 1 macroimage on the intrinsic waveform $h(f)$ is: (22)

$$h_{L,macro} = \sqrt{\mu}h(f), \tag{5.3}$$

For SIS lens model, for type 1 macroimage, if $\eta_{SIS} < 1\theta_{SIS}$, then the corresponding $F(f) = \sqrt{\mu}$ (for detailed derivation, please refer to (74))).

Similarly, the waveform, $h_{L,full}$ including the effects of both Type 1 macrolensing and microlensing due to a population is

$$h_{L,full} = F(f)h(f). \tag{5.4}$$

From 5.4 it can be seen that microlensing introduces frequency dependent modulations in the signal in both the phase and the amplitude (8), (12), (21).

The gravitational waveform $h(f)$ for the binary black hole is generated via IMRPhenomXPHM model (41), implemented via the PYCBC package (75). This model approximates the strain signal for specific binary masses ($M_{\odot}$) in the defined frequency range (aLIGO band 1). Additionally, the PYCBC package calculates the Power Spectral Density (PSD) aligned with aLIGO's design sensitivity within this range (4.4).
The waveform of the binary system is characterized by both intrinsic parameters, encompassing the masses of the two binary black holes, and extrinsic parameters, which include the luminosity distance (d_L) of the source (35).

Using the information above, two important parameters: Effective Micro-magnification and Mismatch can be defined for quantification of the effect of microlensing on the macrolensed waveform(see ch 7 of (35) for the background expression development).

- **Effective Micro-Magnification**: The parameter indicates the change in overall amplification of the signal due to microlensing. It is calculated as

  $$\mu_m = \frac{(h_{L,full}|h_{L,full})}{(h_{L,macro}|h_{L,macro})} \tag{5.5}$$

  where,

  $$(a|b) = 4Re\int_{f_{high}}^{f_{low}} \frac{a(f)b^*(f)}{S_n(f)} \tag{5.6}$$

  is the noise-weighted inner product of two waveforms a(f) and b(f), where $*$ denotes the complex conjugate. It is integrated over the frequency range f_{low} to f_{high} and weighted by the power spectral density $S_n(f)$ of the detector (as discussed in section 4.4). By calculating the noise-weighted inner product of $h_{L,full}$ and $h_{L,macro}$, the frequency dependence is removed so that the amplitude change due to population of microlenses can be measured.

  For the type 1 macroimage, the amplitude of the gravitational wave is amplified by a factor $\sqrt{\mu}$, which we refer to as the macro-amplification value. The corresponding

effective micro-amplification is given as $\sqrt{\mu}_m$.
$\sqrt{\mu}_m > 1$, signifies a net amplification and $\sqrt{\mu}_m < 1$ indicates a net de-amplification of the macrolensed waveform (from type 1 macroimage) due to microlensing.
In the strong lensing studies, the macro-amplification of the lensed signal is used to calculate the luminosity distance of the binary (19). This parameter holds significant importance in cosmological investigations associated with strong lensing studies, such as localization studies and the computation of the Hubble Constant. The uncertainty in the measurement of d_L propagates in proportion to the uncertainty in $\sqrt{\mu}$ (19). Consequently, any deviation of $\sqrt{\mu_m}$ from 1 introduces uncertainties in $\sqrt{\mu}$, with the resultant error propagating in amplitude in proportion to $\sqrt{\mu_m}$ and thereby influencing the accuracy of the luminosity distance measurement.

- **Mismatch**: The match indicates how similar the waveforms are when optimally aligned in time and phase. $1 - match$ gives the mismatch, indicating the corresponding differences in two waveforms. The waveform overlap is defined as:

$$O[h_{L,macro}, h_{L,full}] = \frac{(h_{L,full}|h_{L,macro})}{(h_{L,full}|h_{L,full})(h_{L,macro}|h_{L,macro})} \tag{5.7}$$

the match $M[(h_{L,macro}, h_{L,full}]$ is defined as the waveform overlap maximized over time and phase,thus mismatch is $1 - M[(h_{L,macro}, h_{L,full})]$

$$\mathbb{M} = 1 - \ max_{(t,\phi)}\, O[h_{L,macro}, h_{L,full}] \tag{5.8}$$

where again $(a|b)$ is defined as the noise-weighted inner product of two waveforms $a(f)$ and $b(f)$.

Due to the normalisation, the mismatch does not encode any information about the macrolensing magnification μ and thus is a pure measure of the effect of microlensing effects. As intrinsic parameters such as the mass and spin of the binary are determined by GW phasing, it is likely for the microlensing to effect these parameters. We will use the mismatch quantification in percentage in the thesis.
The value of 0% indicates the perfect coincidence between two waveforms while the value of 100% indicates null correlation. Microlensing effects become detectable when there is a significant waveform mismatch and the literature considers a cut-off of around 3% for typical aLIGO events for the microlensing to be detectable (24),(12), (23), (22). Such an analysis helps estimate the effects on inference of gravitational wave source parameters.

5.4 Procedure for Lensing by Macromodel and Amplification Factor Calculation

The initial step in this procedure entails the computation of gravitational lensing caused by the macromodel, a task accomplished using software package LensingGW. Subsequently, the process for determining the amplification factor denoted as $F(f)$ as per equation 4.30 will be elucidated.

5.4.1 LensingGW: a PYTHON package for lensing of Gravitational Waves

LensingGW (11) is a python package for lensing of gravitational waves. It works on a forked version of Lenstronomy, which is a python package for gravitational lensing (76). LensingGW is used in the thesis for calculating the lensing by the macromodel by facilitating the calculation of essential parameters such as image positions, time delays, and corresponding image magnifications. The content of this section draws from the work presented in (11). Readers who wish to delve into further details are encouraged to consult this reference.

Finding the image positions comes with a challenge as it requires one to solve equation 3.29 which is a system of non-linear, algebraic and coupled equation of two variables. Furthermore, the gravitational potential might not be analytic. Thus, finding the complete solution to these equations often relies on giving initial values to the algorithm (77), which is not a known quantity. Without making any prior assumptions about the image structure, LensingGW develops the methodology specifically designed to handle various length scales in lens potential while maintaining fast performance.

The numerical solver of LensingGW involves a two-step procedure for finding the image positions for the macromodel, as illustrated below:

- First it separates the lens system to identify macrolens in case microlenses are also present in the model.
- The image plane is ray-shooted to the source plane via equation 3.29. The region where the search is performed for the images is centered on the source position with the size specified by the user. Pixels whose projected distances from the source are local minima are iterated over through adaptive grids. The true solutions must precisely reproduce the source position when ray-shooted. Hence, approximate solutions should minimize the distance between their ray-shooted position and the actual source position within a locally. The pixels that reach the desired precision are saved as images while the remaining tiles that still contain candidate solutions undergo further processing. These candidate solution tiles become the centers for the next set of grids, with each grid twice the size of the original pixel. The tiling and iteration process continues on the new grids until either no more candidate regions are found or the pixel size reaches a safe threshold of 10^{-20} arcsec.[2].

Fig. 3.1 shows an illustrative diagram for the procedure. The calculated image position serves as an input parameter for calculation of the corresponding image magnification, critical curves and caustics as per the discussion in 3.4. The time delay is calculated by implementing equation 3.26. For more details into the code please see the reference (78).

---

[2] this is orders of magnitude below the typical separation between the microimages (11))

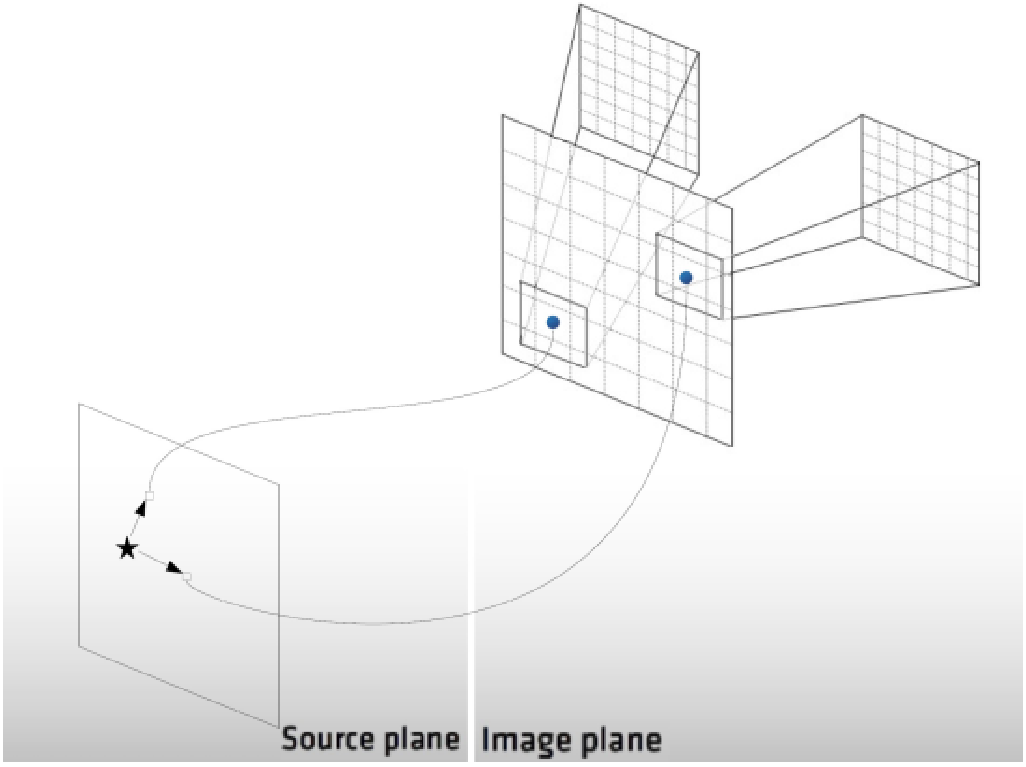

Figure 5.5: An illustrative image of the iterative procedure of LensingGW. The arrows show the image plane being divided into pixels and ray-shooted to the source plane via lens equation with. The pixels whose projected distance from the source (star in the figure) is local minima are iterated over through the adaptive grid method. The process terminates when no more candidate regions are found or the minimum pixel size is reached. Fig. credits (11).

5.4.2 Calculation of Amplification factor using Wave Optics

The calculation of amplification factor for equation 5.4 involves calculating the integral in the equation 4.30. The calculation of this integral is done using a similar procedure mentioned used in (12).

The git repository (25) uses the procedure in (12), which will also be used in the thesis for the calculation of amplification factor. The integral is evaluated in the lens plane ($x - y$ plane). The lens plane is covered with a dense grid and for each point we calculate T_d and the histogram of these time delay values gives $F(t)$, taking the inverse fourier transform of its derivatives gives $F(f)$. For simplicity we choose $\phi_m(\vec{y})$ to correspond to time delay of type 1 macroimage. It is important to note that the lensing potential for calculating the amplification factor in equation 3.26 includes the effect of both the macrolens and the microlensing population (23).
As we have a finite range for the computation of $F(t)$, an important numerical step in the process is applying apodization using cosine window function to the computed $F(t)$. It removes the oscillatory behaviour of finally computed $F(f)$ at low frequencies (12).
This approach differs from the one opted in (23) and (79) in the direct computation of the

area within constant time delay intervals, rather than using contour integrals to calculate $F(t)$ [3] The main advantage of this method over the traditional method used by (23) and (79) is that it avoids the divergence of the contour integral at local minima/maxima of time delay function, which otherwise would be needed to be handled separately as explained in (79).

Integration Window Size

The identification of the appropriate window size is also an important step in the process for the calculation of amplification factor by multiple microlenses as it differs from the same used for calculation of microlensing effects by a single microlens.

The calculation of the integral in eq. 4.30 requires calculating the area of the region between two contour lines corresponding to consecutive values of time delay which theoretically would require using an area window in the lens plane that encloses all contour lines with time delays close to the arrival time of the macroimage under consideration. A broad window for integration would not be practical because we need a very fine resolution in time delay for computing microlensing effects (22). Thanks to the stationary phase approximation, the integral in equation 4.30 is primarily influenced by the region surrounding the macroimage, therefore the chosen integration area can be justified by increasing it to double the area while maintaining the same resolution. As per (22) the initial area coverage is sufficiently accurate, increasing the grid size will not meaningfully change the outcome and extending the integration window further will likely yield a similar result. However, if our original integration range is too narrow, widening the window will produce a noticeably different and more precise amplification curve.

More about the characteristics of the amplification factor (along with the appropriate integration window size) will described in the chapter 6 I proceed onto the investigation of the parameter space.

---

[3] The contour integral methodology requires calculating amplification factor by summation over all time delay contours, C_k as $F(t) = \sum_k \oint_{C_k} \frac{ds}{|\vec{\nabla}_{\vec{x}} t_d|}$, where ds is the is the infinitesimal length along the contour. The formula for which has a divergence at the image positions as per equation 3.29. For more details please refer to (79), (23).

Chapter 6

Effect of Microlensing on signal from Type 1 macroimage

6.1 Goals of this Chapter

Building upon the understanding from all the chapters above, the overall goal of this chapter is to analyse the impact of microlensing by a population of microlenses on the strongly lensed gravitational wave signal from type 1 macroimage. Detailed analysis of the variation amplification factor and systematic investigation of the variation of mismatch and effective micro-amplification will be performed for the parameters in consideration. The chapter will conclude with a general discussion of results.

6.2 Investigation of the Parameters

It will be analysed how microlensing on signal from type 1 macroimage is affected due to variation of the following parameters:

- Surface density of microlenses around the Type 1 macroimage
- Source position
- Stellar IMF
- Total mass of the binary producing Gravitational waves
- Mass ratio of the binary producing Gravitational waves.

The basic setup is the same as described in section 5.2 and the respective setup details will be described as the particular parameter is considered for the investigation.

6.2.1 Effect due to variation in density of microlenses around the Type 1 macroimage

Note: The section will commence with the setup of the problem for studying the parameter in interest. We will then explore the solution of the macromodel for this specific setup, utilizing LensingGW which will be fundamental in the final calculation of amplification factor. Next, we will delve into the behavior of amplification factor, $F(f)$ with frequency. Understanding the macromodel solution and the amplification factor curve will be crucial in gaining a comprehensive understanding of the variation of all parameters under consideration. After this, we will finally investigate the effect due to the variation density of microlenses around the Type 1 macroimage utilizing effective micro-amplification and mismatch.

Setup

The configuration of the lensing arrangement follows the methodology discussion in Section 5.2, accompanied by forthcoming explanations of the specifications for studying the variation with density. The macro-impact parameter is chosen to be $\eta_{SIS} = 0.1\theta_{SIS}$ as not only it is close to the typical value found in the literature around type 1 macroimage (23), it also aids in computational efficiency [1]. The mass of the binary producing the gravitational wave is considered to be 30+30 $M_{\odot}$ in the source plane as there is an excess of mergers with the mass of primary black hole close to 30 $M_{\odot}$ (80). This corresponds to 60+60 $M_{\odot}$ in the detector frame following the equation (4.22).[2]. All discussions in this and upcoming sections will correspond to the computations in the detector frame, i.e. taking the effect of redshift into account.

The masses of microlenses are drawn from the Chabrier IMF. The typical value of the stellar densities found around the Type 1 macroimage are found to be varying from 30 $M_{\odot}/\text{pc}^2$ to 107 $M_{\odot}/\text{pc}^2$ (72), (23). 25 random mass distributions are drawn from the Chabrier IMF and for each distribution the amplification factor $F(f)$ was calculated for the following densities: [30, 50, 70, 90, 107] $M_{\odot}/\text{pc}^2$.

The distribution of microlenses around Type 1 macroimage requires obtaining the position of the type 1 macroimage. For obtaining the position, the macromodel setup will be considered and the image position is obtained using LensingGW as discussed below.

Output from LensingGW: Lensing due to Macromodel

As per the discussion in section 3.7.2, the lensing as per the macromodel configuration described in section 5.2 leads to the formation of two macroimages, (as the source is taken to be placed at $0.1\theta_{SIS}$ from the macrolens center/galactic center), as shown in the fig 6.1.

The type 1 macroimage (the image on the right size in Fig. 6.1 is recognised by identifying the minima of the time delay function and following are the key numerical outputs for the same obtained as a result of lensing by the macromodel:

- Macro-Magnification: 10.99
- Image Position (Right Ascension (RA), Declination (DEC), relative to galaxy center): (8.85e-7, -4.23e-22) radians

---

[1] The computational time increases exponentially as we decrease the value of $\eta_{SIS} = 0.1\theta_{SIS}$

[2] the effect of redshift in the chirp mass also reflects in the total mass with the individual masses in the source frame multiplied by (1+z), where z is the redshift of the source.

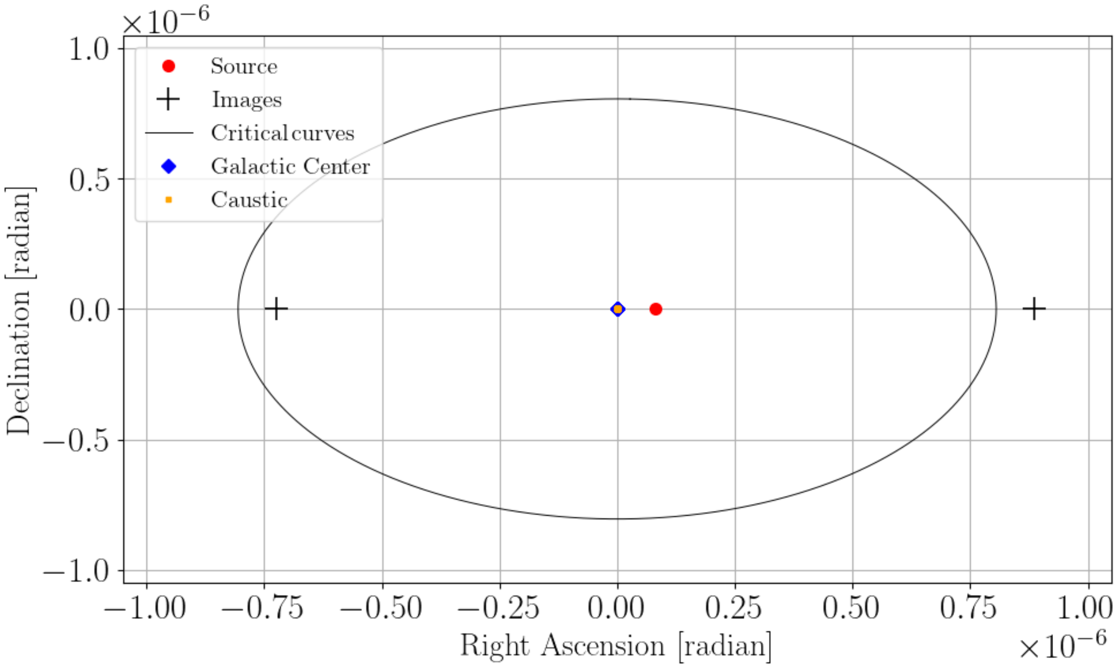

Figure 6.1: The figure shows the macroimages '+' recovered by LensingGW for a Macromodel setup consisting of a SIS lens of mass 1e10 $M_\odot$. The coordinates are relative to the galaxy center or macrolens center (blue diamond) at [0,0]. The off-axis source ($\eta_{SIS} = 0.1\theta_{SIS}$) is shown as a red dot, while the critical curve (det A= 0 as discussed in 3.4) is shown in black line. The critical curve mapped to the source plane generates point caustic at coordinates [0,0] marked by orange dot. The lensing by the macrolens produces two images with the image on right being the type 1 image recognised by finding the minima of the time delay surface.

The information obtained in the output above is used in the final calculation of the amplification factor for the complete lens model using wave optics. The image position serves as a crucial parameter for placing lenses around the type 1 macroimage, while the macro-magnification (μ) is reserved for subsequent evaluation to determine the mismatch/effective micro-amplification.

Amplification Factor

After the macromodel solution, the value for the amplification factor was calculated using the procedure described in section 5.4.2. An important thing in the process was determination of the integration window size as explained in 5.4.2. Taking inspiration from the existing code (git repository - (25)) resolution size was chosen to be sufficiently smaller than the typical separation between the multiple microlenses in the lens plane. Following the discussion in section 5.4.2, it was found that an integration area slightly extending beyond the area encompassed by the distribution of microlenses around macroimage is sufficient for the computations throughout the thesis. To validate the selection, the integration area was expanded to twice the original dimensions (keeping the resolution same

[3]) Upon doing so, it was ascertained that the outcomes did not significantly improve the accuracy. This demonstrated that the original integration area was adequate for the calculation and amplifying it further would not meaningfully improve the accuracy. It has been graphically illustrated in 8).

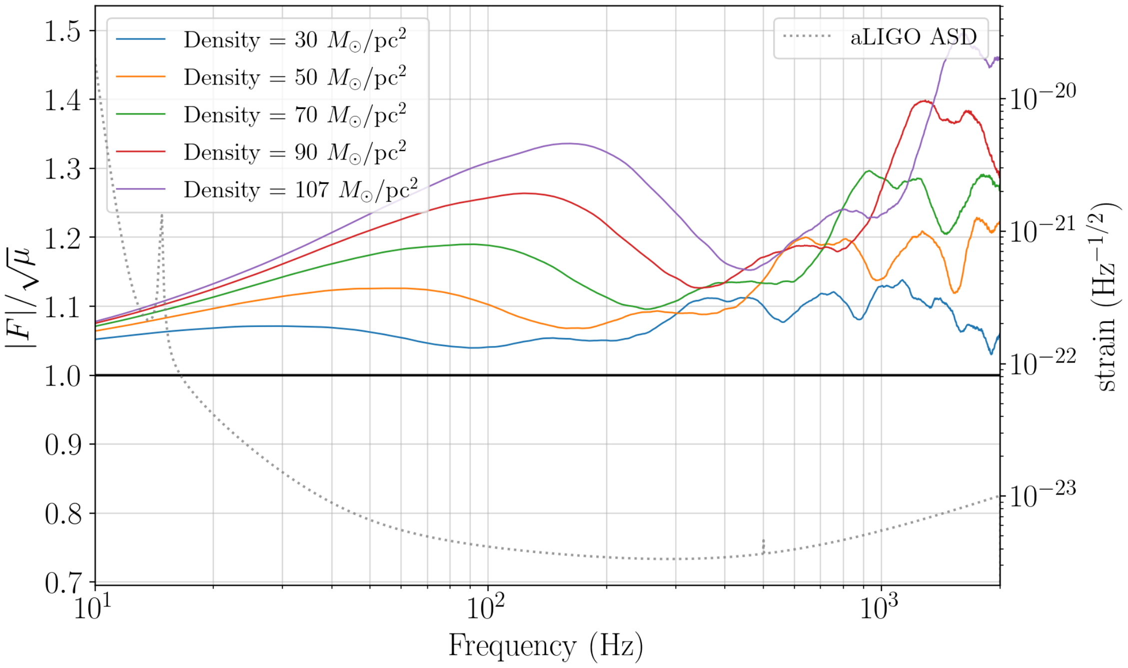

Figure 6.2: The figure shows the amplitude of the amplification factor $|F|$ normalised by the strong amplification $\sqrt{\mu}$ varying with frequency for different densities of microlenses around Type 1 macroimage. The values of density are taken to be [30, 50, 70, 90, 107] $M_\odot/\mathrm{pc}^2$. The solid black line illustrates the $|F|$ being equal to the strong lensing amplification value $\sqrt{\mu}$. The ASD for aLIGO is plotted in grey along with the corresponding value of strain. The curves approach strong lensing amplification value at low frequencies and microlensing effects start dominating from higher frequencies.

Variation of Amplification Factor vs frequency

Before proceeding further, it is important to understand the variation of $F(f)$ curve with frequency for any particular density, say 107 $M_\odot/\mathrm{pc}^2$, that will remain universal for all the densities in consideration in this section and upcoming discussions (refer 8.2 for plots for different densities and mass distributions) [4]. The discussion in this section has been inspired from (8), (23), (12).

Fig. 6.2 shows that the curve approaches the strong lensing value, 1 at low frequencies ($f << t_d^{-1}$), (where $|F|$ approaches $\sqrt{\mu}$). At low frequencies, we approach no-microlens limit as the wavelength of the gravitational wave signal is very large as compared to the scale of the population of lenses, called R_s ($\lambda >> R_s$). Thus, at very low frequencies,

---

[3] This increased the computation time four folds

[4] The computational time in generating single $F(f)$ vs f curve is approximately 5 hours.

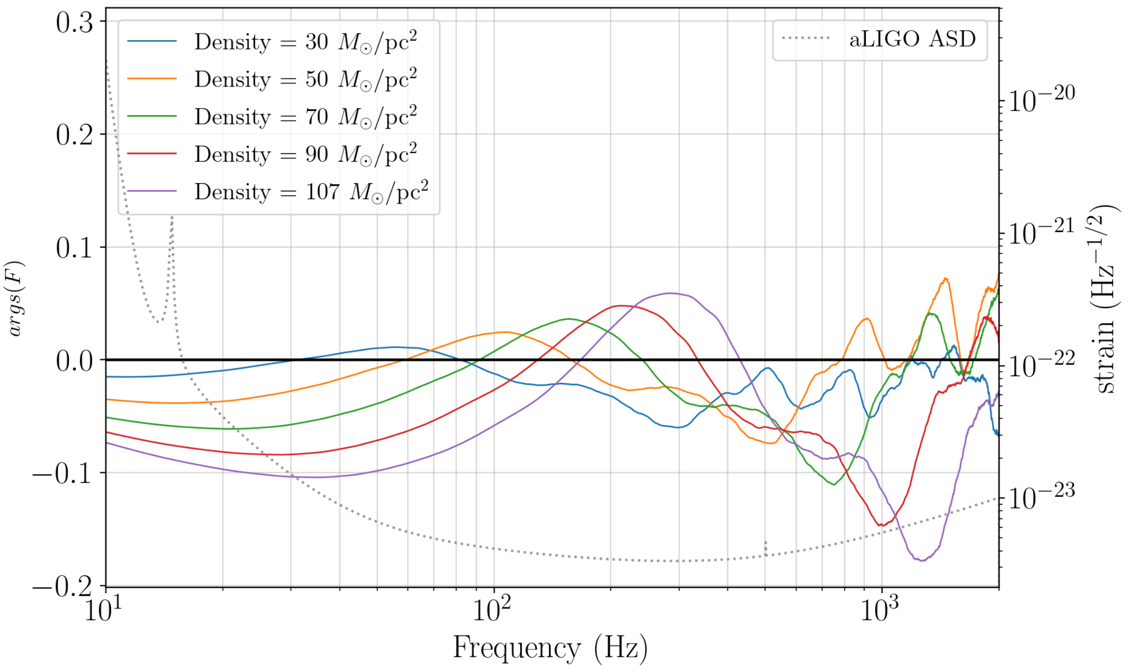

Figure 6.3: The figure shows the phase of the amplification factor $args|F|$ varying with frequency for different densities of microlenses around Type 1 macroimage. The values of density are taken to be [30, 50, 70, 90, 107] $M_\odot/\mathrm{pc}^2$. The solid black line corresponds to the phase shift 0 associated to the Type 1 macroimage. The ASD for aLIGO is plotted in grey along with the corresponding value of strain. The cuves approach strong lensing phase shift at low frequencies and microlensing effects start dominating from higher frequencies.

the signal is only amplified by the macroimage's magnification. The is essentially due to diffraction effects as any obstacle whose size is significantly smaller than the wavelength of a wave will have a negligible effect on the propagation of that wave and is called 'wave optics suppression'. Similarly, for the curve showing the phase shift, we recover a phase shift of 0 corresponding to type 1 image (as discussed in section 4.5.1.
As we go to higher frequencies, $\lambda \leq R_s$ $(f \geq t_d^{-1})$ the effects for microlensing start dominating and the curve shows stronger distortions as can be seen in Fig. 6.2 and 6.3). This is due to the formation of many microimages at significant time delays with respect to type 1 macroimage (as per (23)). The microimages as formed from the low mass microlenses have low time delay values as expected from equation 3.26, thus as the frequency increases, more and more microimages satisfy the criteria $f \geq t_d^{-1}$ and thus a greater number of microimages begin to contribute to $F(f)$ which leads to both the amplitude and phase of the amplification factor becoming more random and chaotic.

Not shown in the curves above, at very high frequencies, $\lambda << R_s$, we approach geometrical optics limit. Approaching this limit, both amplitude and phase variation curves (6.2 and 6.3) show rapid oscillations around the geometrical optics limit and the average magnification over frequency becomes independent of frequency, as expected from the formula 4.32 (also represented in Fig. 1 of (23))

Variation with the Density

Now that we know about the characteristic of curve, we can study the variation of the curve with the density. First a description of how density variation affects $F(f)$ will be provided which will be followed by the mismatch and effective micro-amplification calculation for different densities.

Amplification Factor variation with Density

For a particular mass distribution drawn from the Chabrier IMF, as the density is increased, we see that there are stronger modulations in both the phase and amplitude (Fig. 6.2 and 6.3). The modulations also start from the lower frequencies for higher densities. This behavior can be explained by the fact that as the density of microlenses increases, it leads to the formation of a larger number of significantly amplified microimages, especially those with large time delays (or microlensing can start dominating from even lower frequencies), as per (23). This can be understood referring to equation 3.36. The lens potential due to a microlens is given as $\Psi(x) \sim m_k ln|x_k - x_0|$, where m_k and x_k denote the mass and potential of kth microlens located around point x_0. Therefore, if there are N microlenses of mass m located close together around some point x_0, such that $|x_k - x_0| << 1$, then the net effect of those microlenses will be similar to that of a single microlens of mass Nm located at x_0 (23). In other words, when microlenses are clustered closely together, they effectively act as one larger lens with a mass equal to the sum of the individual microlens masses and thus produces microimages with larger time delays and amplification (23).
It can also be seen that the curves approach to the strong lensing amplification value at low frequencies and the phase shift corresponding to the Type 1 macroimage independent of the density due to wave optics suppression. The results obtained above are qualitatively inline with the results obtained in the study (23). [5]

Effective Micro-Amplification and Mismatch v/s Density

More insight can be obtained by analysing the variation of effective micro-amplification and the mismatch with the density. The calculation of effective micro-amplification and mismatch is carried out as detailed in section 5.3. The value of the macro-amplification was obtained as an output from LensingGW as discussed in section 6.2.1 and will be utilized for the caluclation.

Fig. 6.4, 6.5 show the variation of effective micro-amplification with density. It can be

---

[5] As shown in Figures 6.2 and 6.3, the plots are generated for a particular sample of masses drawn from the Chabrier IMF. The apparently systematic variation in the curves with increasing density is an artifact that results from using the same mass distribution for each curve. Since the same set of masses simply comes closer together with increasing density, the relative positions and contributions of the individual masses remain similar, leading to a more systematic pattern. However, when different mass distributions are used for different densities, the variation in the curves does not appear as systematic as expected. While using different mass distributions at different densities results in less systematic variation in the curves due to the sensitivity of the results to the specific masses and their positions within each sample, the overall trend of amplification and time delays increasing with density persists. It can be well illustrated by section 8.2

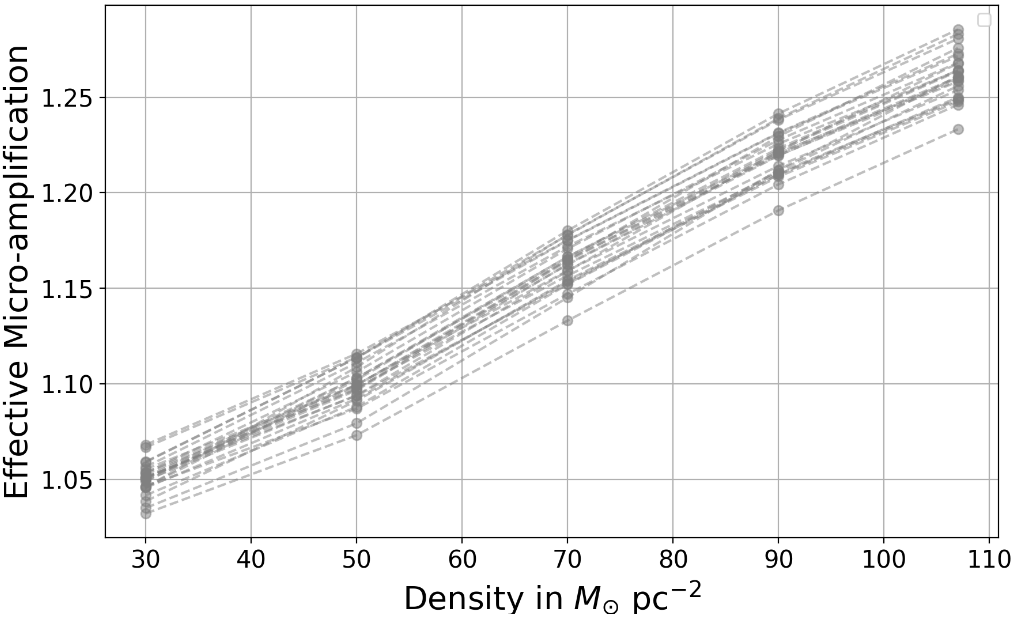

Figure 6.4: The figure shows the effective micro-amplification variation with the density of microlenses around Type 1 macroimage for the particular setup. The values of density are taken to be [30, 50, 70, 90, 107] $M_\odot/\mathrm{pc}^2$. The grey plots show the same calculated for the 25 random mass distributions drawn from the Chabrier IMF for the particular setup. The effective micro-amplification increases with increase in density for all the distributions.

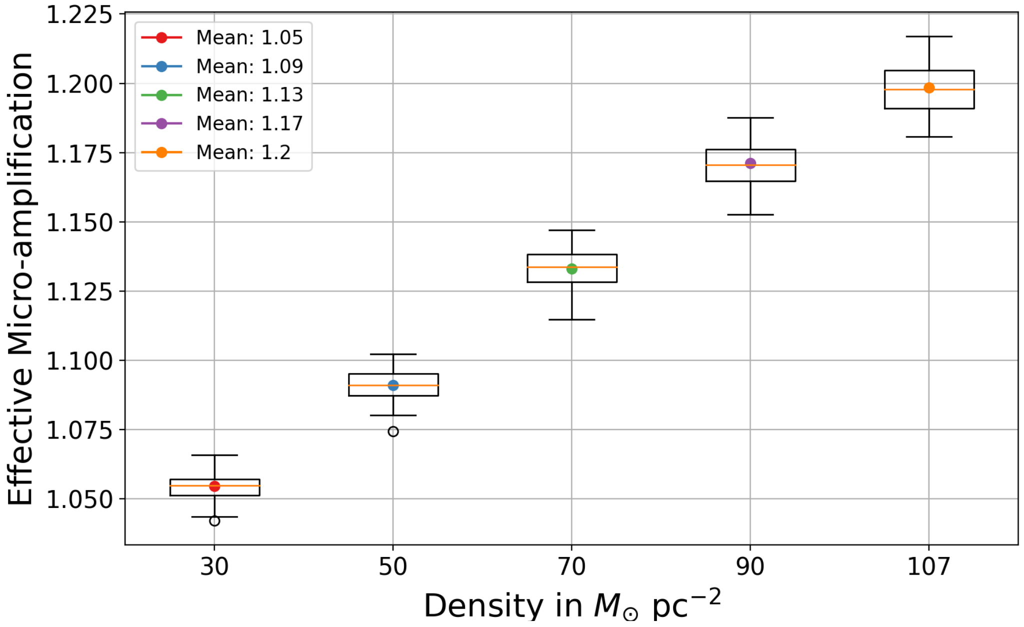

Figure 6.5: The figure shows the box plot corresponding to figure 6.4 for the variation of the effective micro-amplification with density with the corresponding mean values computed for the respective densities. A box plot consists of a rectangular box that spans the interquartile range (IQR), which encompasses the middle 50% of the data. The orange line inside the box represents the median value, dividing the data into two equal halves. The whiskers extend from the box to indicate the range of the remaining data, typically reaching up to 1.5 times the IQR from the quartiles. Any data points beyond this range are considered outliers and are plotted individually as circles in the figure. The box plot also depicts increasing trend of effective micro-amplification with increasing density.

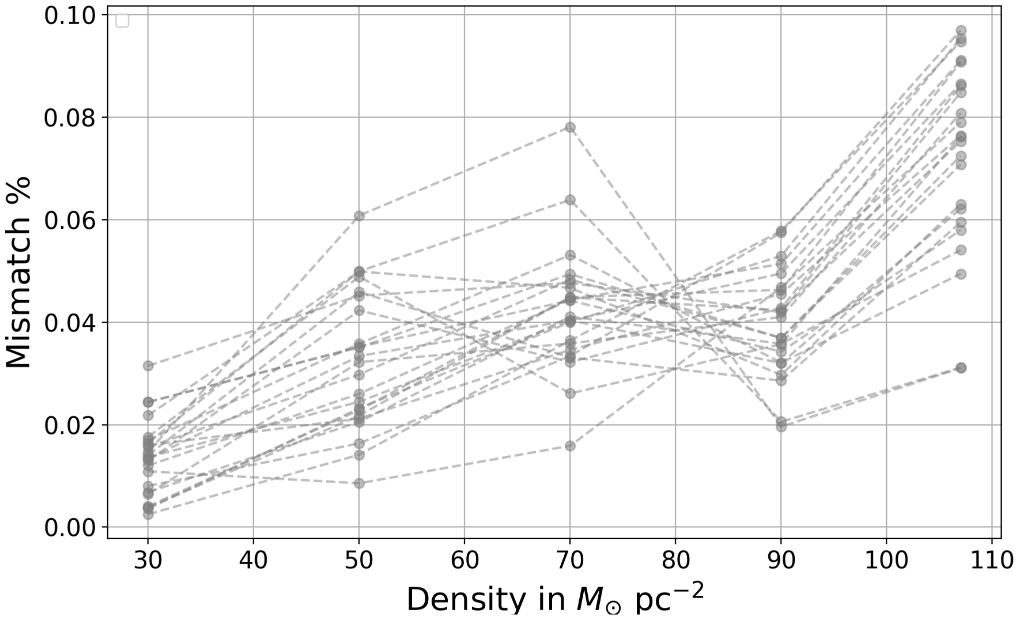

Figure 6.6: The figure shows the mismatch variation with the density of microlenses around Type 1 macroimage for the particular setup. The values of density are taken to be [30, 50, 70, 90, 107] $M_\odot/\mathrm{pc}^2$. The grey plots show the same calculated for the 25 random mass distributions drawn from the Chabrier IMF for the particular setup. The mismatch shows a complicated trend with increase in density.

seen that the effective micro-amplification increases in proportion to the density, which means that as the density of microlenses increases, the waveform from the macroimage is amplified in a corresponding manner by the microlenses. Fig. 6.5 shows the box plot corresponding to the mean values of the amplification factor. The overall increase is ~ 0.21 as the value of density increases from 30 to 107 $M_\odot/\mathrm{pc}^2$. This trend is expected as the value of the amplitude of amplification factor increases with increase in density from Fig. 6.2. As the value of the effective micro-amplification is always greater than 1 it indicates that there will be the net-amplification of the macrolensed waveform (from type 1 macroimage) due to microlensing as the density increases.

From Fig. 6.6, it can be seen that the mismatch however does not increase in proportion to the increase in density and rather follows a complex trend sensitive to the particular mass distribution. The mismatch variation is expected to be different as compared to micro-magnification due to sensitivity of the calculation to both the amplification effects and phase shift effects caused by microlensing 5.3. Fig. 6.7 shows that the average mismatch increases as the density increases from 30 to 70 $M_\odot/\mathrm{pc}^2$ however the increasing trend settles from 70 $M_\odot/\mathrm{pc}^2$ to 90 $M_\odot/\mathrm{pc}^2$ after which it increases again for 107 $M_\odot/\mathrm{pc}^2$. The overall increase in the value of the mismatch is ~ 0.06 % as the density increases from 30 to 107 $M_\odot/\mathrm{pc}^2$. The complex behavior observed in microlensing can be attributed to the findings of a study on microlensing by a single microlens (22).
As shown in Fig. 6.8, this study demonstrates that the mismatch value is highly sensitive to the location (the micro-impact parameter and the relative angle) of the microlens with

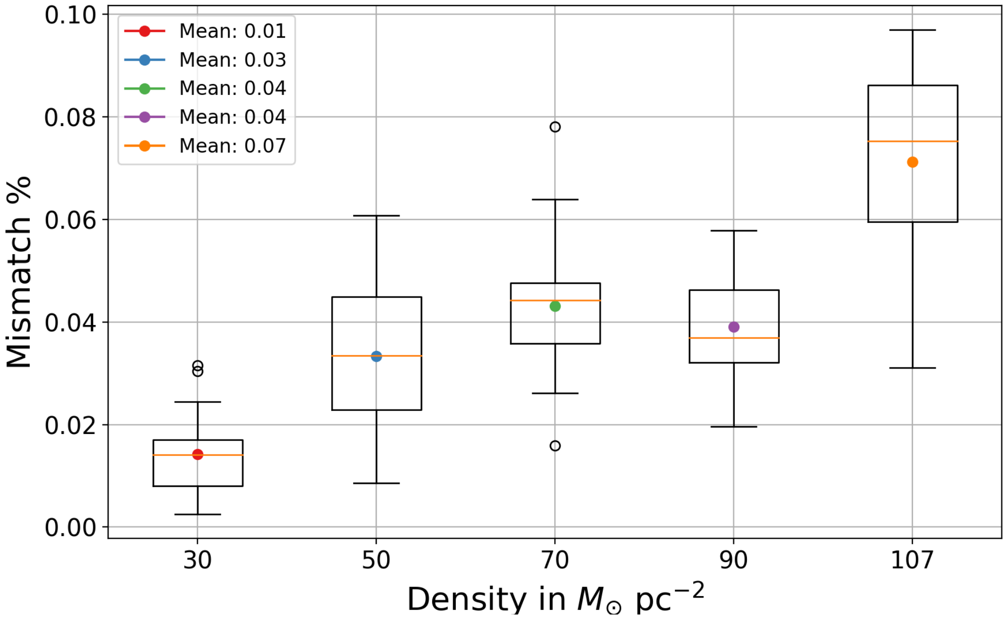

Figure 6.7: The figure shows the box plot corresponding to figure 6.6 for the variation of mismatch with density with the mean values of the mismatch computed for the respective densities. The basic description of the box plot is the same as in the caption of fig. 6.5. The box plot also depicts the complicated behaviour of mismatch with the increase in density, however higher mismatch can be expected for very high densities ($\sim 107\ M_\odot/\mathrm{pc}^2$) as compared to very low densities ($\sim 30\ M_\odot/\mathrm{pc}^2$).

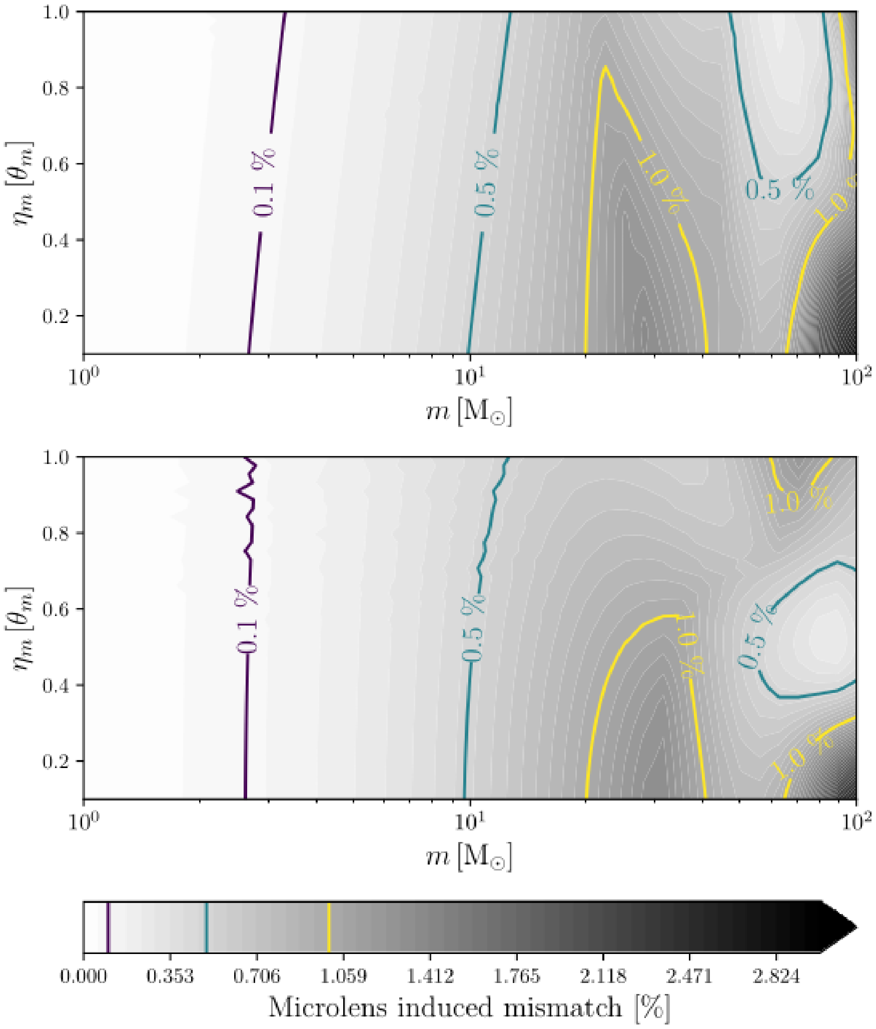

Figure 6.8: The figure, sourced from the literature (22), illustrates a contour plot depicting the mismatch resulting from microlensing by a single microlens around the Type 1 macroimage. In this study, the macromodel employs the same parameters as those used in the thesis. However study uses different binary mass in the source plane. The plot spans various mass values and micro-impact parameter values represented as $\eta_m[\theta_m]$ in the horizontal and vertical axis respectively. The upper panel corresponds to a relative angle of 135 degree measured with respect to the straight line from the SIS lens center to macroimage position in the simulation, while the lower panel corresponds to a relative angle of 180 degrees. The study illustrates the sensitivity of the mismatch to the location of microlens around type 1 macroimage as the mass of a single microlens increases.

respect to the type 1 macroimage position. Thus, as the densely clustered microlenses behave as a single larger lens, overall higher mismatch can be expected as the effective mass increases but the increase is highly sensitive to the location of microlenses around type 1 macroimage. As per the results, the mismatch is expected to increase for very high densities such as 107 $M_{\odot}/\mathrm{pc}^2$ as compared to very low densities, 30 $M_{\odot}/\mathrm{pc}^2$.
The mismatch however very well below 3 % threshold.

In the literature (22), it has been reported that for the case of a single microlens ($mass \leq 10M_{\odot}$), the effective micro-amplification shows minimal deviation from unity($\sqrt{\mu} \sim 10$), and the mismatch between the waveforms is at a sub-percentage level (as also demonstrated in Fig. 6.8.)

6.2.2 Effect due to Variation with the Source Position

In this section, the focus will be on studying the effect of varying the source position (or macro-impact parameter). It is an important parameter to be investigated as the variation of the same results in the variation in the value of the macro-amplification as can be seen in the section 3.7.2, equation 3.46). As macro-amplification value is often utilised in strong lensing studies such as (14), therefore graphs in this section will be plotted with respect to the same ($\sqrt{\mu}$).

Setup

The configuration of the lensing arrangement follows the methodology discussion in Section 5.2, accompanied by forthcoming explanation of the ensuing specifications for studying the variation with the source position.

For the investigation, the source position has been varied to the different values as $\eta_{SIS} = [0.03, 0.1, 0.8]\theta_{SIS}$ (common values for lensing of type 1 macroimage as per (23)).[6]. The mass of the binary producing the gravitational wave is considered to be 60+60 $M_{\odot}$ in the detector plane as taken in 6.2.1. The study has been done for the 10 random mass distributions from the Chabrier IMF for each source position for the density 90 $M_{\odot}/\text{pc}^2$.

Output from LensingGW: Lensing due to Macromodel

The software LensingGW is used to calculate lensing by the macromodel corresponding to each source position. The relevant numerical outputs from the software (along with the corresponding macro-amplification value) to the corresponding source positions are listed in the Table 6.1. The type 1 image is again recognised by the minima of the time delay function.

	Source Position [η_{SIS} [θ_{SIS}]]	Macro-magnification [μ]	Macro-amplification [$\sqrt{\mu}$]	Image Position [RA, [radians]]	Image Position [Dec, [radians]]
	0.03	34.33	5.86	8.29e-07	-2.43e-21
	0.1	10.99	3.32	8.85e-07	-4.23e-22
	0.8	2.25	1.50	1.44e-06	-4.23e-22

Table 6.1: Output from LensingGW for the lensing by macromodel for varying source position η_{SIS}. The macro-magnification and type 1 macroimage position (relative to the galaxy center) are obtained for each macromodel lensing setup.

The following outputs obtained are used in the calculation of the amplification factor, effective micro-amplification and mismatch. In addition to the numerical outputs, the corresponding critical curves obtained for each setup will play a significant role in further analysis.

Variation with the Source Position

The impact of source position variation on $F(f)$ will be discussed first, following which the effects on the mismatch and effective micro-amplification for different source positions

---

[6] The computational time increases exponentially with the decrease in the value of η_{SIS}

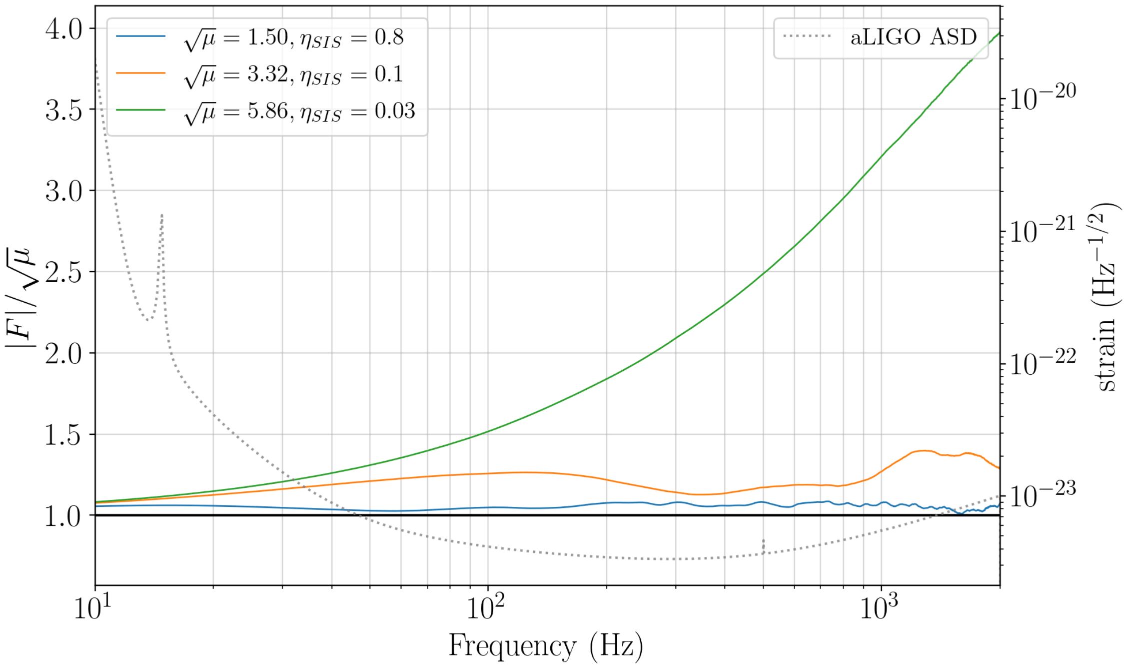

Figure 6.9: The figure shows the amplitude of the amplification factor $|F|$ normalised by the respective macro-amplification $\sqrt{\mu}$ varying with frequency for different source positions $[\eta_{SIS} = [0.03, 0.1, 0.8]\theta_{SIS}]$ and hence macro-amplifications [$\mu =$ 34.33,11.00,2.25 for a particular density 90 $M_{\odot}/\mathrm{pc}^2$. The solid black line illustrates the $|F|$ being equal to the strong lensing amplification value $\sqrt{\mu}$. The ASD for aLIGO is plotted in grey along with the corresponding value of strain. The amplitude of the amplification factor increases strongly as the macro-amplification value is increased.

will be examined.

Amplification Factor variation with Source Position

For a typical density say, 90 $M_{\odot}/\mathrm{pc}^2$ around Type 1 macroimage, Fig. 6.9 and 6.10 show the amplitude and the phase shift for the amplification factor $F(f)$ for different source positions for a particular mass distribution drawn from Chabrier IMF. The discussion will remain universal for all the mass distributions in consideration (refer 8.3).

From the Fig. 6.9 and 6.10, it can be clearly seen that both the phase and amplitude show strong deviation as the macro-amplification value is increased (or the source is moved closer to the lens center). The modulations also start from the lower frequencies.
As the macro-magnification value μ increases, the type 1 image gradually approaches the critical curve of the lens, as observed in Fig. 6.11. This phenomenon has been extensively studied in (12) and it has been established that this leads to a compression of the fixed area in the image plane by a factor of μ, resulting in the formation of overlapping microcaustics in the source plane. This overlapping effect becomes increasingly significant as one approaches the critical curves of the macromodel (12). The presence of small overlapping caustics can mimic the effect of a much larger microlens in terms of time delays (12). In other words, as per (12), a microlens of mass m embedded in a

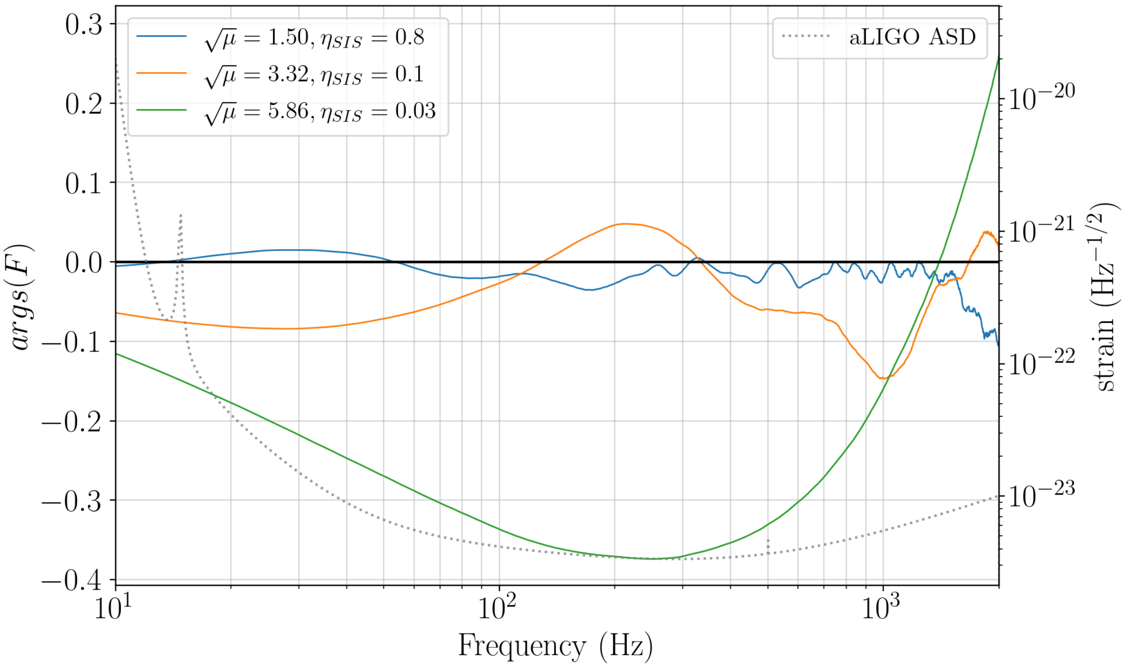

Figure 6.10: The figure shows the phase of the amplification factor $args|F|$ varying with frequency for different source positions $[\eta_{SIS} = [0.03, 0.1, 0.8]\theta_{SIS}]$ and hence macro-magnifications [$\mu = 34.33$, 10.99, 2.25] for a particular density 90 $M_\odot/\mathrm{pc}^2$. The solid black line corresponds to the phase shift 0 associated to the Type 1 macroimage. The ASD for aLIGO is plotted in grey along with the corresponding value of strain. The modulations in phase of the amplification factor are significant for higher values of macro-amplification.

macromodel with magnification μ behaves like a microlens with an effective mass of $m\mu$, thereby producing images with large relative time delays 3.5. This implies that microlensing can start dominating from lower frequencies and generate larger microlensing effects. [7]

Effective Micro-amplification and Mismatch v/s Source Position

From the figures 6.12 and 6.13 it can be seen that the effective micro-amplification increases strongly as the macro-amplification increases. This trend is expected as the amplitude of amplification factor shows strong modulations with increase in the macro-amplification, fig 6.9. Fig. 6.13 shows that overall increase is ~ 0.41 as the value of macro-amplification increases from 1.50 to 5.86. As the value of the effective micro-amplification is always greater than 1 it indicates that there is a the net-amplification of the macrolensed waveform (from type 1 macroimage) due to microlensing as the macro-amplification is increased. The result for the micro-amplification is in qualitative agreement with the literature (23).

Fig. 6.14 6.15 show that the mismatch increase steeply as compared to effective micro-amplification. The box plot in Fig. 6.15 shows that there is approximately an increase of $\sim 0.45\%$ as the macro-amplification increases from 1.5 to 5.86. The mismatch variation is stronger as compared to micro-magnification which is again a consequence of the sensitivity of the calculation to both the amplification effects and phase shift effects caused by microlensing 5.8. The mismatch however is below the detection threshold of 3%.

---

[7] The computational time for the simulations corresponding to $\eta_{SIS} = 0.03\theta_{SIS}$ is 12+ hrs for a single $F(f)$ vs f plot

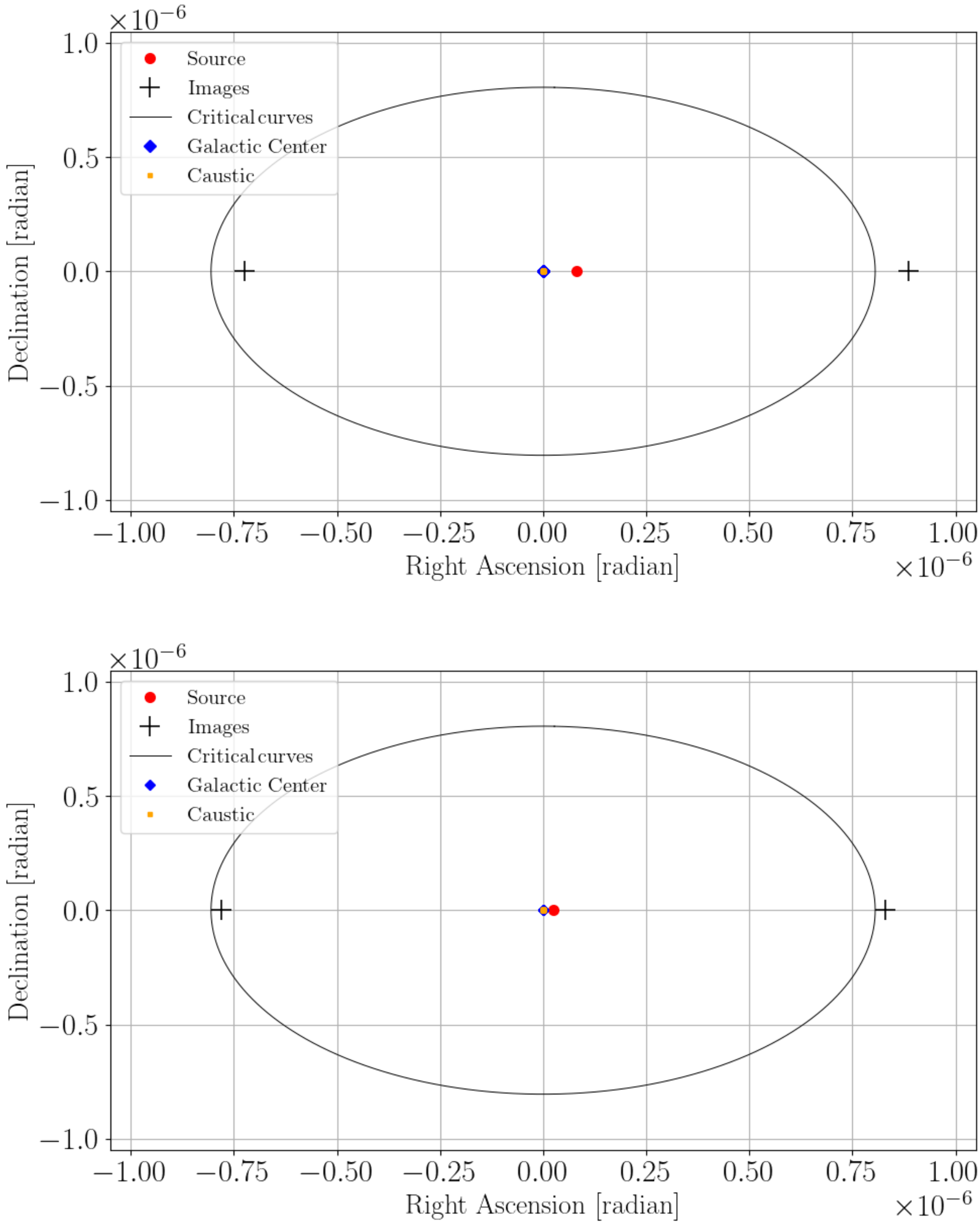

Figure 6.11: The basic description of the both the upper and lower panel is the same as the caption of figure 6.1. The source position is $\eta_{SIS} = 0.1\theta_{SIS}$ in the upper panel while the same is $\eta_{SIS} = 0.03\theta_{SIS}$ in the lower panel. It can be seen as the the source position is varied from $\eta_{SIS} = 0.1\theta_{SIS}$ to $\eta_{SIS} = 0.03\theta_{SIS}$ the type 1 macroimage (on right in both the plot panels) approaches the critical curve of the lens.

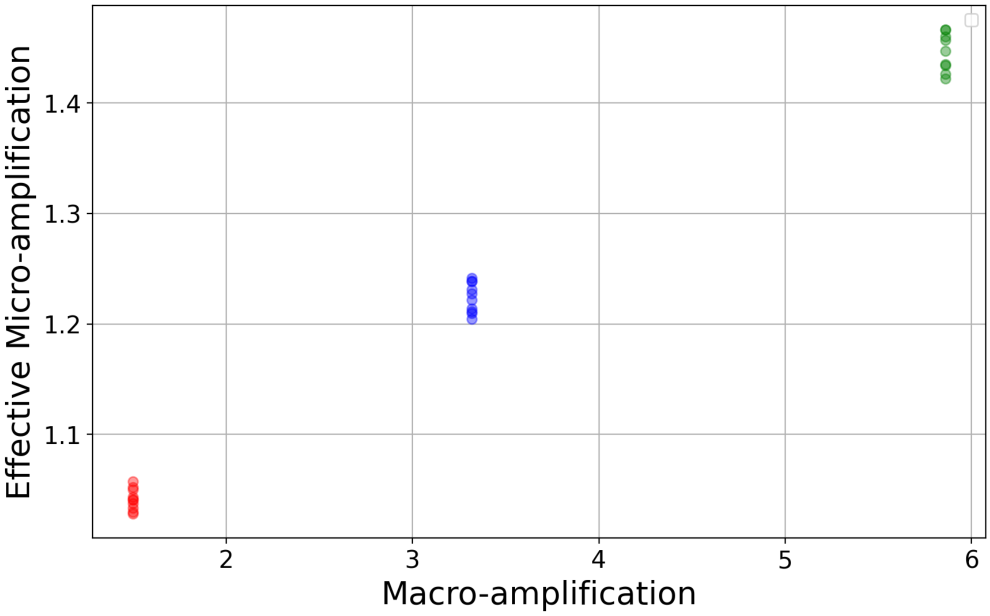

Figure 6.12: The figure shows the effective micro-amplification variation with the macro-amplification for 10 random mass distributions corresponding to each macro-amplification. Red, blue and green dots correspond to macro-amplifications $[\sqrt{\mu} = 1.50,\ 3.32,\ 5.86]$ and hence source positions $[\eta_{SIS} = [0.8, 0.1, 0.03]\theta_{SIS}]$. The effective micro-amplification increases with increase in macro-amplification for all the mass distributions.

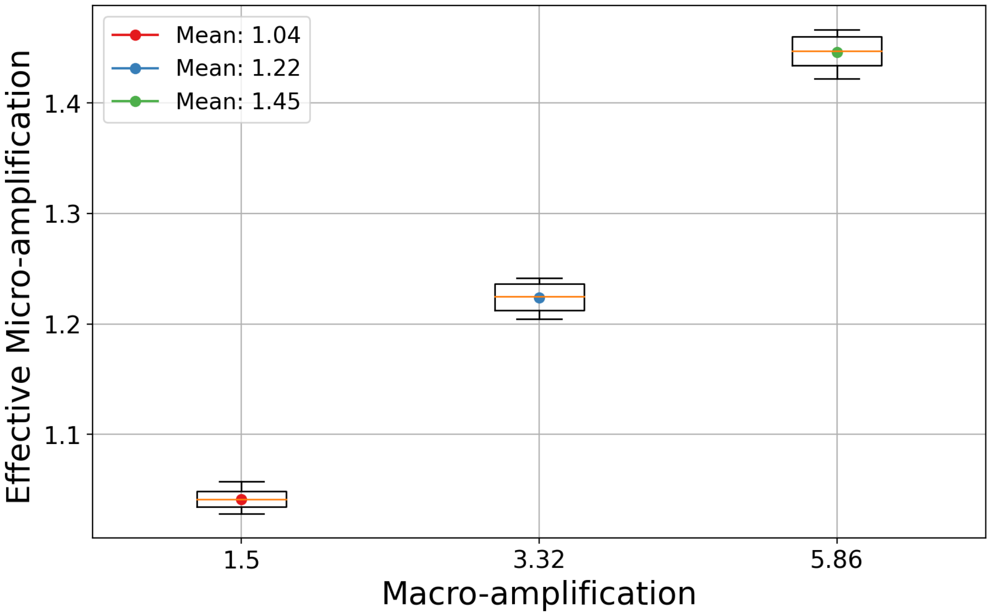

Figure 6.13: The figure shows the box plot corresponding to figure 6.12 for the variation of effective micro-amplification with macro-amplification with the corresponding mean values for the macro-amplification. The basic description of the box plot is the same as in the caption of fig. 6.5. The box plot also depicts increasing nature of effective micro-amplification with increase in macro-amplification.

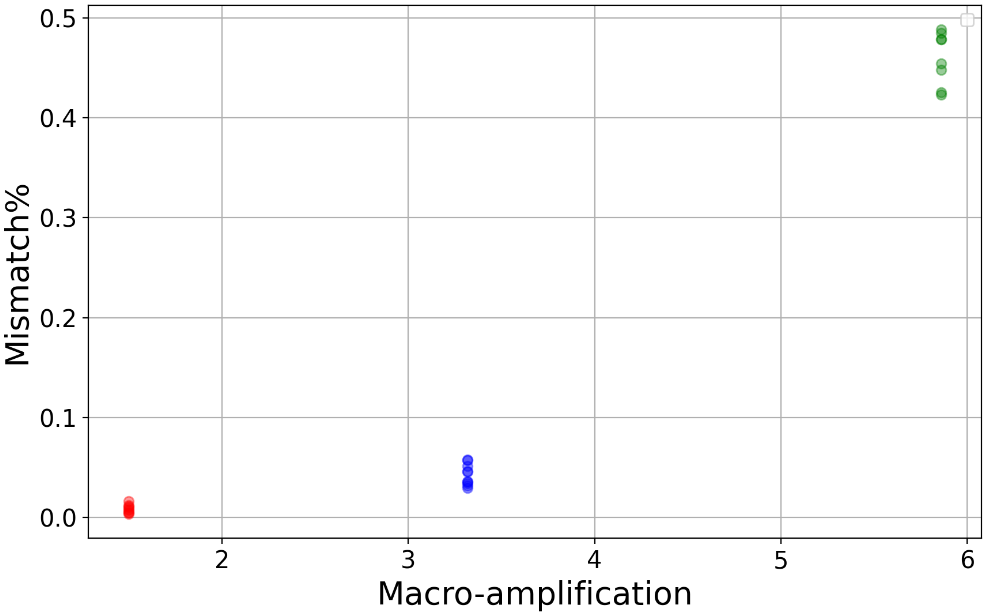

Figure 6.14: The figure shows the mismatch variation with the macro-amplification for 10 random mass distributions corresponding to each macro-amplification. Red, blue and green dots correspond to macro-amplifications $[\sqrt{\mu} = 1.50,\ 3.32,\ 5.86]$ and hence source positions $[\eta_{SIS} = [0.8, 0.1, 0.03]\theta_{SIS}]$. Mismatch increases with increase in macro-amplification for all the mass distributions.

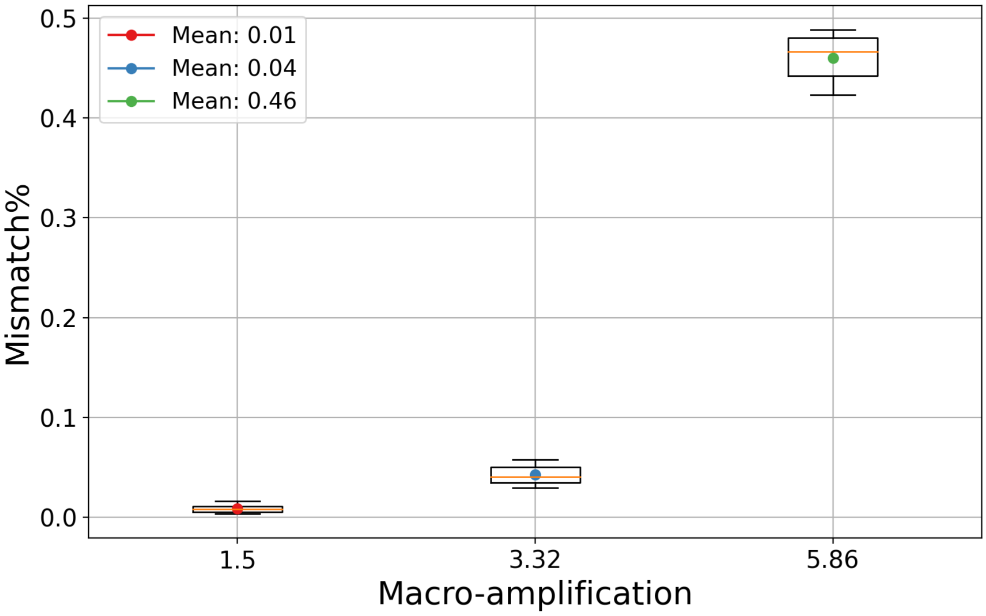

Figure 6.15: The figure shows the box plot corresponding to figure 6.14 for the variation of mismatch with macro-amplification with the corresponding mean values for the macro-amplification. The basic description of the box plot is the same as in the caption of fig. 6.5. The box plot also shows the increase in mismatch with increasing macro-amplification.

6.2.3 Effect due to Variation in Stellar IMF

Note: The literature presents a range of macro-amplification values corresponding to different densities around type 1 macroimage and thus for further investigation of the current scenario and all the upcoming parameters in interest, we set specific values for both macro-amplification (source position) and density for systematic investigation.
In particular, the literature highlights that a macro-amplification value near 3.32 corresponds to a density of approximately 90 $M_{\odot}/\mathrm{pc}^2$ for type 1 macroimages (23). Therefore, the particular values for the macro-amplification and density will be adopted for the further parameter investigation in the thesis[8].

Setup

The configuration of the lensing arrangement follows the methodology discussion in Section 5.2, accompanied by forthcoming explanation of the ensuing specifications for studying the variation with the IMF. For a fixed source position, specifically $\eta_{SIS} = [0.1]\theta_{SIS}$, the amplification factor $F(f)$ is calculated for density of 90 $M_{\odot}/\mathrm{pc}^2$ for Chabrier, Kroupa and Scalo IMF. For the analysis 10 random mass distributions are drawn from the each of the IMFs and for each distribution, we calculate the amplification factor $F(f)$. The mass of the binary producing the gravitational wave is considered to be 60+60 $M_{\odot}$ in the detector plane as taken in 6.2.1.

Different IMFs

Very similar to Chabrier IMF, the Kroupa IMF (67) has been found to be suitable for describing the early-type galaxies and low mass stars in previous studies (81), (64). The functional form of the Kroupa IMF is given as (70):

$$p_{kroupa} = \begin{cases} N_{1K} m^{-1.3}, & 0.08 < m < 0.5 M_{\odot} \\ N_{2K} m^{-2.3}, & 0.5 \leq m < 1 M_{\odot} \end{cases} \tag{6.1}$$

where N_{1K} and N_{2K} are the normalisation constants for Kroupa IMF.

Another IMF is Scalo IMF which is recognized as a more suitable representation of the mass distribution for massive stars with $m \geq 1M_{\odot}$ (82),(83). The functional form for the same is given as (83)

$$p_{scalo} = \begin{cases} N_{1S} m^{0}, & m < 1 M_{\odot} \\ N_{2S} m^{-2.7}, & m \geq 1 M_{\odot} \end{cases} \tag{6.2}$$

where N_{1S} and N_{2K} are the normalisation constants for Scalo IMF.

The corresponding masses from each IMF have been generated following similar procedure in section 5.2 for Chabrier IMF. Fig. 6.16 shows the line plot for the probability density function for Chabrier, Kroupa and Scalo IMF.

---

[8] The literature lists different values of macro-amplification corresponding to different densities, this pair of values has been chosen as the best match for observational probability and the corresponding computational time.

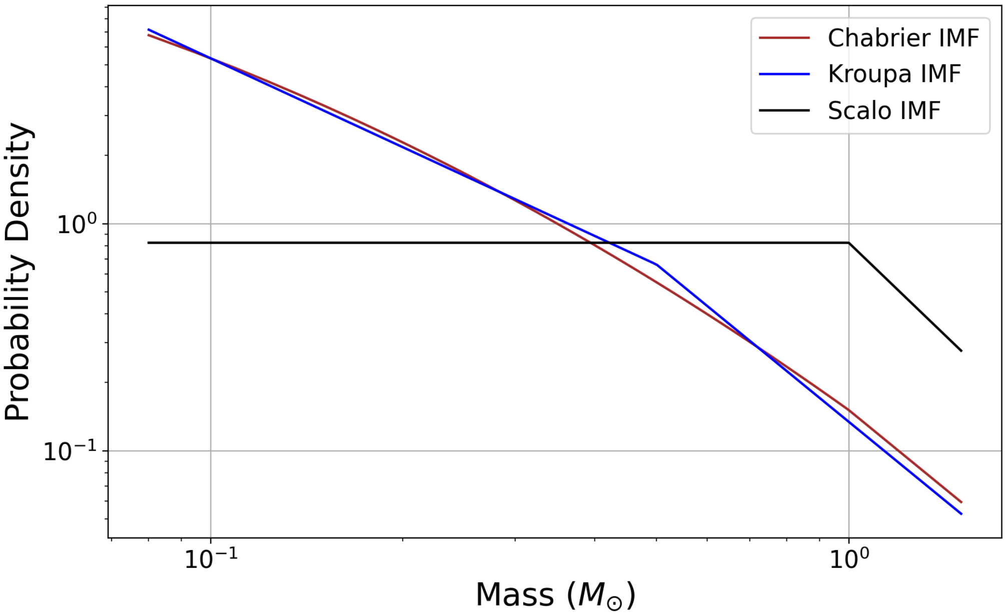

Figure 6.16: The figure shows the probability density plots corresponding to equations 5.2,6.1 and 6.2 for Chabrier, Kroupa and Scalo IMF respectively. Chabrier and Kroupa IMF have a higher probability density for lower mass lenses as compared to Scalo IMF. Chabrier and Kroupa IMF also show similar probability density form as plotted.

While the Chabrier and Kroupa IMFs are found suitable for modelling low mass stars, they also exhibit similar line plots as shown in Fig. 6.16 (indicating nearly equal probabilities of finding mass within a given mass range). Therefore, to explore the effects of significant deviations in the functional forms of the IMF, the Scalo IMF (82) is employed alongside the Chabrier and Kroupa IMFs for analysis purpose in this section.

Output from LensingGW: Lensing due to Macromodel

The parameters of the macromodel are the same as discussed in section 6.2.1. Thus, using software LensingGW, the same macro-magnification, image positions are obtained for the macromodel lensing setup which will be used in the calculation of the amplification factor and the study of mismatch and effective micro-amplification.

Variation with IMF

First, the impact of variation of IMF on the amplification factor $F(f)$ for a specific density is discussed after which the effects on mismatch and and effective micro-amplification is considered.

Amplification Factor Variation with IMF

For a single mass distribution drawn from of each of the IMFs: Chabrier, Kroupa and

Scalo, Fig.6.17 and 6.18 show the amplitude and the phase corresponding to the amplification factor $F(f)$. The discussion will remain universal for all the mass distributions in consideration for all the IMFs (refer 8.4).

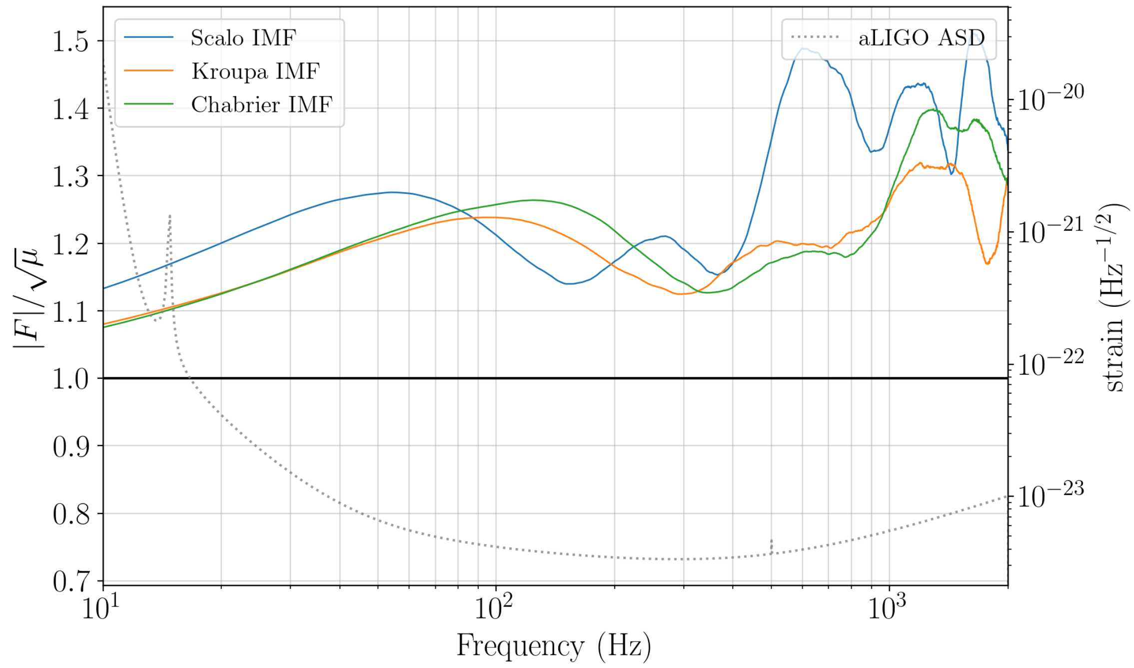

Figure 6.17: The figure shows amplitude of the amplification factor $|F|$ normalised by the strong amplification $\sqrt{\mu}$ varying with frequency for Chabrier, Kroupa and Scalo IMFs. The solid black line corresponds to the phase shift 0 associated to the Type 1 macroimage. The ASD for aLIGO is plotted in grey along with the corresponding value of strain.

From the Fig. 6.17 and 6.18, it can be seen that Scalo IMF has larger variations from lower frequency and there is a overall significant deviation in amplitude and phase at with frequency as compared to both Chabrier and Kroupa IMF.

This is because the Kroupa and Chabrier IMFs are more bottom heavy, i.e. probability density of drawing lower masses is higher as compared to the Scalo IMF, as depicted in Figure 6.16. This implies that, for the same density, the time delay of microimages tends to be relatively small for Chabrier/Kroupa as compared to Scalo IMF and thus, the distortions caused by microlensing occur at later stages in $F(f)$. An important thing to note is that although overall deviations are strong for Scalo IMF, the amplitude of the amplification factor can also decrease for certain frequency ranges in comparison to Kroupa and Chabrier IMF as seen in Fig. 6.17.

From 6.16 it is not ultimately clear if Chabrier or Kroupa is bottom heavy in comparison to each other. The differences in the phase and amplitude of the amplification factor is because of the sensitivity to the distribution of the microlenses and therefore mismatch and effective micro-amplification calculations will better illustrate the differences in the two IMFs, if any.

Effective Micro-Amplification and Mismatch v/s IMF

The top panel in Fig. 6.19 shows the effective micro-amplification variation for 10 random

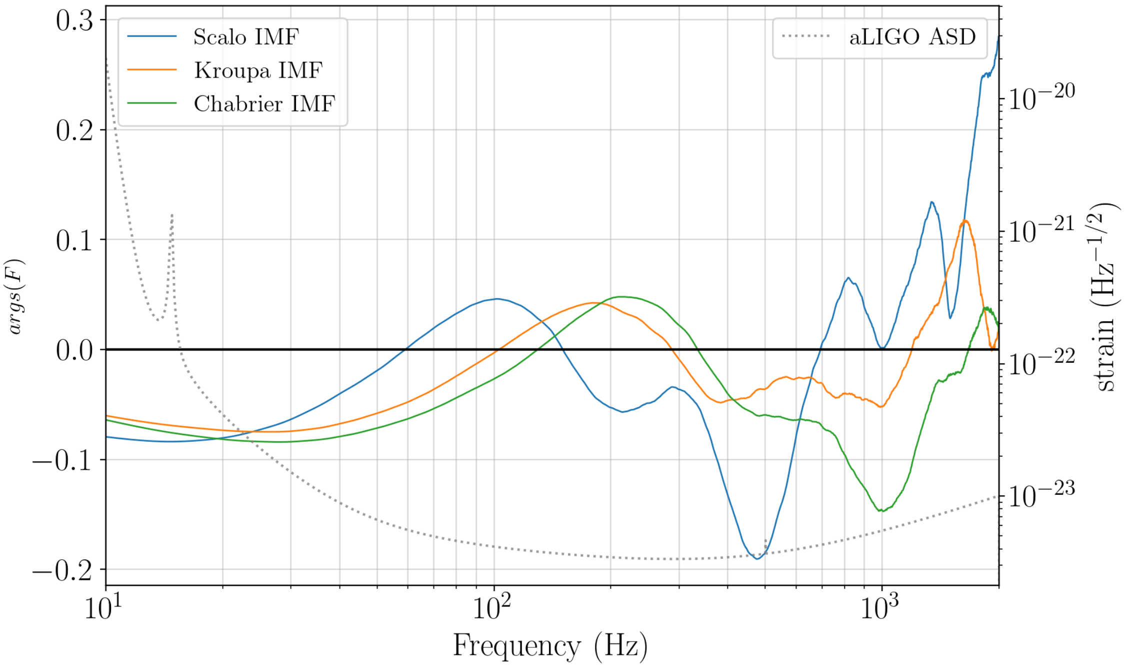

Figure 6.18: The figure shows the phase of the amplification factor $args|F|$ varying with frequency for Chabrier, Kroupa and Scalo IMFs. The solid black line corresponds to the phase shift 0 associated to the Type 1 macroimage. The ASD for aLIGO is plotted in grey along with the corresponding value of strain.

mass distributions drawn from all IMFs in consideration. For some of the distributions, Scalo IMF shows low effective micro-amplification as compared to Chabrier/Kroupa IMF. This can be expected as for some frequency ranges, the amplitude of amplification factor is less as compared to Chabrier/Kroupa IMF and this might dominantly affect the inner product calculation in equation 5.5 to produce lower output. The bottom panel in the same figure plots the corresponding mean values, which shows that the mean effective micro-amplification and the mismatch are almost indistinguishable for Chabrier, Kroupa, with the difference in Scalo IMF of approximately ~ 0.02. The effective micro-amplification is greater than 1 for all the IMFs.

Similarly, as per the top panel for Fig. 6.20, Scalo IMF is expected to produce higher mismatch as compared to Kroupa and Chabrier IMF. This increase can be attributed to the strong phase modulations as compared to Chabrier/Kroupa IMF. There is a difference of 0.08 % in the mean value of mismatch between Scalo and Chabrier/Kroupa IMF. This difference is well below the detection threshold of 3 %. This result is qualitatively consistent with the literature (23).
Due to the reasoning given in 5.2 and the result above, the Chabrier IMF will be utilized for the subsequent analysis as well.

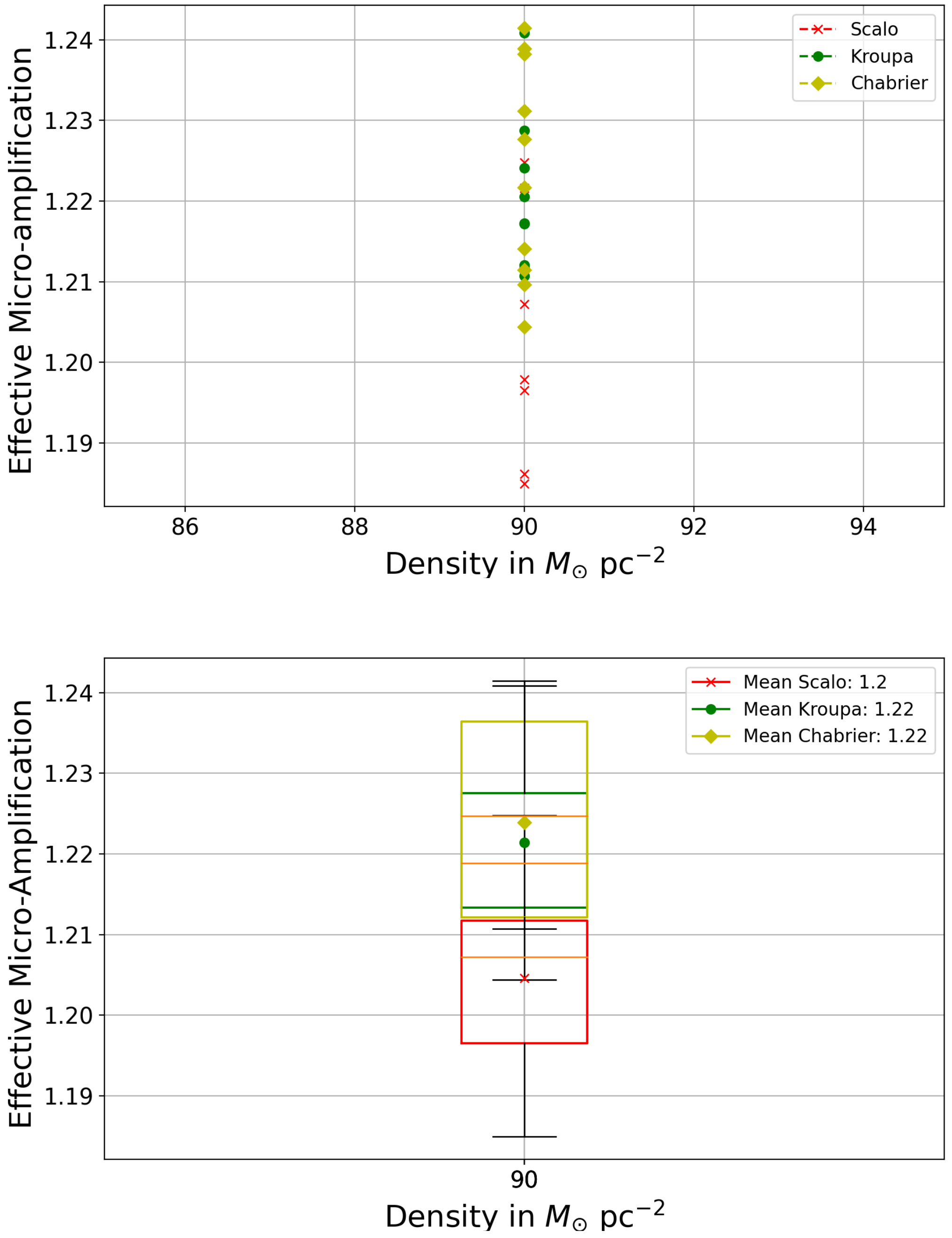

Figure 6.19: The upper panel shows the effective micro-amplification value for 10 random mass distributions for each IMF for the setup explained and the lower panel shows the box plot with the corresponding mean values for each IMF. The red, green and yellow boxes for the box plots correspond to Scalo, Kroupa and Chabrier IMF. The box plots exhibit substantial overlap when considering various IMFs. The basic description of the box plot is the same as in the caption of fig. 6.5.

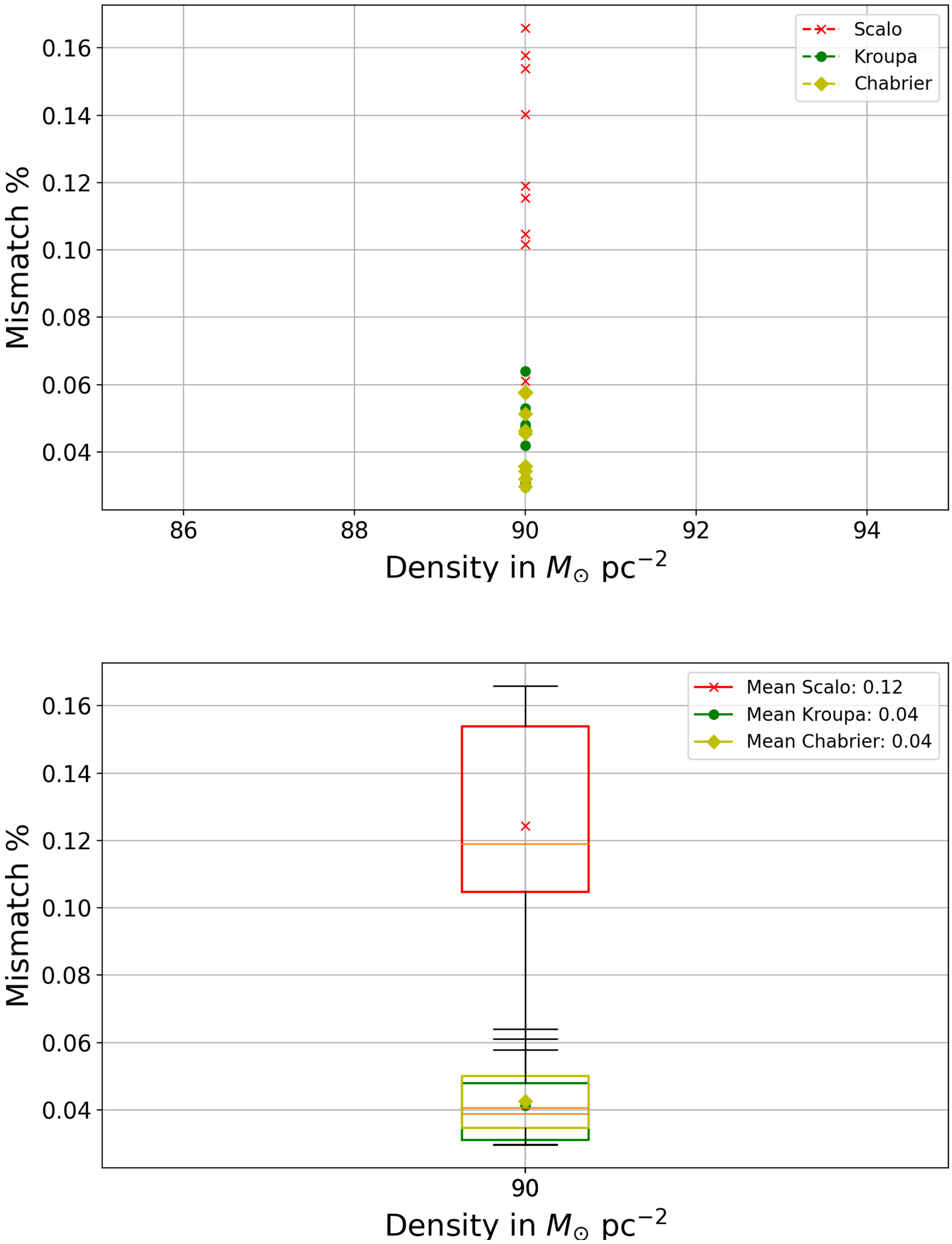

Figure 6.20: The upper panel shows the mismatch value for 10 random mass distributions for each IMF for the setup explained and the lower panel shows the box plot with the corresponding mean values for each IMF. The red, green and yellow boxes for the box plots correspond to Scalo, Kroupa and Chabrier IMF. The box plots exhibit a substantial overlap for Chabrier and Kroupa IMF. The basic description of the box plot is the same as in the caption of fig. 6.5.

6.2.4 Effect due to Variation in total mass of the Binary producing Gravitational waves

In this section, the focus will be on studying the effect of varying the total mass of the binary producing Gravitational waves. It is an important parameter to be investigated as the frequency evolution of the gravitational wave signal depends on the total mass of the binary as illustrated in equation 4.16 and 4.15. The total mass corresponds to the detector plane mass.

Setup

The configuration of the lensing arrangement follows the methodology discussion in Section 5.2, accompanied by forthcoming explanations of the ensuing specifications for studying the variation with the total mass of the binary producing gravitational waves. For the investigation, the total mass of the binary has been varied for the typical density 90 $M_{\odot}/\text{pc}^2$ and $\eta_{SIS} = [0.1]\theta_{SIS}$, as discussed in the preceding section. The study has been done for the 25 random mass distributions from the Chabrier IMF. The mass ratio has been fixed to 1 for simplicity in the analysis.

Output from LensingGW: Lensing due to Macromodel

The parameters of the macromodel are the same as discussed in section 6.2.1. Thus, using software LensingGW, the same macro-magnification, image positions are obtained for the macromodel lensing setup which will be used in the calculation of the amplification factor and the study of mismatch and effective micro-amplification.

Amplification Factor Variation

The amplification factor $F(f)$ is independent of the total mass of the binary producing the gravitational waves (4.29), thus the $F(f)$ as computed in section 6.2.1 for the density 90 $M_{\odot}/\text{pc}^2$ is used for the analysis. Fig. 6.22 shows the corresponding amplitude and phase variations of $F(f)$ for 25 random mass distributions.

Effective Micro-Amplification and Mismatch v/s Total Mass of the Binary

The discussion about the mismatch has been inspired from the literature (23) and (24).

As discussed earlier in Section 6.2.1, the graphs illustrating the variation of the amplification factor with frequency indicate that microlensing effects tend to increase as the frequency increases. With $f(t)$, f_{isco} and f_{rd} inversely dependent on the mass of the binary as discussed in section 4.3.1, the signals from the smaller mass binaries span higher frequencies. However, it is also important to note that smaller mass binaries have longer gravitational waveform as compared to the large mass binaries, corresponding to equation 4.19. Thus, the mismatch ultimately depends on the length of the signal and how it is affected by the modulations in $F(f)$.
Fig. 6.21 shows the mismatch variation with the total mass of the binary for 25 random mass distributions for the particular setup and also displays the mean plot for the same. It can be seen that the mismatch is larger for the binaries having lower total mass as

compared to those with higher mass. The mean increase is $\sim 0.15\%$ for the highest and the lowest values of mismatch. However, we do not observe a consistent increase in the mismatch initially as we lower the binary mass. This can be explained from the preceding discussion. Despite smaller mass binaries spanning higher frequencies, their longer waveforms can lead to a reduction in mismatch if distortions in $F(f)$ are not significant at low frequencies, leading to a larger part of the signal being unaffected by the microlensing.

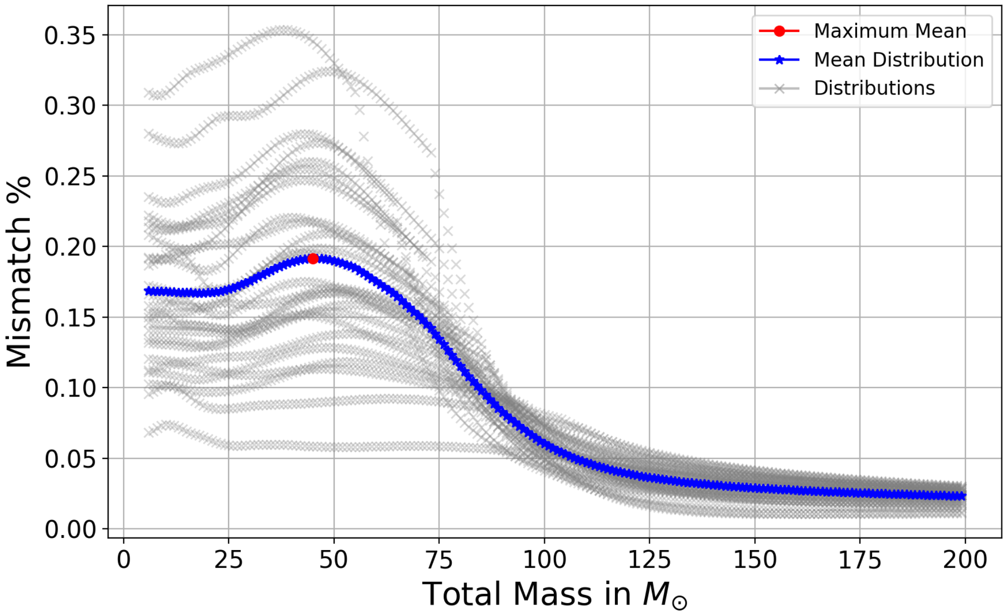

Figure 6.21: The figure shows the mismatch variation with the total mass of the binary producing gravitational waves. The grey plots show the mismatch calculated for 25 random mass distributions drawn from the Chabrier IMF for the particular setup. The blue plot displays the mean variation plot for the distributions with the red point marking the maximum mismatch for the corresponding total binary mass (45 $M_\odot$). The variability in the mean values is proportional to the scatter of the distributions.

On an average, the maximum mismatch is observed for the total mass around 45 $M_\odot$ and the minimum is for total mass ~ 200 $M_\odot$. The maximum mismatch for the mean distribution can be thus be explained by examining the gravitational waveform of a binary system corresponding to highest and lowest mismatch and comparing it with the amplitude and phase curves of the amplification factor $F(f)$.
From Fig. 6.22 it can be seen that the wave optics suppression ($|F|/\sqrt{\mu} \sim 1$) occurs at the low frequencies and the microlensing effects start dominating from the higher frequencies, as explained in section 6.2.1. Figure 6.23 depicts the gravitational waveform for two binary systems: with total mass 45 $M_\odot$ and 200 $M_\odot$ respectively. Notably, the gravitational waveform for the more massive binary is shorter compared to that of the less massive binary. In contrast, the less massive binaries exhibit a frequency range that covers a region with relatively stronger microlensing effects and thus, there is a higher mismatch for the lesser total binary mass.

Expressed mathematically, the calculation of the mismatch entails the assessment of the inner product, outlined by equation 5.8. Extended the signal's duration in within the frequency domain leads to more evidence of deviations from an unlensed waveform, resulting in greater mismatch. Moreover, as microlensing-induced modulations increase with increasing frequencies, the inclusion of signals spanning higher frequency ranges can correspond to increase in mismatch. These results for the mismatch shows qualitative agreement with the literature (23).
The mismatch however always remains below the detection threshold of 3%. However, for the high mass microlenses (0.08 $M_{\odot}$ to 28 $M_{\odot}$) and high macro-amplification ($\sqrt{\mu} \sim 10$) literature reports the mismatch to reach the detection threshold. It is expected as the large mass microlenses produce a large time delay (as discussed in section 6.2.1).

Fig. 6.24 shows the effective micro-amplification variation with the total mass of the binary for 25 random mass distributions for the particular setup and also displays the mean plot for the same. The effective micro-amplification value is always above one which means that there is always net-amplification of the waveform as the total binary mass is varied. The mean increase is ~ 0.02 for the corresponding highest and the lowest mean values of effective micro-amplification. However, interestingly for the particular case, the maximum of the effective micro-amplification, occurs at relatively high mass as compared to the mismatch. This is again because the micro-amplification captures the net amplitude increase due to microlensing and the mismatch relates to the changes in both the amplitude and the phase as per the formulae discussed in section 5.3. Thus, net amplitude amplification can still be expected for the higher mass binaries, where the mismatch comparatively the lowest.

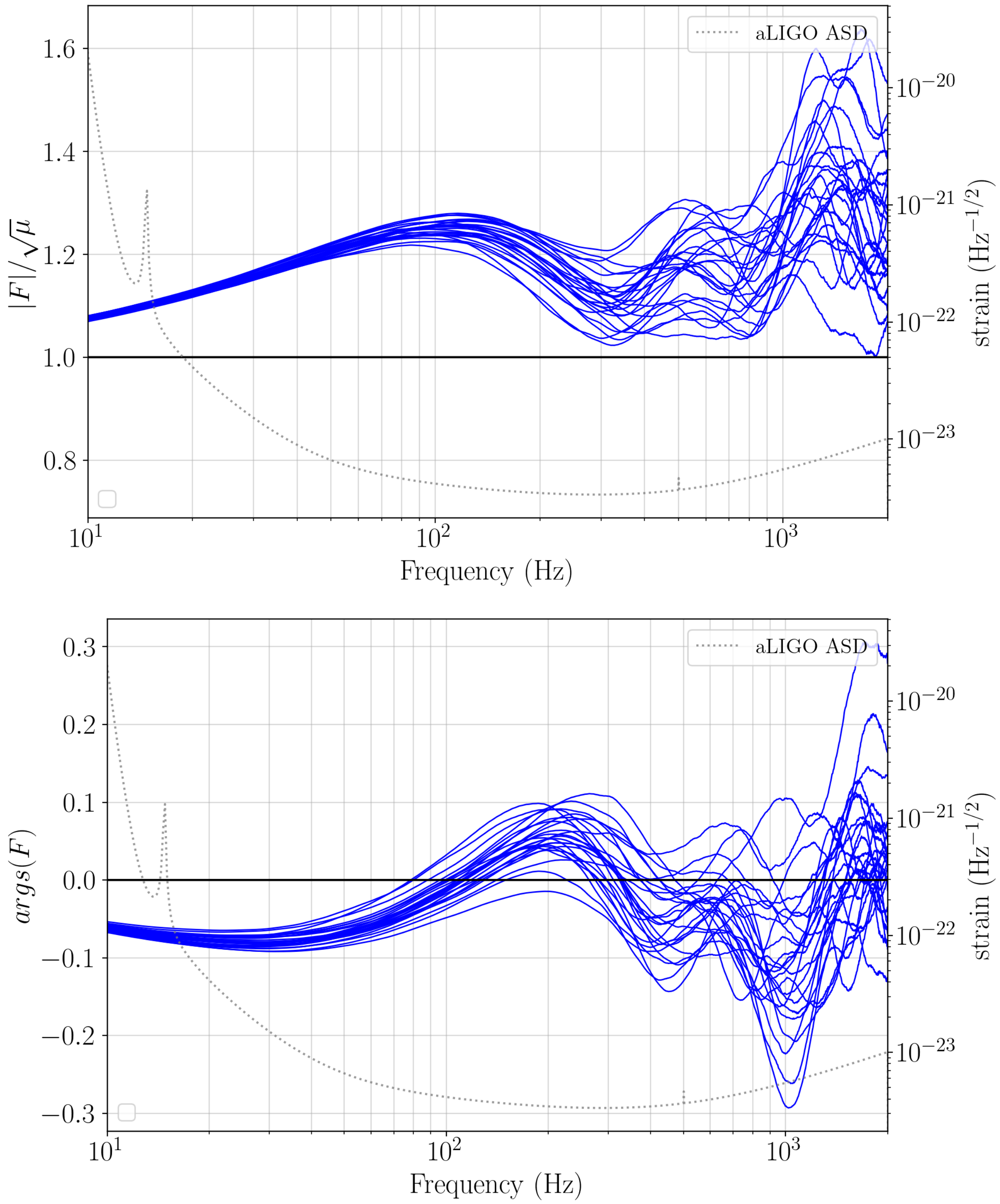

Figure 6.22: The top panel shows the amplification factor $|F|$ normalised by the strong amplification $\sqrt{\mu}$ and bottom panel shows the phase $args|F|$ of the amplification factor varying with frequency for 25 random mass distributions drawn from the Chabrier IMF for the particular setup. The solid black line corresponds to the $|F|$ being equal to the strong lensing amplification value $\sqrt{\mu}$ in the top panel and the phase shift 0 in the bottom panel. The ASD for aLIGO is plotted in grey along with the corresponding value of strain. The stronger distortions due to microlensing effects in both the amplitude and phase occur at higher frequencies as elucidated in section 6.2.1.

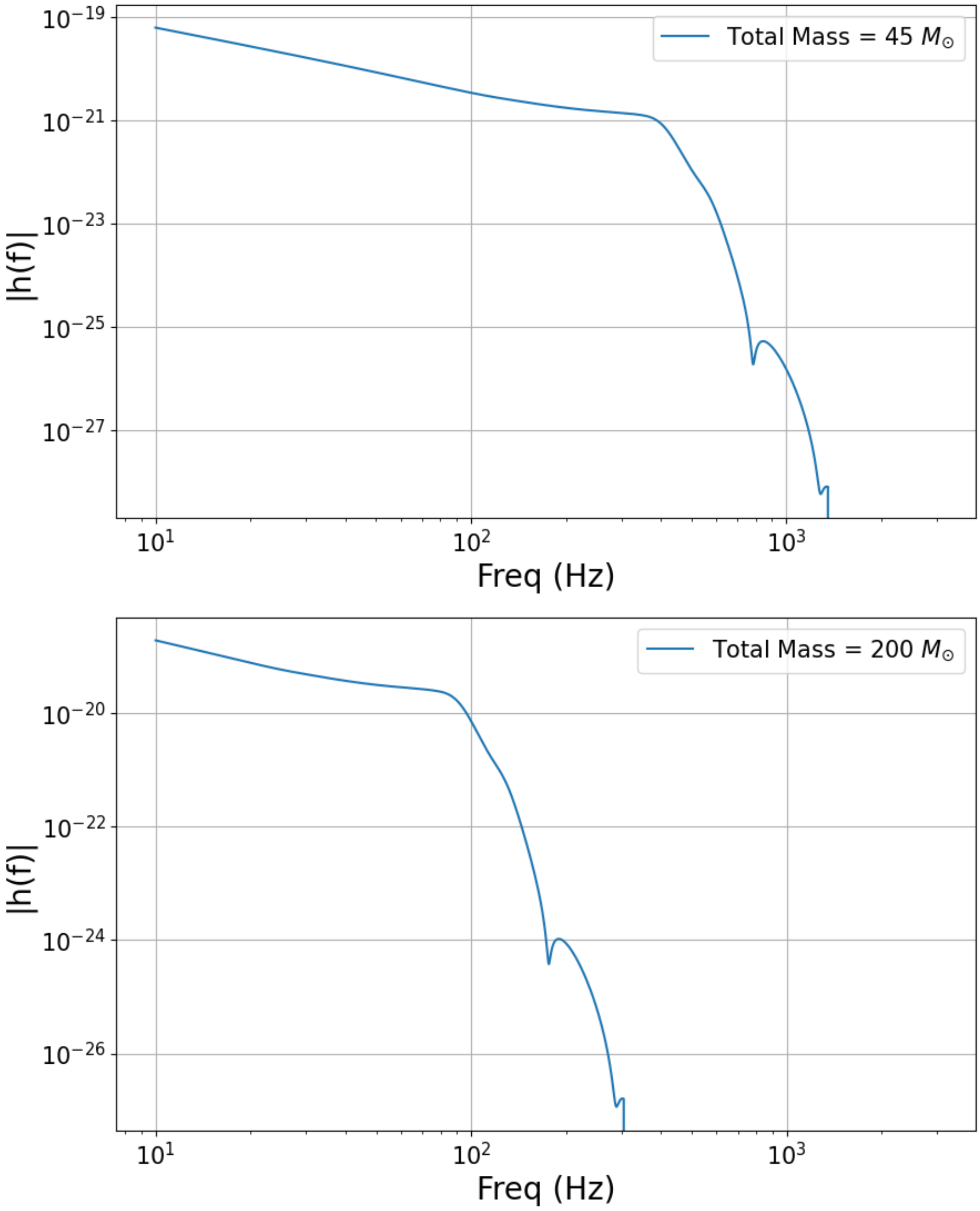

Figure 6.23: The absolute value of the Fourier transform of the gravitational wave strain amplitude $|h(f)|$ plotted as a function of frequency in both the panels of the figure. the gravitational wave form generated using IMRPhenomXPHM waveform model as explained in section 5.3. Compared to the waveform for the binary with a total mass of 45 $M_\odot$, the waveform for the binary with a total mass of 200 $M_\odot$ is shorter in terms of frequency span.

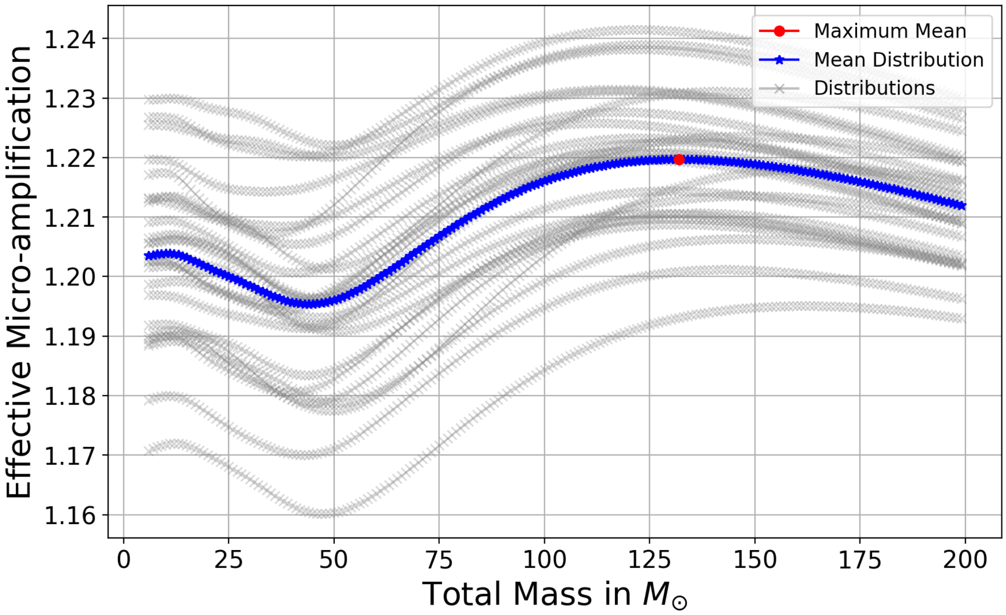

Figure 6.24: The figure shows the effective micro-amplification variation with the total mass of the binary producing gravitational waves. The grey plots show the same calculated for the 25 random mass distributions drawn from the Chabrier IMF for the particular setup. The blue plot displays the mean variation plot for the distributions with the red point marking the maximum effective micro-amplification (at $132M_\odot$) for the corresponding total binary mass. The variability in the mean values is proportional to the scatter of the distributions.

6.2.5 Effect due to Variation in the Mass Ratio

In this section, the focus is on studying the impact of varying the mass ratio of the binary system on the production of gravitational waves. As mentioned earlier, the frequency evolution of the gravitational wave signal is influenced by the mass ratio of the binary system as illustrated in equation 4.16 and 4.15.

Setup

The configuration of the lensing arrangement follows the methodology discussion in Section 5.2, accompanied by forthcoming explanations of the ensuing specifications for studying the variation with the mass ratio of the binary producing gravitational waves. For the investigation, the mass ratio of the binary has been varied, $q = m_2/m_1 \in (0, 1]$, for the typical density 90 $M_\odot/\text{pc}^2$ and $\eta_{SIS} = [0.1]\theta_{SIS}$, as discussed in the preceding section. The study has been done for the 25 random mass distributions from the Chabrier IMF for the density 90 $M_\odot/\text{pc}^2$. The mass of the binary producing the gravitational wave is considered to be 60+60 $M_\odot$ in the detector plane as taken in 6.2.1.

The discussion for the output from LensingGW and the amplification factor remain the same as discussed in the preceding section (6.2.4)

Effective Micro-Amplification and Mismatch v/s the Mass ratio of the Binary

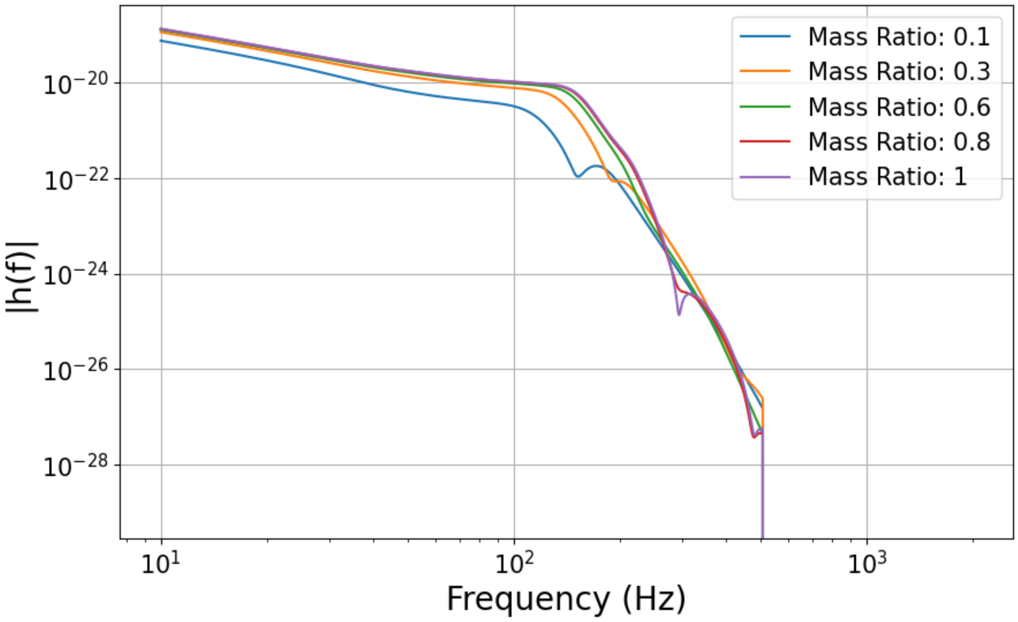

Figure 6.25: The absolute value of the Fourier transform of the gravitational wave strain amplitude $|h(f)|$ plotted as a function of frequency for a 60+60 $M_\odot$ binary with the masses reported in detector plane. The gravitational wave form generated using IMRPhenomXPHM waveform model as explained in section 5.3. The length of the waveform before the ringdown frequency, marked by the sudden decline in waveform similar to fig. 4.3, increases as the mass ratio increases.

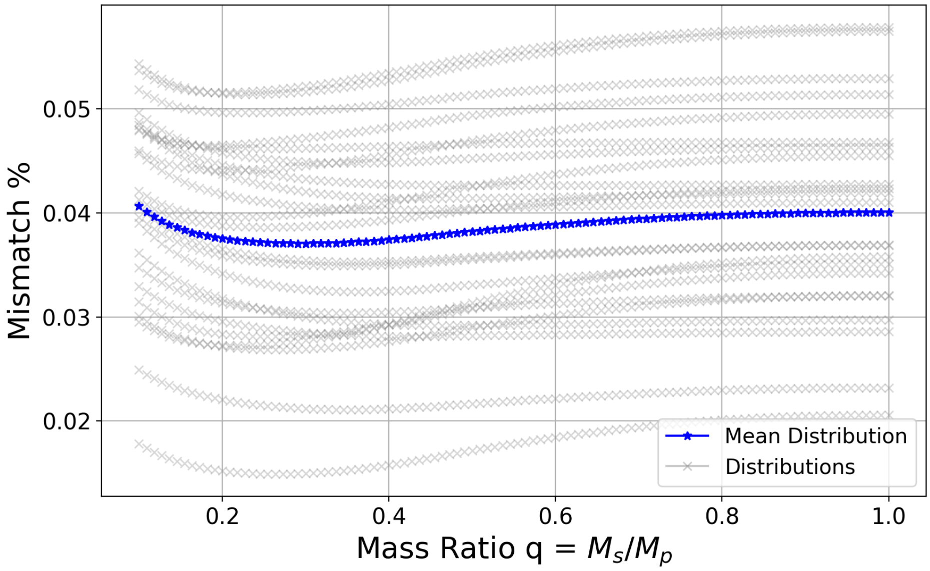

Figure 6.26: The figure shows the mismatch variation with the mass ratio for total binary mass 120 $M_\odot$. The grey plots show the mismatch calculated for the 25 random mass distributions drawn from the Chabrier IMF for the particular setup. The blue plot displays the mean variation plot for the distributions. The variability in the mean values is proportional to the scatter of the distributions.

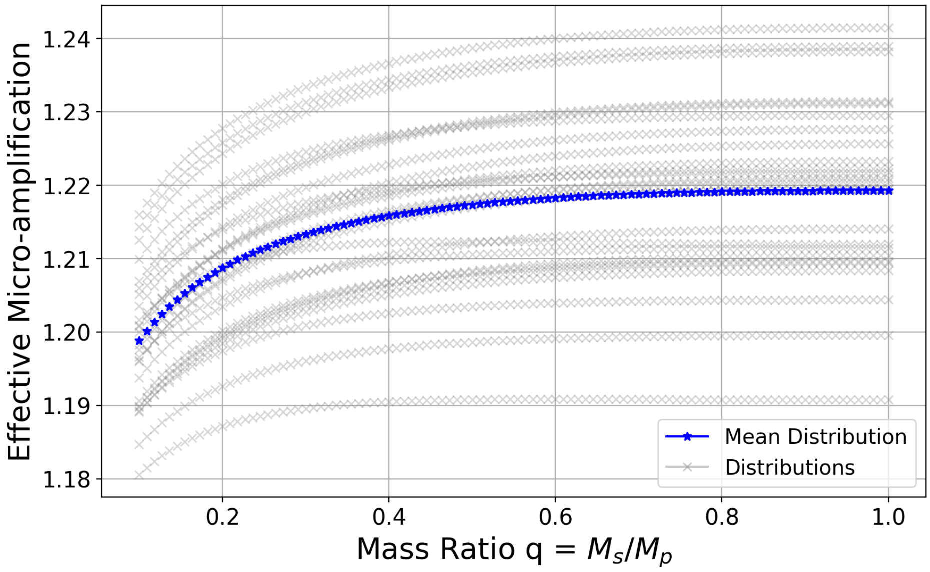

Figure 6.27: The figure shows the effective micro-amplification variation with the mass ratio for total binary mass 120 $M_\odot$. The grey plots show the effective micro-amplification calculated for the 25 random mass distributions drawn from the Chabrier IMF for the particular setup. The blue plot displays the mean variation plot for the distributions. The variability in the mean values is proportional to the scatter of the distributions.

Figure (6.25) shows the variation in the gravitational waveform as the mass ratio of the binary increases for the binary mass chosen for the analysis. The length of the signal before ringdown increases as the mass ratio increases. As the amplitude of the gravitational waveform decreases very sharply after the ringdown, the ringdown phase does not contribute much to the mismatch (23). Therefore, similar to the discussion in section 6.2.4 signal length increasing before the ringdown can lead to higher mismatch however the increase is not expected to be coherent because of the competition between the signal length and the modulations in $F(f)$.
Fig. 6.26 shows the the mismatch variation with the mass ratio of the binary for 25 random mass distributions are drawn from the Chabrier IMF for the particular setup and also displays the mean plot for the same. Except for very low mass ratio (~ 0.1), the mismatch increases with increase in mass ratio, however the mean increase is of the order of 0.001%, corresponding to the minimum mean value mismatch and value at $q = 1$. [9]. The mismatch however always remains well below the detection threshold of 3%. These results for the mismatch show qualitative agreement with the literature (23). However, for the high mass microlenses (0.08 $M_{\odot}$ to 28 $M_{\odot}$) and high macro-amplification ($\sqrt{\mu} \sim 10$) literature (23) reports the mismatch to reach the detection threshold which is expected as the higher mass microlenses produce larger time delay (as discussed in section 6.2.1).

Fig. 6.27 shows the effective micro-amplification variation with the mass ratio for 25 random mass distributions for the particular setup and also displays the mean plot for the same. The effective micro-amplification shows an increase with the mass ratio, indicating increasing amplification due to microlensing. As the effective micro-amplification value is always greater than 1 it means that the macrolensed waveform (from type 1 macroimage) is effectively amplified due to microlensing for the variable mass ratio. The mean increase is ~ 0.2 for the highest and the lowest values of effective micro-amplification. However, the relationship between the mismatch and effective micro-amplification is not identical as effective micro-amplification measures the net waveform amplification due to microlensing and the mismatch is an overall measure of microlensing effects as also illustrated in the sections above. [10]

---

[9] the discussion above suggests that for very low mass ratio, (~ 0.1) there is a greater length of signal being affected by microlensing despite overall shorter waveform as compared to other q values

[10] The same $F(f)$ plots were used for the investigation in Fig. 6.27 and fig.6.24. In terms of the signal length, the effective micro-amplification clearly increases with increase in signal length with Fig. 6.27 while similar is not the case in fig.6.24. This demonstrates the sensitivity of the effective micro-amplification calculation to the binary waveform used for the computation for particular $F(f)$.

6.3 General Discussion of Results

As the effective micro-amplification value is always greater than one, the lensing by a population of microlenses always leads to net amplification of the macrolensed waveform (from type 1 macroimage) for all the parameters considered. Thus, microlensing effects are expected to introduce differences in the luminosity distance in the strong lensing studies (19) and the error propagation in the measurements is proportional to effective micro-amplification value. As the mismatch is less than the threshold of 3 % for all the cases in consideration, microlensing by the population of lenses will not affect the measurement of intrinsic source parameters.

Amongst all the parameters, the microlensing effects are the most sensitive to the variation of the source position (macro-amplification value). As mismatch is a directly inferable quantity from observations, its known values within the detectable limit may facilitate the constraint on macro-amplification, both due to the strong variations in mismatch and absence of overlap in the dispersion regions depicted by the box plots in fig. 6.15 (however the extent of the same requires additional research).

Overall, large microlensing effects be expected for the high density of microlenses, high macro-amplification, low mass binaries and equal mass ratio of the binary - taking relevant IMF (Chabrier or Kroupa in this study) for the given mass range of microlenses. An example demonstrating this can be presented as follows:
As discussed in section 6.2.4 we study the effective micro-amplification and mismatch variation with the total mass of binary ($q = 1$). In this analysis, the only difference with the setup in section 6.2.4 is that the macro-amplification is now set to 5.86 (or the source position is $\eta_{SIS} = 0.03$ as presented (6.2.2) and the density of 107 $M_{\odot}/\mathrm{pc}^2$ is considered. While the particular density and macro-amplification values adopted may not be commonly reported in the literature for Type 1 macroimages, this case suitably illustrates the phenomenon under investigation.
Fig. 6.28 shows the effective micro-amplification and mismatch variation with the total binary mass for the particular setup. Following the discussion in section 6.2.4, it can be seen that the mismatch reaches the detection threshold of 3% close to total mass 18 $M_{\odot}$ while the effective micro-amplification values are comparatively larger than those studied previously, reaching a maximum at total mass of 32 $M_{\odot}$. As per the results, the significant impact to the increase in the mismatch and micro-amplification is attributed to the increased macro-amplification. The maximum mismatch value corresponds to the total mass of the binary in the source plane to be 9 $M_{\odot}$. Even if there is a non-zero probability for the case corresponding to $\mu \sim 34$ and density = 107 $M_{\odot}/\mathrm{pc}^2$, the total mass for which the mismatch reaches the detection threshold corresponds to 4+4 $M_{\odot}$ binary in the source plane which is very less probable to be observationally detectable as this is well below the observed peak for the binary component masses in the source plane close to 30 $M_{\odot}$.

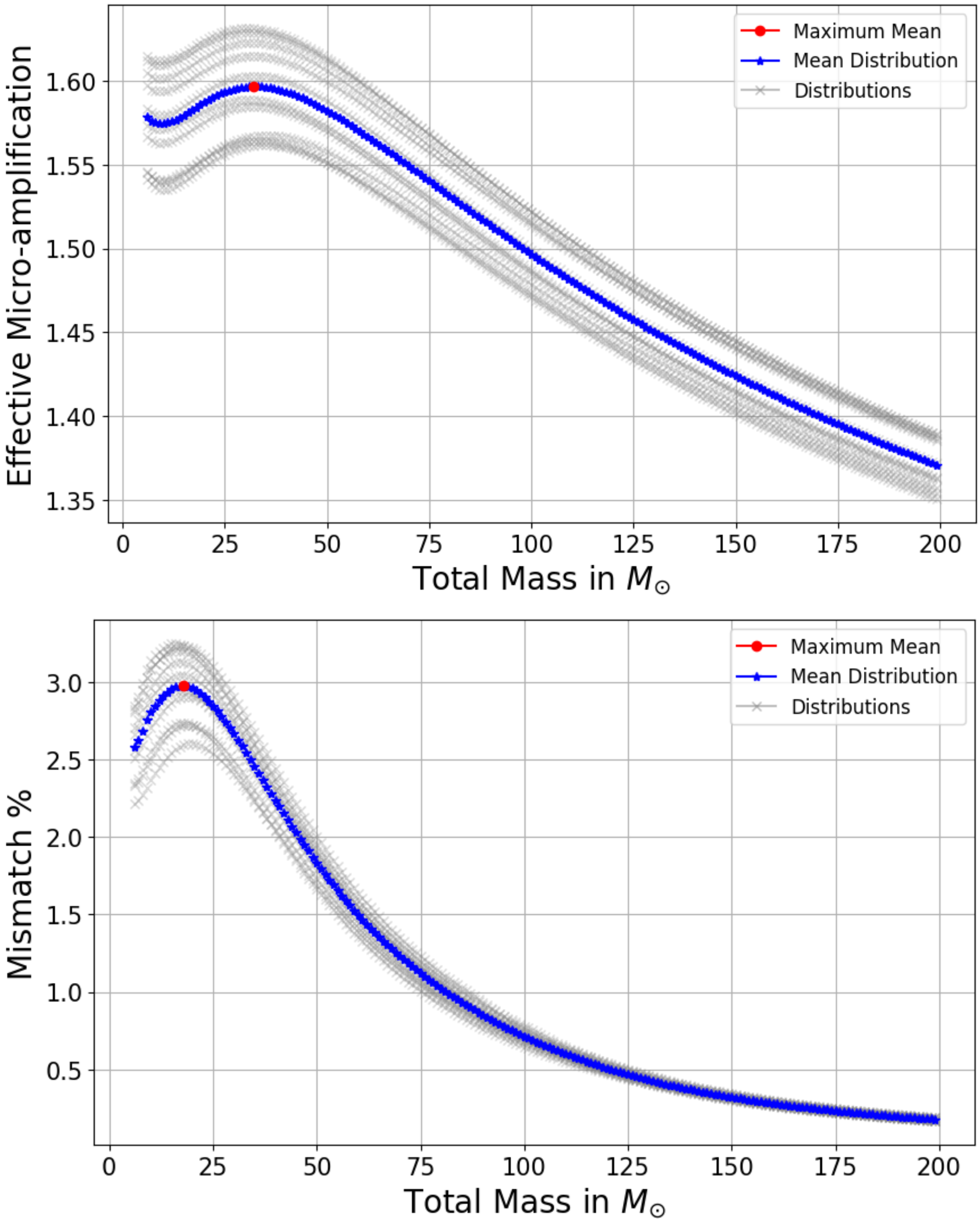

Figure 6.28: The upper panel shows the effective micro-amplification a with the total binary mass and the lower panel shows the corresponding mismatch for the particular setup. In both the panels, the grey plots show the same calculated for the 10 random mass distributions drawn from the Chabrier IMF for the particular setup. The blue plot is the mean variation plot for the distributions, with the red point marking the maximum effective micro-amplification and mismtach respectively for the corresponding total binary mass. The variability in the mean values is proportional to the scatter of the distributions. The mismatch reaches the detection threshold of 3% while the effective micro-amplification values are comparatively larger than those studied previously during the parameter investigation.

Chapter 7

Conclusion and Future Work

7.1 Conclusion

With this thesis, the impact of microlensing by a population of microlenses on the signal from type 1 macroimage has been analysed. After grasping the relevant theoretical understanding, the first step was developing a code for the lensing by multiple microlenses building upon the existing code for lensing by a single microlens. Following this, the study of the variation of amplification factor and the quantification of mismatch and effective micro-amplification for all the relevant parameters in consideration is performed. Relevant comparison with the existing literature has also been made when possible and it has been found that the results are in qualitative agreement with the literature.

The study concluded that microlensing will not affect intrinsic source parameter estimation and can still effect the luminosity distance measurement in the strong lensing studies for the taken setup. Overall, larger microlensing effects can be expected for the high density of microlenses, large image magnification due to strong lensing (high macro-amplification), low mass binaries and mass ratio being unity - taking relevant IMF (Chabrier/Kroupa in this study) for the given mass range of microlenses. Amongst all the parameters investigated, the highest contribution to the microlensing effects is expected from the increase in the macro-amplification value or decrease in the macro-impact parameter of the source.

In addition to the code development and independent investigation, this work is an important contribution to the existing literature with the comprehensive and systematic analysis of both the mismatch and effective micro-amplification for a population of microlenses. The mismatch quantification emphasises that if a type 1 macroimage is detected for low macro-amplification ($\sqrt{\mu} \leq 3$), it can be used as a reference GW signal for intrinsic parameter estimation. While the effective micro-amplification will have its corresponding error budget in the strong lensing studies such as (19), the significance of the error contribution is dependent on the significance of the other error measurements. Furthermore, effective micro-amplification quantification also shows that microlensing by a population of microlenses always results in the net amplification of the original macrolensed waveform for all the parameters considered.

It is important to note that the conclusions related to the detection probability of microlensing effects are valid in the limit of the setup in consideration, however the physics of nature of the variation of the amplification factor $F(f)$, mismatch and effective micro-amplification can be applied to the different setup in consideration.

7.2 Future Work

The first direction of the work should be the code optimization for the message passing interface as it will significantly decrease the computational time for the simulations. Following this, it will be interesting to investigate the simulations leading to large microlensing effects and studying the corresponding observational probability for such events. Within the detectable limits, mismatch can help in constraining the corresponding parameter space values, nonetheless, a comprehensive understanding of its extent will necessitate additional research.

Furthermore, there lies an exciting opportunity to conduct a more comprehensive exploration of all the parameters that have been fixed in the setup. A particularly fascinating avenue lies in studying the impact of redshift on both the source and lens plane as it affects the time delay (as per equation 3.26) and the chirp mass of the binary (as per equation 4.18). Additionally, the investigation could extend to understanding how the increased sensitivity of detectors influences the outcomes. Existing studies suggest an increased likelihood of detecting microlensed induced signals with advanced detectors like the Cosmic Explorer and the Einstein Telescope, as highlighted by (12).

The application of effective micro-amplification analysis in this work can be instrumental in refining error estimations for luminosity distance in the context of strong lensing studies such as (19). The conclusions from the analysis related to mismatch can be utilized in the GW paramter estimation studies from the lensed signal.
Although we focused on the microlensing effects on type 1 macroimage, the insights from this thesis and the code developed have the potential for broader applications including the analysis of lensed signal from type 2 and type 3 macroimages.

Lastly, in the midst of these academic pursuits, it is also essential to pause and reflect on the grandeur of the universe itself—a captivating mosaic of beauty and wonder that continues to inspire our quest for knowledge.

Chapter 8

Appendix

8.1 Contribution to Software Lenstronomy

During the course of investigating macromodel-based lensing phenomena, it was ascertained that the caustic count provided by the software LensingGW (11) exhibited inaccuracies. LensingGW works on a forked version of the Lenstronomy software (76), which is responsible for caustic count computation. The identified issue was subsequently communicated to the original author of Lenstronomy. I contributed to the resolution if this issue by reporting the bug on the GitHub platform. The author duly acknowledged my participation in rectifying the matter, as evidenced by the attached documentation 8.1

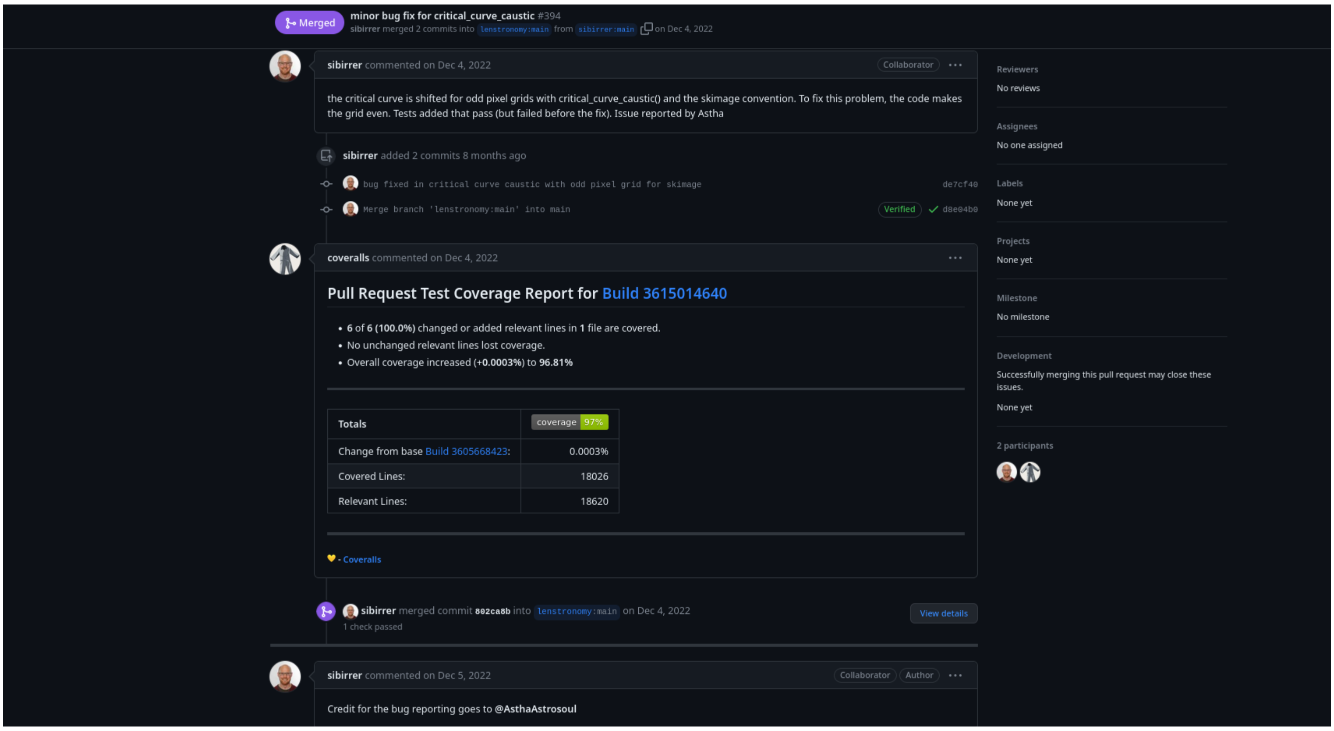

minor bug fix for critical_curve_caustic #394
sibirrer merged 2 commits into `lenstronomy:main` from `sibirrer:main` on Dec 4, 2022

sibirrer commented on Dec 4, 2022

the critical curve is shifted for odd pixel grids with critical_curve_caustic() and the skimage convention. To fix this problem, the code makes the grid even. Tests added that pass (but failed before the fix). Issue reported by Astha

sibirrer added 2 commits 8 months ago

```
bug fixed in critical curve caustic with odd pixel grid for skimage    de7cf40
Merge branch 'lenstronomy:main' into main                   Verified ✓ d8e04b0
```

coveralls commented on Dec 4, 2022

Pull Request Test Coverage Report for Build 3615014640

- **6** of **6 (100.0%)** changed or added relevant lines in **1** file are covered.
- No unchanged relevant lines lost coverage.
- Overall coverage increased (**+0.0003%**) to **96.81%**

Totals	coverage 97%
Change from base Build 3605668423:	0.0003%
Covered Lines:	18026
Relevant Lines:	18620

💛 - Coveralls

sibirrer merged commit **802ca8b** into `lenstronomy:main` on Dec 4, 2022
1 check passed

sibirrer commented on Dec 5, 2022

Credit for the bug reporting goes to **@AsthaAstrosoul**

Reviewers: No reviews
Assignees: No one assigned
Labels: None yet
Projects: None yet
Milestone: No milestone
Development: Successfully merging this pull request may close these issues. None yet
2 participants

Figure 8.1: Bug Report Credit Lenstronomy

8.2 Amplification Factor Graphs for the Variation with Density for different distributions

Following the setup description in section 6.2.1, graphs below (Fig. 8.25) show the amplitude of the amplification factor $|F|$ normalised by the strong amplification $\sqrt{\mu} = 3.32$, corresponding to source position $\eta_{SIS} = [0.1]\theta_{SIS}$ and the corresponding phase $args(F)$ varying with frequency, for different densities of microlenses around Type 1 macroimage. The values of density are taken to be [30, 50, 70, 90, 107] $M_\odot/\text{pc}^2$. One row represents the corresponding plots for one mass distribution drawn from Chabrier IMF. The solid black lines illustrate the plotted values approaching strong lensing limit. The ASD of aLIGO is plotted in grey along with the corresponding value of strain.

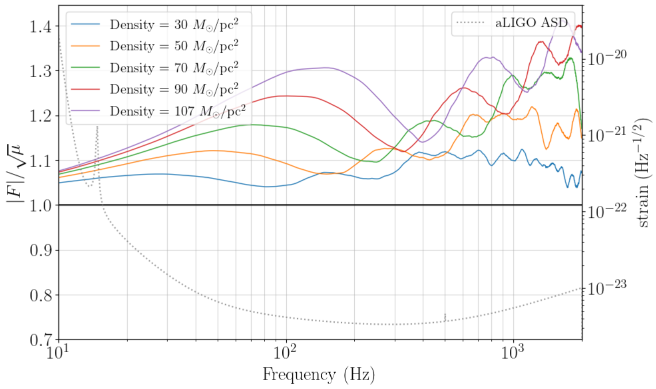

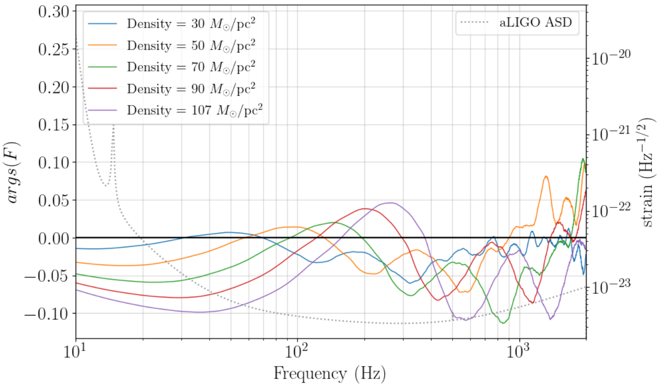

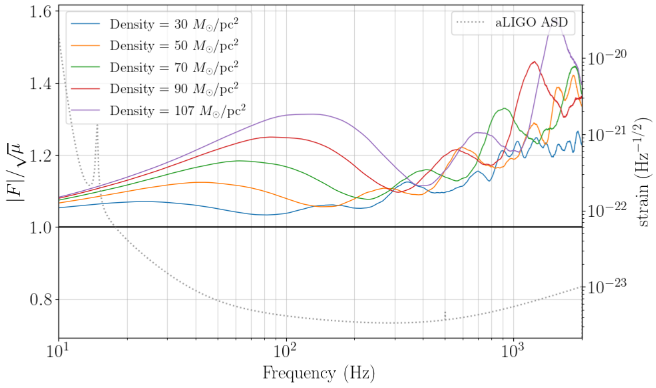

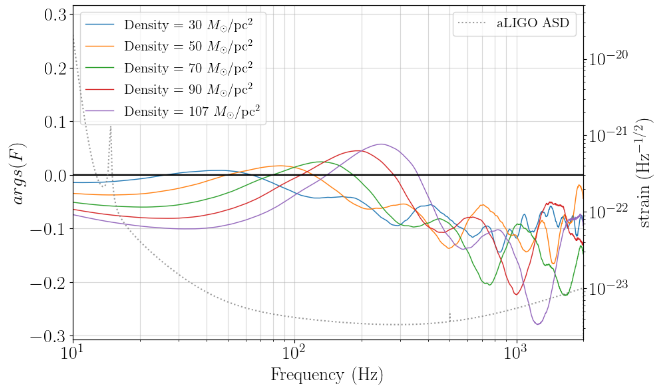

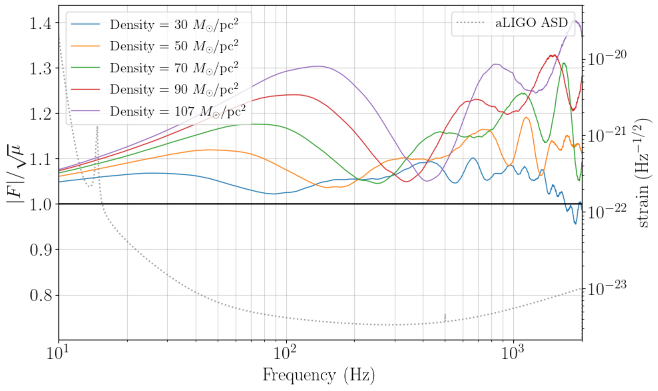
Density = 30 $M_\odot$/pc^2
Density = 50 $M_\odot$/pc^2
Density = 70 $M_\odot$/pc^2
Density = 90 $M_\odot$/pc^2
Density = 107 $M_\odot$/pc^2
aLIGO ASD
1.4
1.3
1.2
1.1
1.0
0.9
0.8
$|F|/\sqrt{\mu}$
10^{1}
10^{2}
10^{3}
Frequency (Hz)
10^{-20}
10^{-21}
10^{-22}
10^{-23}
strain (Hz$^{-1/2}$)

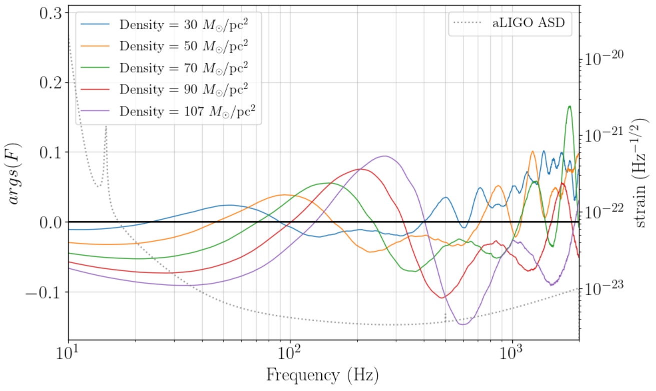
Density = 30 $M_\odot$/pc^2
Density = 50 $M_\odot$/pc^2
Density = 70 $M_\odot$/pc^2
Density = 90 $M_\odot$/pc^2
Density = 107 $M_\odot$/pc^2
aLIGO ASD
0.3
0.2
0.1
0.0
−0.1
$args(F)$
10^{1}
10^{2}
10^{3}
Frequency (Hz)
10^{-20}
10^{-21}
10^{-22}
10^{-23}
strain (Hz$^{-1/2}$)

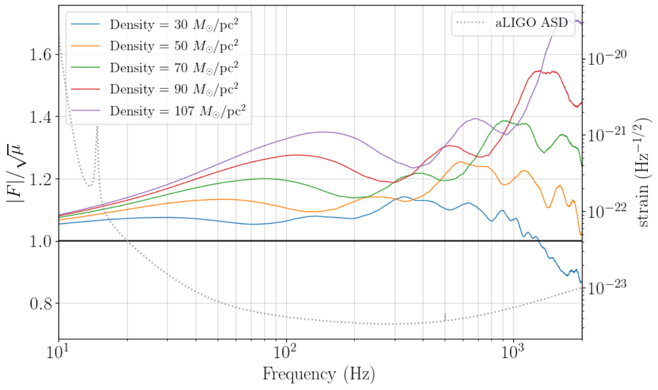
Density = 30 $M_\odot$/pc^2
Density = 50 $M_\odot$/pc^2
Density = 70 $M_\odot$/pc^2
Density = 90 $M_\odot$/pc^2
Density = 107 $M_\odot$/pc^2
aLIGO ASD
1.6
1.4
1.2
1.0
0.8
$|F|/\sqrt{\mu}$
10^{1}
10^{2}
10^{3}
Frequency (Hz)
10^{-20}
10^{-21}
10^{-22}
10^{-23}
strain (Hz$^{-1/2}$)

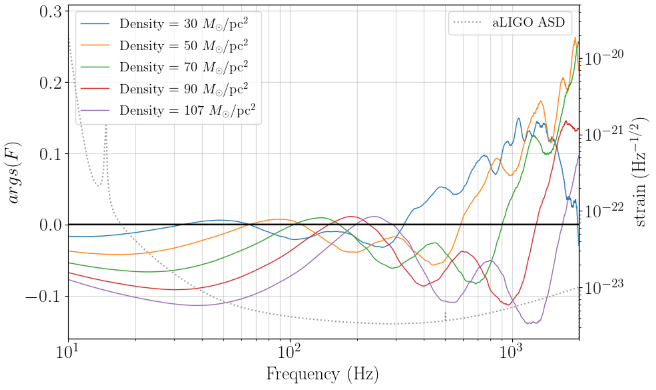
Density = 30 $M_\odot$/pc^2
Density = 50 $M_\odot$/pc^2
Density = 70 $M_\odot$/pc^2
Density = 90 $M_\odot$/pc^2
Density = 107 $M_\odot$/pc^2
aLIGO ASD
0.3
0.2
0.1
0.0
−0.1
$args(F)$
10^{1}
10^{2}
10^{3}
Frequency (Hz)
10^{-20}
10^{-21}
10^{-22}
10^{-23}
strain (Hz$^{-1/2}$)

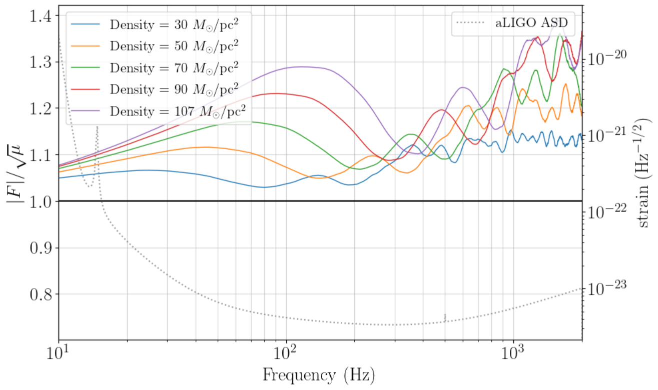
Density = 30 $M_\odot$/pc^2
Density = 50 $M_\odot$/pc^2
Density = 70 $M_\odot$/pc^2
Density = 90 $M_\odot$/pc^2
Density = 107 $M_\odot$/pc^2
aLIGO ASD
1.4
1.3
1.2
1.1
1.0
0.9
0.8
$|F|/\sqrt{\mu}$
10^{1}
10^{2}
10^{3}
Frequency (Hz)
10^{-20}
10^{-21}
10^{-22}
10^{-23}
strain (Hz$^{-1/2}$)

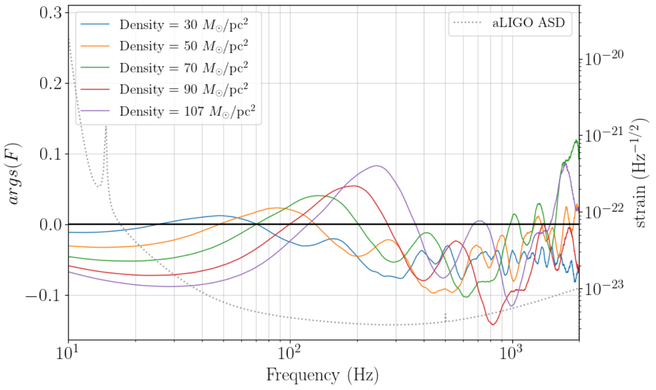
Density = 30 $M_\odot$/pc^2
Density = 50 $M_\odot$/pc^2
Density = 70 $M_\odot$/pc^2
Density = 90 $M_\odot$/pc^2
Density = 107 $M_\odot$/pc^2
aLIGO ASD
0.3
0.2
0.1
0.0
−0.1
$args(F)$
10^{1}
10^{2}
10^{3}
Frequency (Hz)
10^{-20}
10^{-21}
10^{-22}
10^{-23}
strain (Hz$^{-1/2}$)

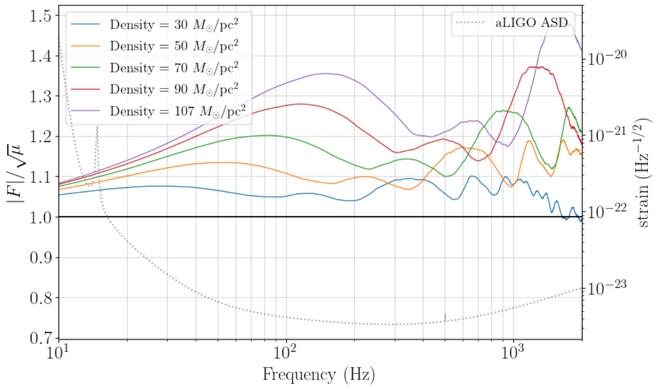
Density = 30 $M_\odot$/pc^2
Density = 50 $M_\odot$/pc^2
Density = 70 $M_\odot$/pc^2
Density = 90 $M_\odot$/pc^2
Density = 107 $M_\odot$/pc^2
aLIGO ASD
1.5
1.4
1.3
1.2
1.1
1.0
0.9
0.8
0.7
$|F|/\sqrt{\mu}$
10^{1}
10^{2}
10^{3}
Frequency (Hz)
10^{-20}
10^{-21}
10^{-22}
10^{-23}
strain (Hz$^{-1/2}$)

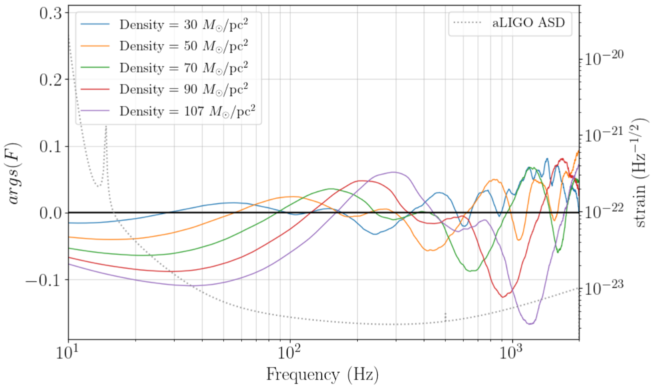
Density = 30 $M_\odot$/pc^2
Density = 50 $M_\odot$/pc^2
Density = 70 $M_\odot$/pc^2
Density = 90 $M_\odot$/pc^2
Density = 107 $M_\odot$/pc^2
aLIGO ASD
0.3
0.2
0.1
0.0
−0.1
$args(F)$
10^{1}
10^{2}
10^{3}
Frequency (Hz)
10^{-20}
10^{-21}
10^{-22}
10^{-23}
strain (Hz$^{-1/2}$)

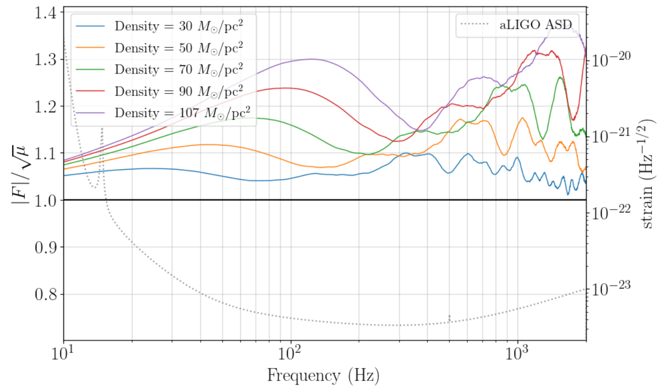
Density = 30 $M_\odot/\mathrm{pc}^2$
Density = 50 $M_\odot/\mathrm{pc}^2$
Density = 70 $M_\odot/\mathrm{pc}^2$
Density = 90 $M_\odot/\mathrm{pc}^2$
Density = 107 $M_\odot/\mathrm{pc}^2$
aLIGO ASD
$|F|/\sqrt{\mu}$
1.4
1.3
1.2
1.1
1.0
0.9
0.8
10^{-20}
10^{-21}
10^{-22}
10^{-23}
strain ($\mathrm{Hz}^{-1/2}$)
10^1
10^2
10^3
Frequency (Hz)

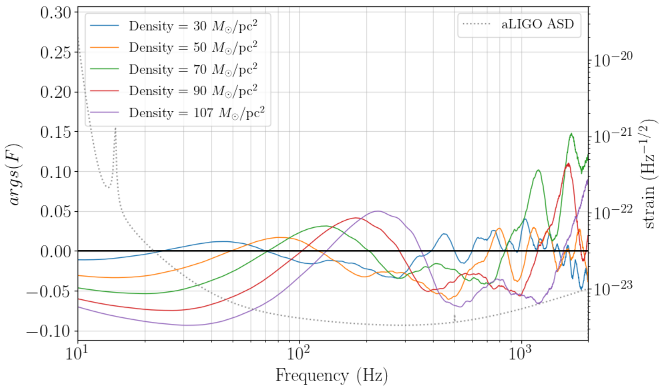
Density = 30 $M_\odot/\mathrm{pc}^2$
Density = 50 $M_\odot/\mathrm{pc}^2$
Density = 70 $M_\odot/\mathrm{pc}^2$
Density = 90 $M_\odot/\mathrm{pc}^2$
Density = 107 $M_\odot/\mathrm{pc}^2$
aLIGO ASD
$args(F)$
0.30
0.25
0.20
0.15
0.10
0.05
0.00
−0.05
−0.10
10^{-20}
10^{-21}
10^{-22}
10^{-23}
strain ($\mathrm{Hz}^{-1/2}$)
10^1
10^2
10^3
Frequency (Hz)

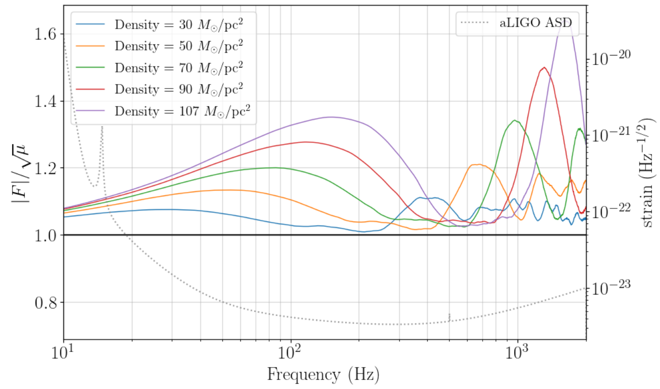
Density = 30 $M_\odot/\mathrm{pc}^2$
Density = 50 $M_\odot/\mathrm{pc}^2$
Density = 70 $M_\odot/\mathrm{pc}^2$
Density = 90 $M_\odot/\mathrm{pc}^2$
Density = 107 $M_\odot/\mathrm{pc}^2$
aLIGO ASD
$|F|/\sqrt{\mu}$
1.6
1.4
1.2
1.0
0.8
10^{-20}
10^{-21}
10^{-22}
10^{-23}
strain ($\mathrm{Hz}^{-1/2}$)
10^1
10^2
10^3
Frequency (Hz)

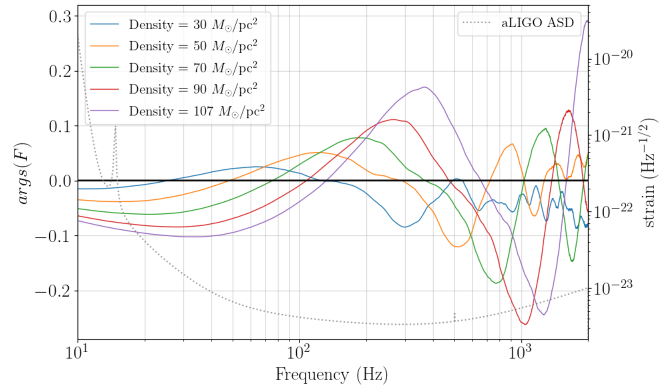
Density = 30 $M_\odot/\mathrm{pc}^2$
Density = 50 $M_\odot/\mathrm{pc}^2$
Density = 70 $M_\odot/\mathrm{pc}^2$
Density = 90 $M_\odot/\mathrm{pc}^2$
Density = 107 $M_\odot/\mathrm{pc}^2$
aLIGO ASD
$args(F)$
0.3
0.2
0.1
0.0
−0.1
−0.2
10^{-20}
10^{-21}
10^{-22}
10^{-23}
strain ($\mathrm{Hz}^{-1/2}$)
10^1
10^2
10^3
Frequency (Hz)

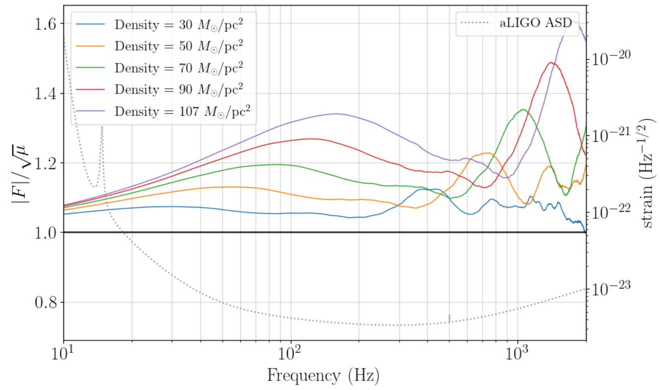
Density = 30 $M_\odot/\mathrm{pc}^2$
Density = 50 $M_\odot/\mathrm{pc}^2$
Density = 70 $M_\odot/\mathrm{pc}^2$
Density = 90 $M_\odot/\mathrm{pc}^2$
Density = 107 $M_\odot/\mathrm{pc}^2$
aLIGO ASD
$|F|/\sqrt{\mu}$
1.6
1.4
1.2
1.0
0.8
10^{-20}
10^{-21}
10^{-22}
10^{-23}
strain ($\mathrm{Hz}^{-1/2}$)
10^1
10^2
10^3
Frequency (Hz)

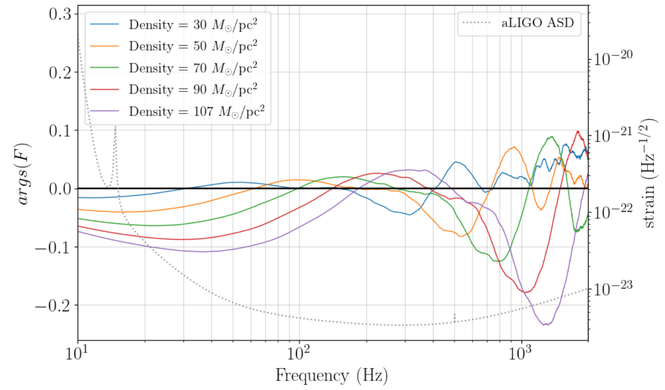
Density = 30 $M_\odot/\mathrm{pc}^2$
Density = 50 $M_\odot/\mathrm{pc}^2$
Density = 70 $M_\odot/\mathrm{pc}^2$
Density = 90 $M_\odot/\mathrm{pc}^2$
Density = 107 $M_\odot/\mathrm{pc}^2$
aLIGO ASD
$args(F)$
0.3
0.2
0.1
0.0
−0.1
−0.2
10^{-20}
10^{-21}
10^{-22}
10^{-23}
strain ($\mathrm{Hz}^{-1/2}$)
10^1
10^2
10^3
Frequency (Hz)

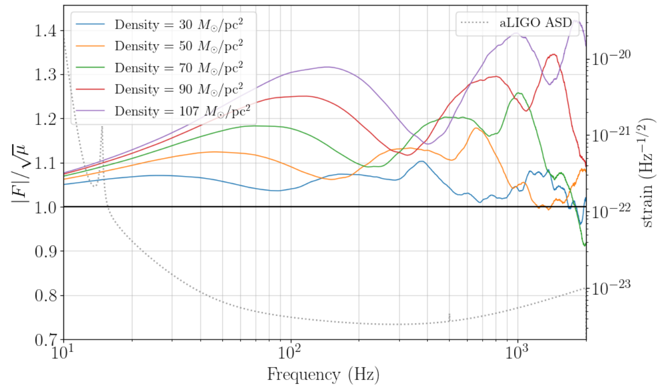
Density = 30 $M_\odot/\mathrm{pc}^2$
Density = 50 $M_\odot/\mathrm{pc}^2$
Density = 70 $M_\odot/\mathrm{pc}^2$
Density = 90 $M_\odot/\mathrm{pc}^2$
Density = 107 $M_\odot/\mathrm{pc}^2$
aLIGO ASD
$|F|/\sqrt{\mu}$
1.4
1.3
1.2
1.1
1.0
0.9
0.8
0.7
10^{-20}
10^{-21}
10^{-22}
10^{-23}
strain ($\mathrm{Hz}^{-1/2}$)
10^1
10^2
10^3
Frequency (Hz)

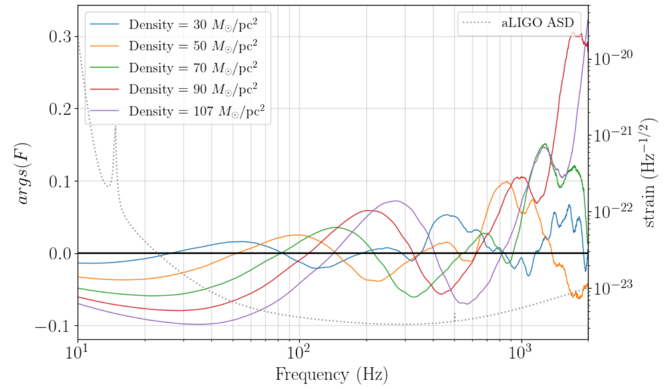
Density = 30 $M_\odot/\mathrm{pc}^2$
Density = 50 $M_\odot/\mathrm{pc}^2$
Density = 70 $M_\odot/\mathrm{pc}^2$
Density = 90 $M_\odot/\mathrm{pc}^2$
Density = 107 $M_\odot/\mathrm{pc}^2$
aLIGO ASD
$args(F)$
0.3
0.2
0.1
0.0
−0.1
10^{-20}
10^{-21}
10^{-22}
10^{-23}
strain ($\mathrm{Hz}^{-1/2}$)
10^1
10^2
10^3
Frequency (Hz)

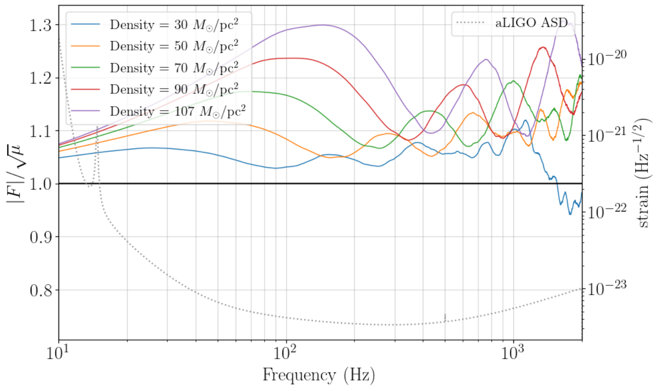
Density = 30 $M_\odot/\mathrm{pc}^2$
Density = 50 $M_\odot/\mathrm{pc}^2$
Density = 70 $M_\odot/\mathrm{pc}^2$
Density = 90 $M_\odot/\mathrm{pc}^2$
Density = 107 $M_\odot/\mathrm{pc}^2$
aLIGO ASD
$|F|/\sqrt{\mu}$
1.3
1.2
1.1
1.0
0.9
0.8
10^{-20}
10^{-21}
10^{-22}
10^{-23}
strain (Hz$^{-1/2}$)
10^1
10^2
10^3
Frequency (Hz)

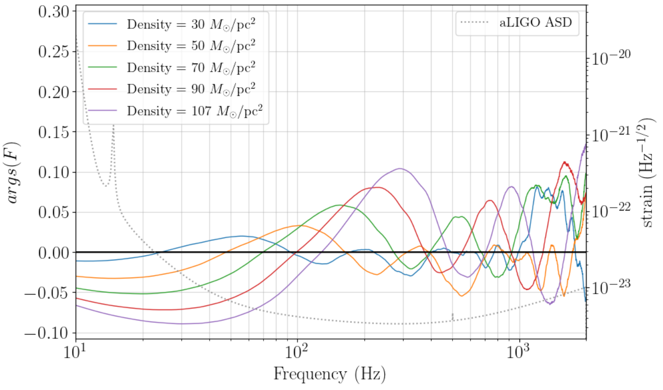
Density = 30 $M_\odot/\mathrm{pc}^2$
Density = 50 $M_\odot/\mathrm{pc}^2$
Density = 70 $M_\odot/\mathrm{pc}^2$
Density = 90 $M_\odot/\mathrm{pc}^2$
Density = 107 $M_\odot/\mathrm{pc}^2$
aLIGO ASD
$args(F)$
0.30
0.25
0.20
0.15
0.10
0.05
0.00
−0.05
−0.10
10^{-20}
10^{-21}
10^{-22}
10^{-23}
strain (Hz$^{-1/2}$)
10^1
10^2
10^3
Frequency (Hz)

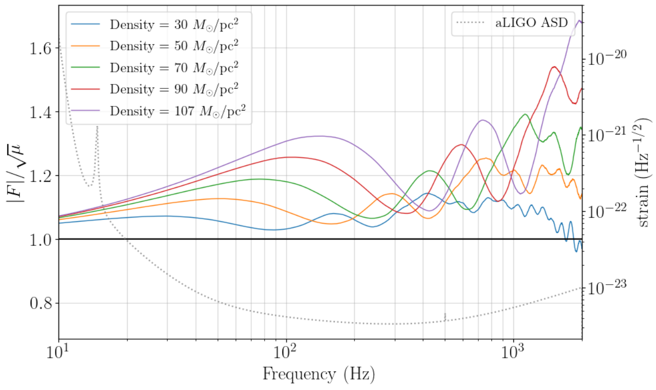
Density = 30 $M_\odot/\mathrm{pc}^2$
Density = 50 $M_\odot/\mathrm{pc}^2$
Density = 70 $M_\odot/\mathrm{pc}^2$
Density = 90 $M_\odot/\mathrm{pc}^2$
Density = 107 $M_\odot/\mathrm{pc}^2$
aLIGO ASD
$|F|/\sqrt{\mu}$
1.6
1.4
1.2
1.0
0.8
10^{-20}
10^{-21}
10^{-22}
10^{-23}
strain (Hz$^{-1/2}$)
10^1
10^2
10^3
Frequency (Hz)

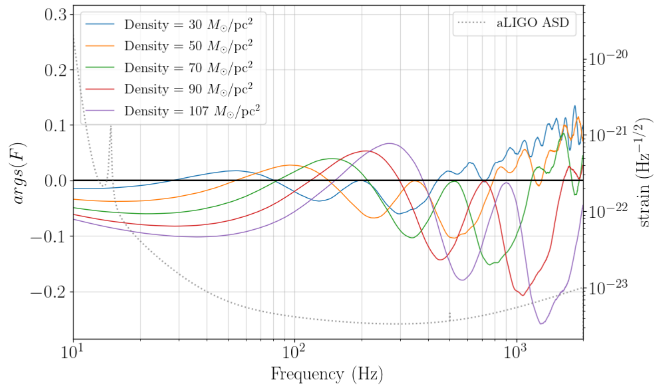
Density = 30 $M_\odot/\mathrm{pc}^2$
Density = 50 $M_\odot/\mathrm{pc}^2$
Density = 70 $M_\odot/\mathrm{pc}^2$
Density = 90 $M_\odot/\mathrm{pc}^2$
Density = 107 $M_\odot/\mathrm{pc}^2$
aLIGO ASD
$args(F)$
0.3
0.2
0.1
0.0
−0.1
−0.2
10^{-20}
10^{-21}
10^{-22}
10^{-23}
strain (Hz$^{-1/2}$)
10^1
10^2
10^3
Frequency (Hz)

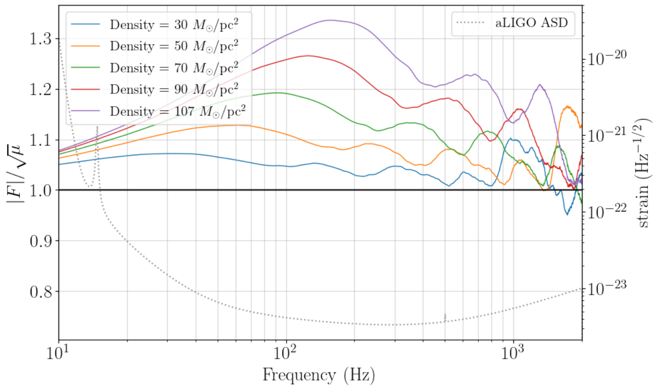
Density = 30 $M_\odot/\mathrm{pc}^2$
Density = 50 $M_\odot/\mathrm{pc}^2$
Density = 70 $M_\odot/\mathrm{pc}^2$
Density = 90 $M_\odot/\mathrm{pc}^2$
Density = 107 $M_\odot/\mathrm{pc}^2$
aLIGO ASD
$|F|/\sqrt{\mu}$
1.3
1.2
1.1
1.0
0.9
0.8
10^{-20}
10^{-21}
10^{-22}
10^{-23}
strain (Hz$^{-1/2}$)
10^1
10^2
10^3
Frequency (Hz)

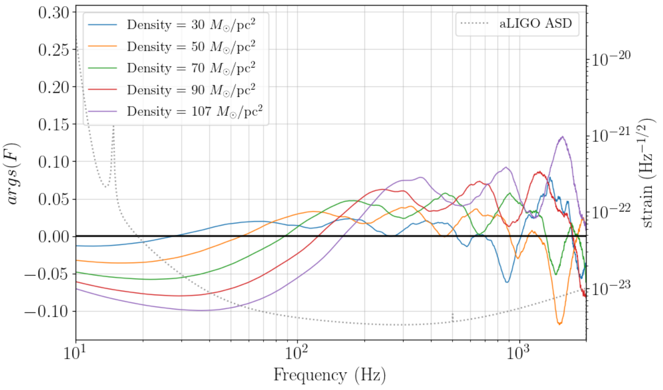
Density = 30 $M_\odot/\mathrm{pc}^2$
Density = 50 $M_\odot/\mathrm{pc}^2$
Density = 70 $M_\odot/\mathrm{pc}^2$
Density = 90 $M_\odot/\mathrm{pc}^2$
Density = 107 $M_\odot/\mathrm{pc}^2$
aLIGO ASD
$args(F)$
0.30
0.25
0.20
0.15
0.10
0.05
0.00
−0.05
−0.10
10^{-20}
10^{-21}
10^{-22}
10^{-23}
strain (Hz$^{-1/2}$)
10^1
10^2
10^3
Frequency (Hz)

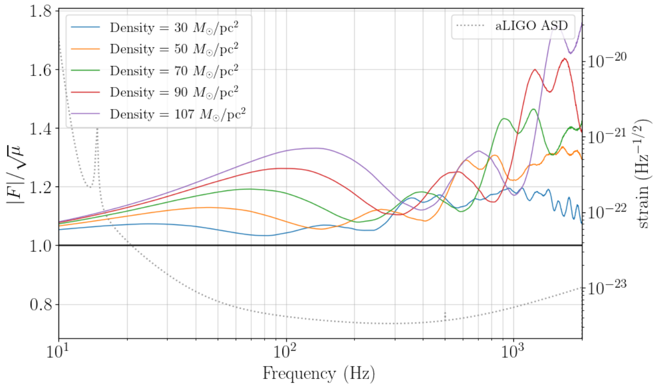
Density = 30 $M_\odot/\mathrm{pc}^2$
Density = 50 $M_\odot/\mathrm{pc}^2$
Density = 70 $M_\odot/\mathrm{pc}^2$
Density = 90 $M_\odot/\mathrm{pc}^2$
Density = 107 $M_\odot/\mathrm{pc}^2$
aLIGO ASD
$|F|/\sqrt{\mu}$
1.8
1.6
1.4
1.2
1.0
0.8
10^{-20}
10^{-21}
10^{-22}
10^{-23}
strain (Hz$^{-1/2}$)
10^1
10^2
10^3
Frequency (Hz)

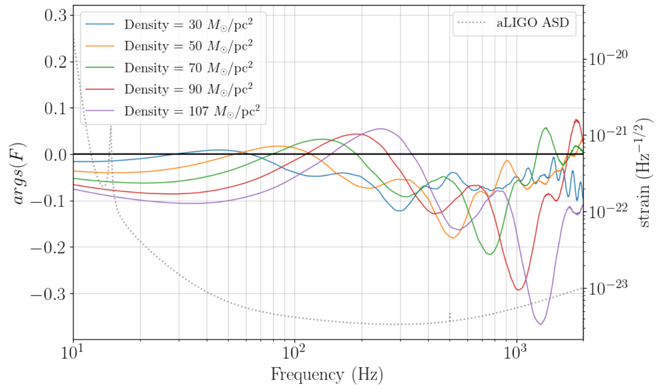
Density = 30 $M_\odot/\mathrm{pc}^2$
Density = 50 $M_\odot/\mathrm{pc}^2$
Density = 70 $M_\odot/\mathrm{pc}^2$
Density = 90 $M_\odot/\mathrm{pc}^2$
Density = 107 $M_\odot/\mathrm{pc}^2$
aLIGO ASD
$args(F)$
0.3
0.2
0.1
0.0
−0.1
−0.2
−0.3
10^{-20}
10^{-21}
10^{-22}
10^{-23}
strain (Hz$^{-1/2}$)
10^1
10^2
10^3
Frequency (Hz)

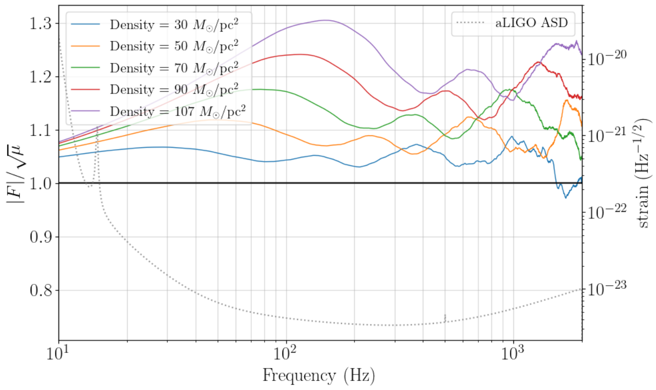
Density = 30 $M_\odot/\mathrm{pc}^2$
Density = 50 $M_\odot/\mathrm{pc}^2$
Density = 70 $M_\odot/\mathrm{pc}^2$
Density = 90 $M_\odot/\mathrm{pc}^2$
Density = 107 $M_\odot/\mathrm{pc}^2$
aLIGO ASD
$|F|/\sqrt{\mu}$
1.3
1.2
1.1
1.0
0.9
0.8
10^1
10^2
10^3
Frequency (Hz)
10^{-20}
10^{-21}
10^{-22}
10^{-23}
strain ($\mathrm{Hz}^{-1/2}$)

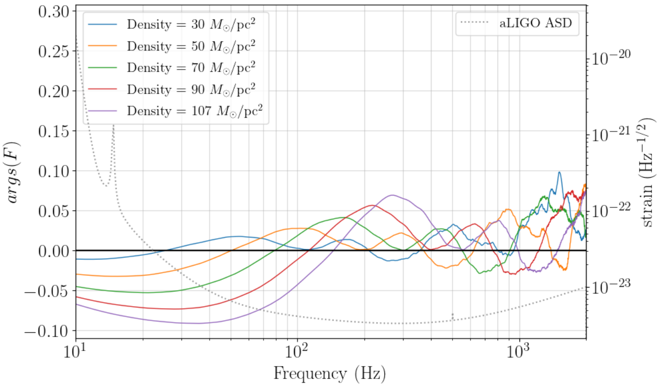
Density = 30 $M_\odot/\mathrm{pc}^2$
Density = 50 $M_\odot/\mathrm{pc}^2$
Density = 70 $M_\odot/\mathrm{pc}^2$
Density = 90 $M_\odot/\mathrm{pc}^2$
Density = 107 $M_\odot/\mathrm{pc}^2$
aLIGO ASD
$args(F)$
0.30
0.25
0.20
0.15
0.10
0.05
0.00
−0.05
−0.10
10^1
10^2
10^3
Frequency (Hz)
10^{-20}
10^{-21}
10^{-22}
10^{-23}
strain ($\mathrm{Hz}^{-1/2}$)

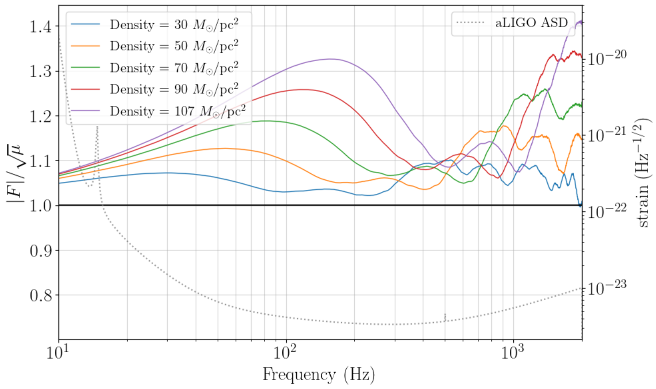
Density = 30 $M_\odot/\mathrm{pc}^2$
Density = 50 $M_\odot/\mathrm{pc}^2$
Density = 70 $M_\odot/\mathrm{pc}^2$
Density = 90 $M_\odot/\mathrm{pc}^2$
Density = 107 $M_\odot/\mathrm{pc}^2$
aLIGO ASD
$|F|/\sqrt{\mu}$
1.4
1.3
1.2
1.1
1.0
0.9
0.8
10^1
10^2
10^3
Frequency (Hz)
10^{-20}
10^{-21}
10^{-22}
10^{-23}
strain ($\mathrm{Hz}^{-1/2}$)

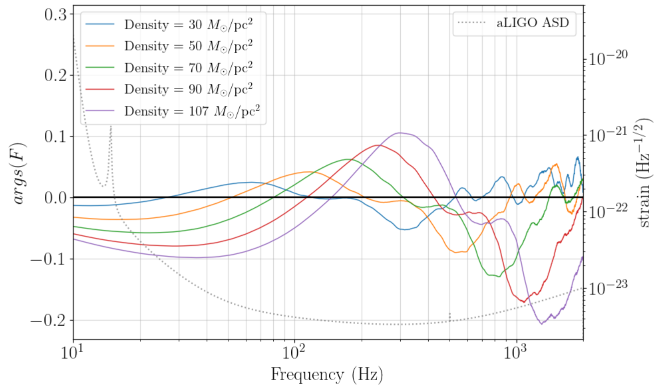
Density = 30 $M_\odot/\mathrm{pc}^2$
Density = 50 $M_\odot/\mathrm{pc}^2$
Density = 70 $M_\odot/\mathrm{pc}^2$
Density = 90 $M_\odot/\mathrm{pc}^2$
Density = 107 $M_\odot/\mathrm{pc}^2$
aLIGO ASD
$args(F)$
0.3
0.2
0.1
0.0
−0.1
−0.2
10^1
10^2
10^3
Frequency (Hz)
10^{-20}
10^{-21}
10^{-22}
10^{-23}
strain ($\mathrm{Hz}^{-1/2}$)

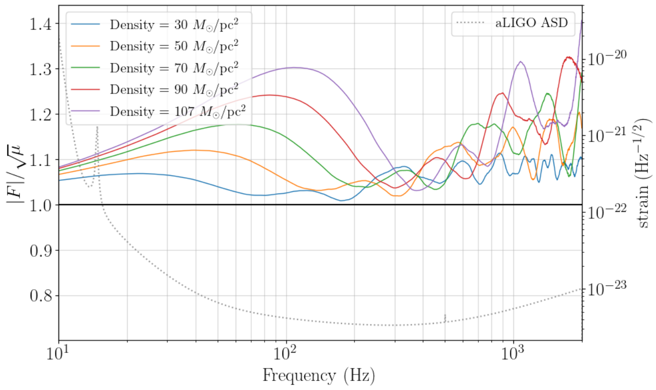
Density = 30 $M_\odot/\mathrm{pc}^2$
Density = 50 $M_\odot/\mathrm{pc}^2$
Density = 70 $M_\odot/\mathrm{pc}^2$
Density = 90 $M_\odot/\mathrm{pc}^2$
Density = 107 $M_\odot/\mathrm{pc}^2$
aLIGO ASD
$|F|/\sqrt{\mu}$
1.4
1.3
1.2
1.1
1.0
0.9
0.8
10^1
10^2
10^3
Frequency (Hz)
10^{-20}
10^{-21}
10^{-22}
10^{-23}
strain ($\mathrm{Hz}^{-1/2}$)

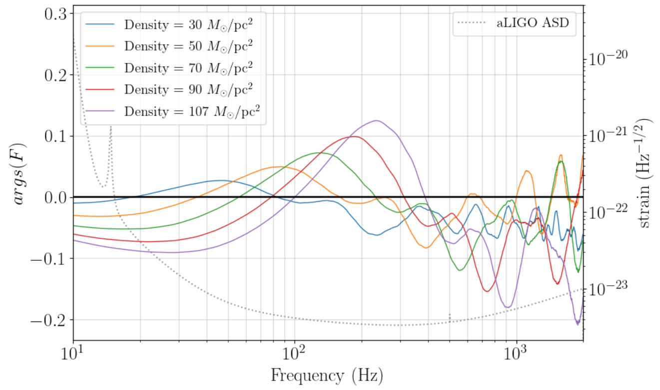
Density = 30 $M_\odot/\mathrm{pc}^2$
Density = 50 $M_\odot/\mathrm{pc}^2$
Density = 70 $M_\odot/\mathrm{pc}^2$
Density = 90 $M_\odot/\mathrm{pc}^2$
Density = 107 $M_\odot/\mathrm{pc}^2$
aLIGO ASD
$args(F)$
0.3
0.2
0.1
0.0
−0.1
−0.2
10^1
10^2
10^3
Frequency (Hz)
10^{-20}
10^{-21}
10^{-22}
10^{-23}
strain ($\mathrm{Hz}^{-1/2}$)

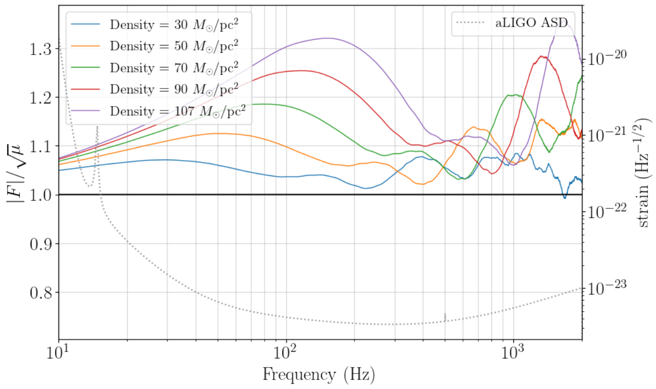
Density = 30 $M_\odot/\mathrm{pc}^2$
Density = 50 $M_\odot/\mathrm{pc}^2$
Density = 70 $M_\odot/\mathrm{pc}^2$
Density = 90 $M_\odot/\mathrm{pc}^2$
Density = 107 $M_\odot/\mathrm{pc}^2$
aLIGO ASD
$|F|/\sqrt{\mu}$
1.3
1.2
1.1
1.0
0.9
0.8
10^1
10^2
10^3
Frequency (Hz)
10^{-20}
10^{-21}
10^{-22}
10^{-23}
strain ($\mathrm{Hz}^{-1/2}$)

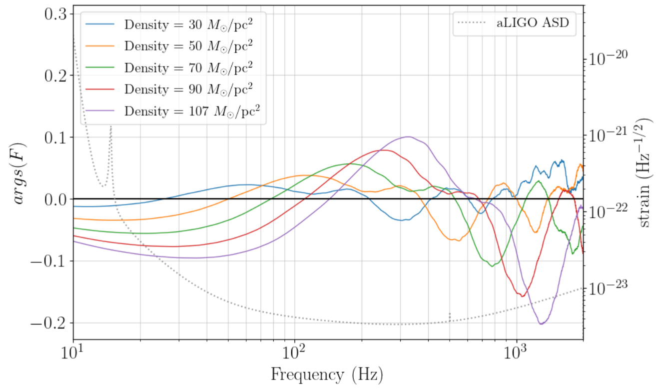
Density = 30 $M_\odot/\mathrm{pc}^2$
Density = 50 $M_\odot/\mathrm{pc}^2$
Density = 70 $M_\odot/\mathrm{pc}^2$
Density = 90 $M_\odot/\mathrm{pc}^2$
Density = 107 $M_\odot/\mathrm{pc}^2$
aLIGO ASD
$args(F)$
0.3
0.2
0.1
0.0
−0.1
−0.2
10^1
10^2
10^3
Frequency (Hz)
10^{-20}
10^{-21}
10^{-22}
10^{-23}
strain ($\mathrm{Hz}^{-1/2}$)

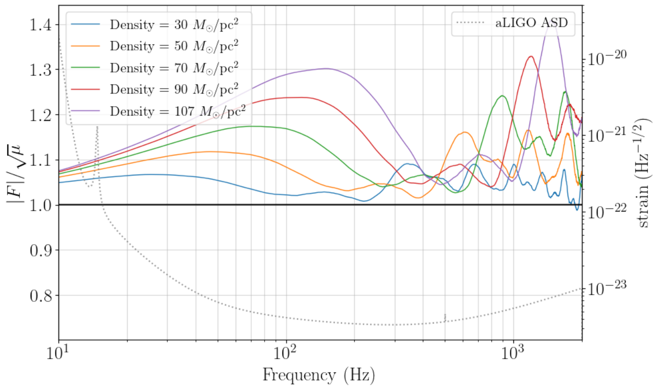
Density = 30 $M_\odot/\mathrm{pc}^2$
Density = 50 $M_\odot/\mathrm{pc}^2$
Density = 70 $M_\odot/\mathrm{pc}^2$
Density = 90 $M_\odot/\mathrm{pc}^2$
Density = 107 $M_\odot/\mathrm{pc}^2$
aLIGO ASD
1.4
1.3
1.2
1.1
1.0
0.9
0.8
$|F|/\sqrt{\mu}$
10^{-20}
10^{-21}
10^{-22}
10^{-23}
strain ($\mathrm{Hz}^{-1/2}$)
10^1
10^2
10^3
Frequency (Hz)

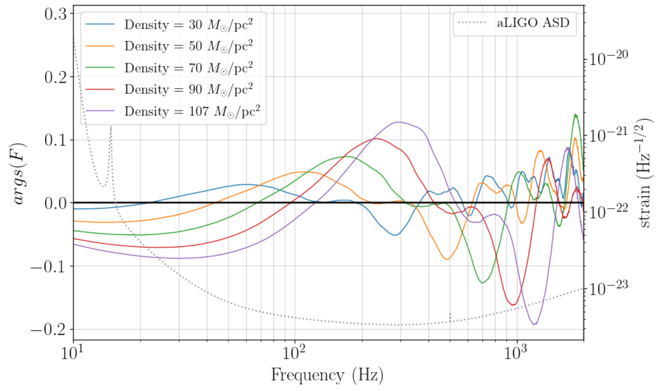
Density = 30 $M_\odot/\mathrm{pc}^2$
Density = 50 $M_\odot/\mathrm{pc}^2$
Density = 70 $M_\odot/\mathrm{pc}^2$
Density = 90 $M_\odot/\mathrm{pc}^2$
Density = 107 $M_\odot/\mathrm{pc}^2$
aLIGO ASD
0.3
0.2
0.1
0.0
−0.1
−0.2
$args(F)$
10^{-20}
10^{-21}
10^{-22}
10^{-23}
strain ($\mathrm{Hz}^{-1/2}$)
10^1
10^2
10^3
Frequency (Hz)

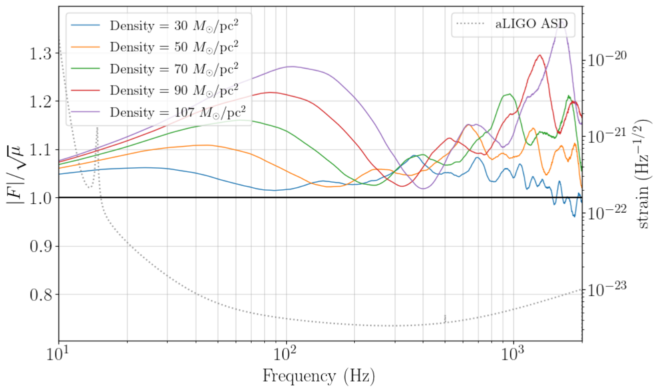
Density = 30 $M_\odot/\mathrm{pc}^2$
Density = 50 $M_\odot/\mathrm{pc}^2$
Density = 70 $M_\odot/\mathrm{pc}^2$
Density = 90 $M_\odot/\mathrm{pc}^2$
Density = 107 $M_\odot/\mathrm{pc}^2$
aLIGO ASD
1.3
1.2
1.1
1.0
0.9
0.8
$|F|/\sqrt{\mu}$
10^{-20}
10^{-21}
10^{-22}
10^{-23}
strain ($\mathrm{Hz}^{-1/2}$)
10^1
10^2
10^3
Frequency (Hz)

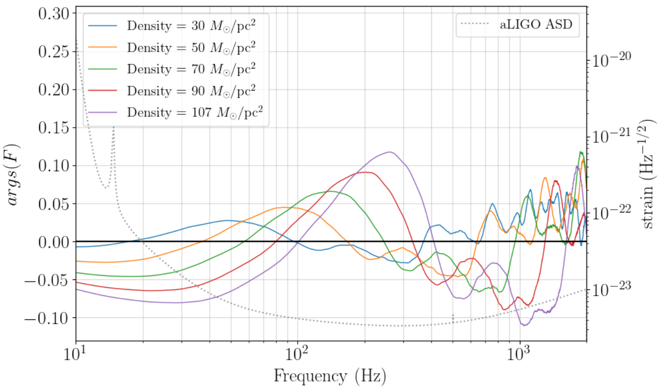
Density = 30 $M_\odot/\mathrm{pc}^2$
Density = 50 $M_\odot/\mathrm{pc}^2$
Density = 70 $M_\odot/\mathrm{pc}^2$
Density = 90 $M_\odot/\mathrm{pc}^2$
Density = 107 $M_\odot/\mathrm{pc}^2$
aLIGO ASD
0.30
0.25
0.20
0.15
0.10
0.05
0.00
−0.05
−0.10
$args(F)$
10^{-20}
10^{-21}
10^{-22}
10^{-23}
strain ($\mathrm{Hz}^{-1/2}$)
10^1
10^2
10^3
Frequency (Hz)

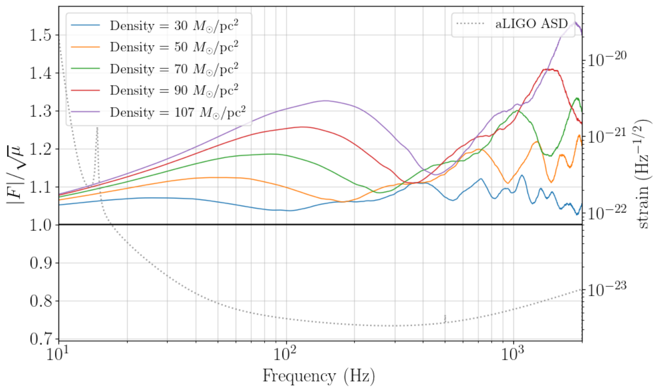
Density = 30 $M_\odot/\mathrm{pc}^2$
Density = 50 $M_\odot/\mathrm{pc}^2$
Density = 70 $M_\odot/\mathrm{pc}^2$
Density = 90 $M_\odot/\mathrm{pc}^2$
Density = 107 $M_\odot/\mathrm{pc}^2$
aLIGO ASD
1.5
1.4
1.3
1.2
1.1
1.0
0.9
0.8
0.7
$|F|/\sqrt{\mu}$
10^{-20}
10^{-21}
10^{-22}
10^{-23}
strain ($\mathrm{Hz}^{-1/2}$)
10^1
10^2
10^3
Frequency (Hz)

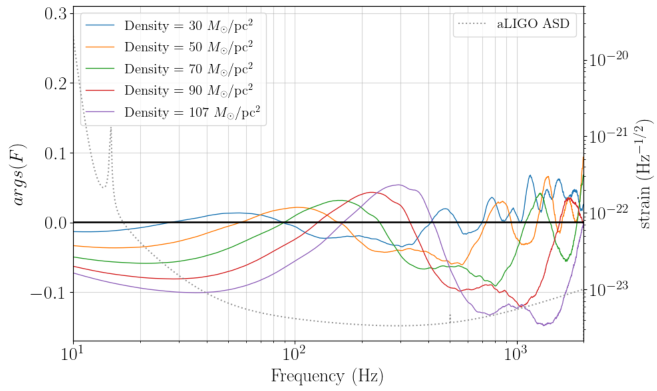
Density = 30 $M_\odot/\mathrm{pc}^2$
Density = 50 $M_\odot/\mathrm{pc}^2$
Density = 70 $M_\odot/\mathrm{pc}^2$
Density = 90 $M_\odot/\mathrm{pc}^2$
Density = 107 $M_\odot/\mathrm{pc}^2$
aLIGO ASD
0.3
0.2
0.1
0.0
−0.1
$args(F)$
10^{-20}
10^{-21}
10^{-22}
10^{-23}
strain ($\mathrm{Hz}^{-1/2}$)
10^1
10^2
10^3
Frequency (Hz)

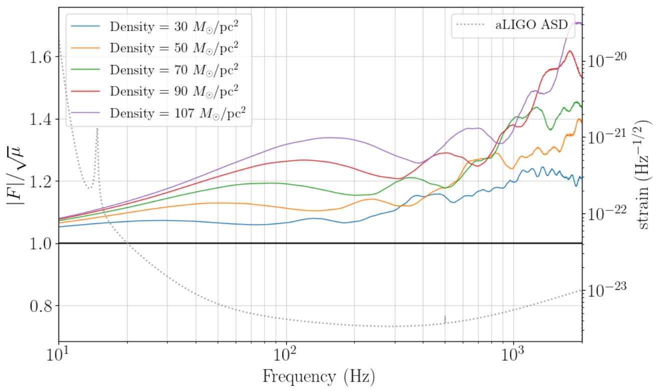
Density = 30 $M_\odot/\mathrm{pc}^2$
Density = 50 $M_\odot/\mathrm{pc}^2$
Density = 70 $M_\odot/\mathrm{pc}^2$
Density = 90 $M_\odot/\mathrm{pc}^2$
Density = 107 $M_\odot/\mathrm{pc}^2$
aLIGO ASD
1.6
1.4
1.2
1.0
0.8
$|F|/\sqrt{\mu}$
10^{-20}
10^{-21}
10^{-22}
10^{-23}
strain ($\mathrm{Hz}^{-1/2}$)
10^1
10^2
10^3
Frequency (Hz)

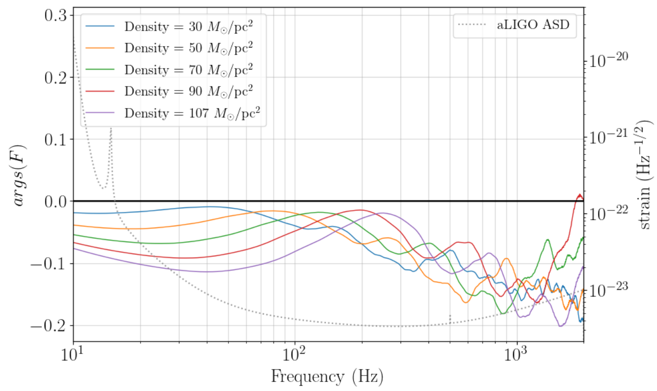
Density = 30 $M_\odot/\mathrm{pc}^2$
Density = 50 $M_\odot/\mathrm{pc}^2$
Density = 70 $M_\odot/\mathrm{pc}^2$
Density = 90 $M_\odot/\mathrm{pc}^2$
Density = 107 $M_\odot/\mathrm{pc}^2$
aLIGO ASD
0.3
0.2
0.1
0.0
−0.1
−0.2
$args(F)$
10^{-20}
10^{-21}
10^{-22}
10^{-23}
strain ($\mathrm{Hz}^{-1/2}$)
10^1
10^2
10^3
Frequency (Hz)

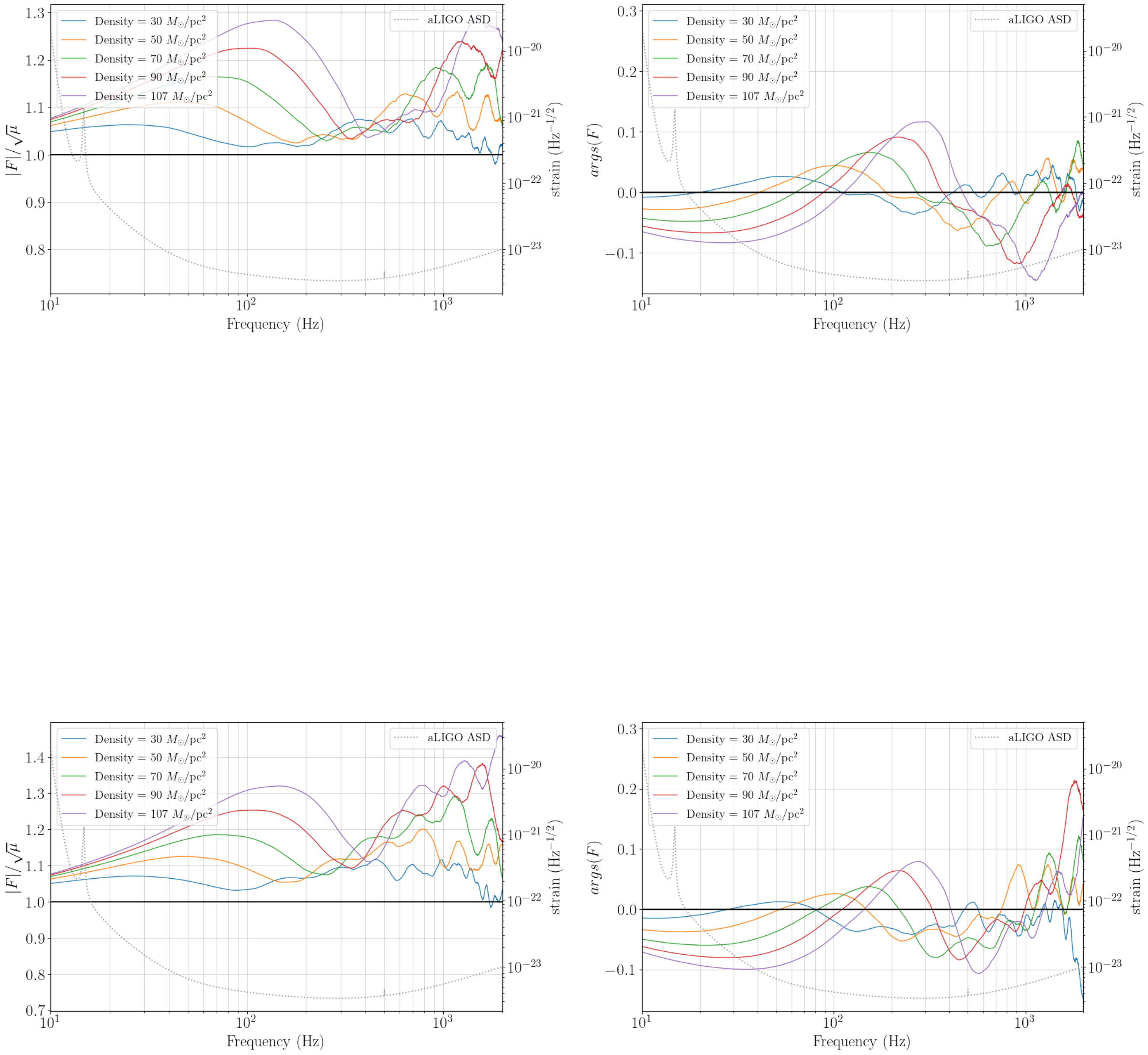

Figure 8.25: 24 panels above show the amplification factor graphs for the variation with density for different mass distributions. One row represents the corresponding plots for one mass distribution. The remaining description of the plots is the same as discussed in the start of this section.

8.3 Amplification Factor Graphs for the Variation with Source Position for different distributions

Following the setup description in section 6.2.2, below are the graphs for the amplitude $|F|$ normalised by the strong amplification $\sqrt{\mu}$ and the corresponding phase $args(F)$, varying with frequency for source positions $[\eta_{SIS} = [0.03, 0.8]\theta_{SIS}]$ and hence macro-amplifications $[\sqrt{\mu} = 5.86, 1.50]$ for a particular density 90 $M_{\odot}/\mathrm{pc}^2$. The solid black lines illustrate the plotted values approaching strong lensing limit. The ASD of aLIGO is plotted in grey along with the corresponding value of strain. The same colors are representative of the same mass distribution in a row.

The plots below (fig. 8.26) show the normalised amplitude $|F|/\sqrt{\mu}$ and phase $args(F)$ variation with frequency for the source position $\eta_{SIS} = [0.8]\theta_{SIS}$ for remaining 9 random mass distributions drawn from the Chabrier IMF.

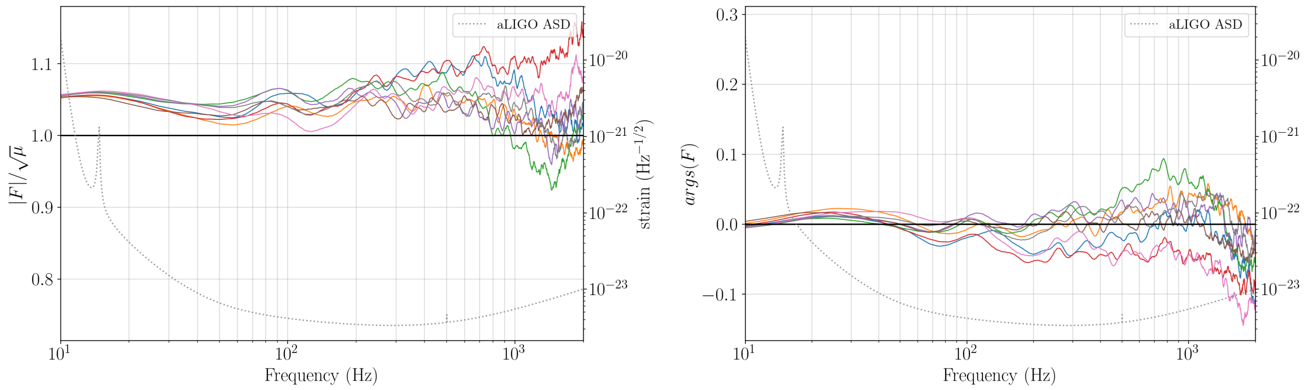

Figure 8.26: Amplification Factor Graphs for $\eta_{SIS} = [0.8]\theta_{SIS}$ for different distributions. The remaining description of the plots is the same as discussed in the start of this section and the paragraph above.

The plots below (fig. 8.27) show the normalised amplitude $|F|/\sqrt{\mu}$ and phase $args(F)$ variation with frequency for the source position $\eta_{SIS} = [0.03]\theta_{SIS}$ for remaining 9 random mass distributions drawn from the Chabrier IMF.
The corresponding plots for normalised amplitude $|F|/\sqrt{\mu}$ and phase variation args(F) for the amplification factor $F(f)$ for the source position $\eta_{SIS} = [0.1]\theta_{SIS}$ and are already presented in the section 8.2.

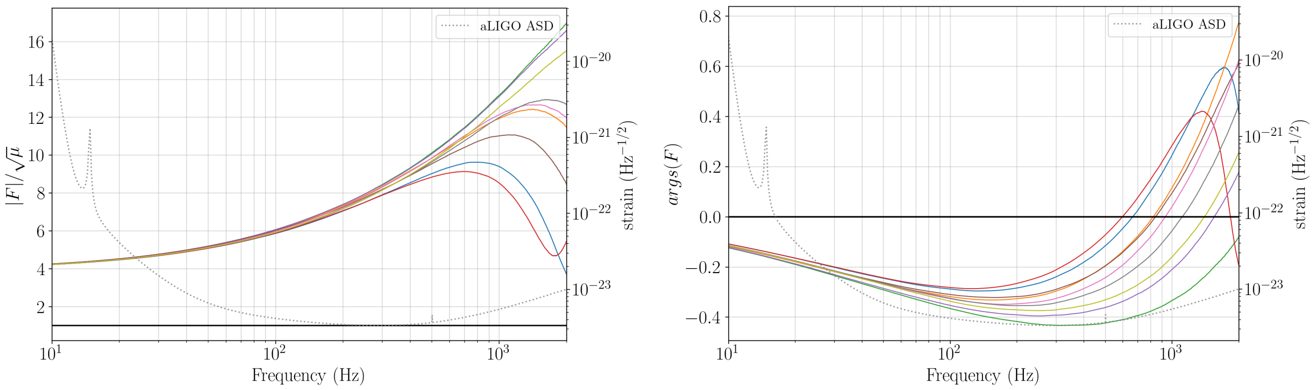

Figure 8.27: Amplification Factor Graphs for $\eta_{SIS} = [0.03]\theta_{SIS}$ for different distributions. The remaining description of the plots is the same as discussed in the start of this section and the paragraph above

8.4 Amplification Factor Variation Graphs for the Variation with IMF for different distributions

Following the setup in section 6.2.3 below are the graphs for the amplitude $|F|$ normalised by the strong amplification $\sqrt{\mu}$ and the corresponding phase $args(F)$, varying with frequency for Kroupa and Scalo IMF. The solid black lines illustrate the plotted values approaching strong lensing limit. The ASD of aLIGO is plotted in grey along with the corresponding value of strain. The same colors are representative of the same mass distribution in a row.

The plots below (fig. 8.28) show the amplitude and phase variation of Amplification factor for remaining 9 random mass distributions drawn from Scalo IMF.

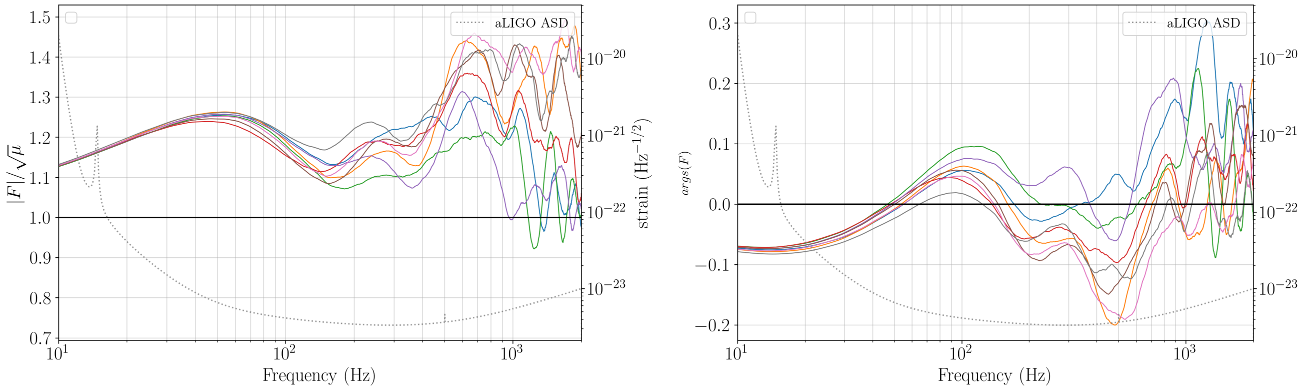

Figure 8.28: Amplification Factor Graphs for Scalo IMF for different distributions. The remaining description of the plots is the same as discussed in the start of this section and the paragraph above.

The plots below (fig. 8.29) show the amplitude and phase variation of Amplification factor for remaining 9 random mass distributions drawn from Kroupa IMF.

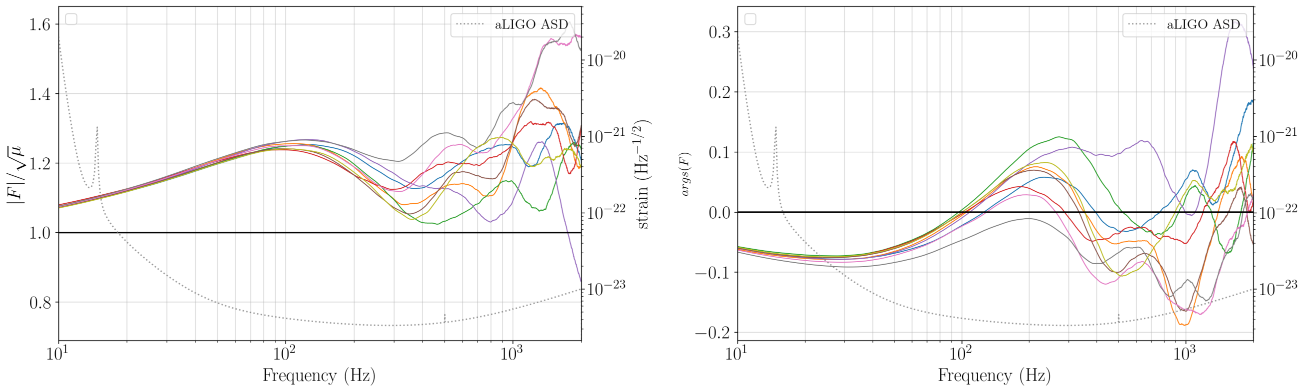

Figure 8.29: Amplification Factor Graphs for Kroupa IMF for different distributions. The remaining description of the plots is the same as discussed in the start of this section and the paragraph above

The corresponding plots for Chabrier IMF are already presented in the section 8.2.

8.5 Amplification Factor Variation Graphs for Integration Window Size

Following (fig. 8.32) are the graphs for the amplitude $|F|$ normalised by the strong amplification $\sqrt{\mu}$ and the corresponding phase $args(F)$, varying with frequency for different window sizes for different setups used throughout the thesis. The solid black lines illustrate the plotted values approaching strong lensing limit. The ASD of aLIGO is plotted in grey along with the corresponding value of strain. The original window size used throughout the thesis is plotted in orange and the corresponding plot for double the window size is in blue. The overlap of the amplification factor curves for the original and the doubled window size for all the cases below illustrate that the original window size is sufficient for the computation throughout the thesis.

The plots below show the amplitude and phase variation of Amplification factor for the setup described in section 6.2.1 for density = 107 $M_{\odot}/\mathrm{pc}^2$. (Thus corresponding density and source position are 107 $M_{\odot}/\mathrm{pc}^2$, $\eta_{SIS} = [0.1]\theta_{SIS}$).

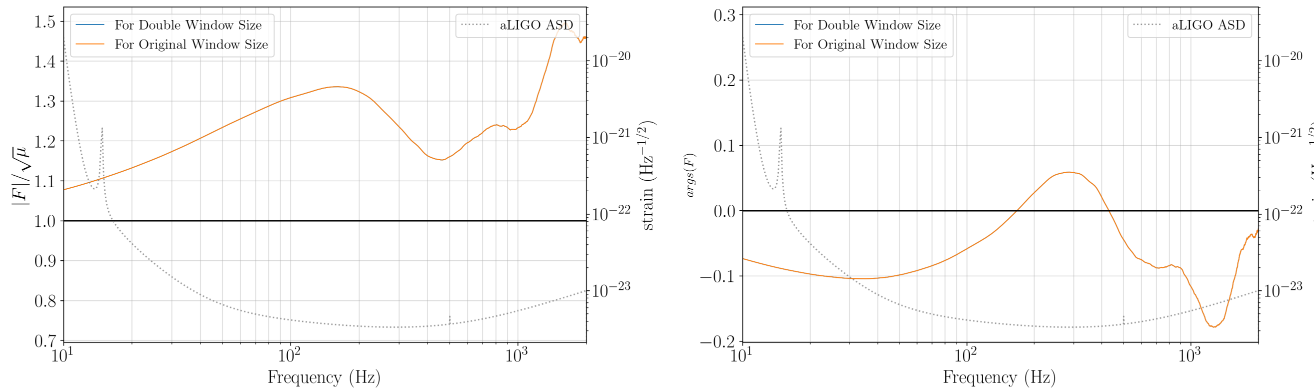

Figure 8.30: Amplification Factor Graphs for $\eta_{SIS} = [0.03]\theta_{SIS}$ for different distributions

The plots below show the amplitude and phase variation of Amplification factor for the setup described in section 6.2.2 for density = 90 $M_{\odot}/\mathrm{pc}^2$ and source position = $\eta_{SIS} = [0.1]\theta_{SIS}$.

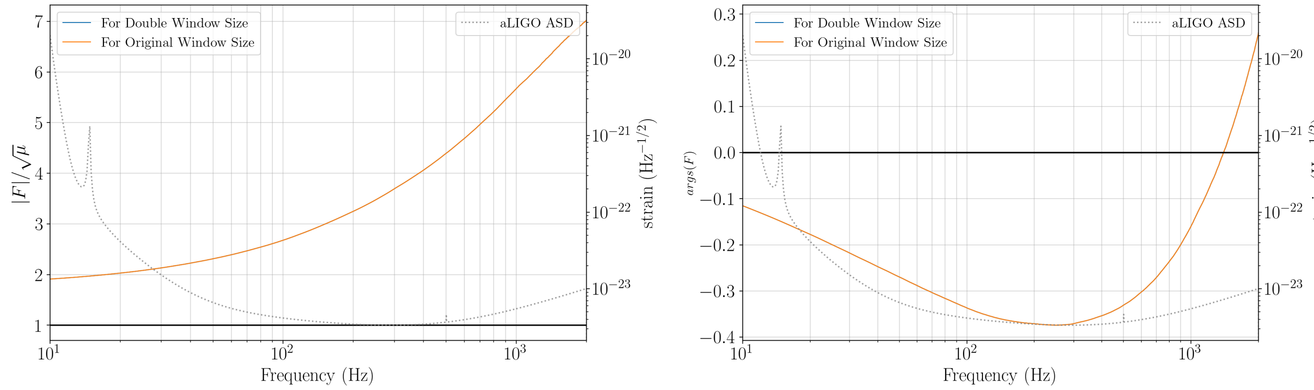

The plots below show the amplitude and phase variation of Amplification factor for Scalo IMF for the setup described in section 6.2.2. (Thus corresponding density and source position are 90 $M_\odot/\mathrm{pc}^2$, $\eta_{SIS} = [0.1]\theta_{SIS}$)

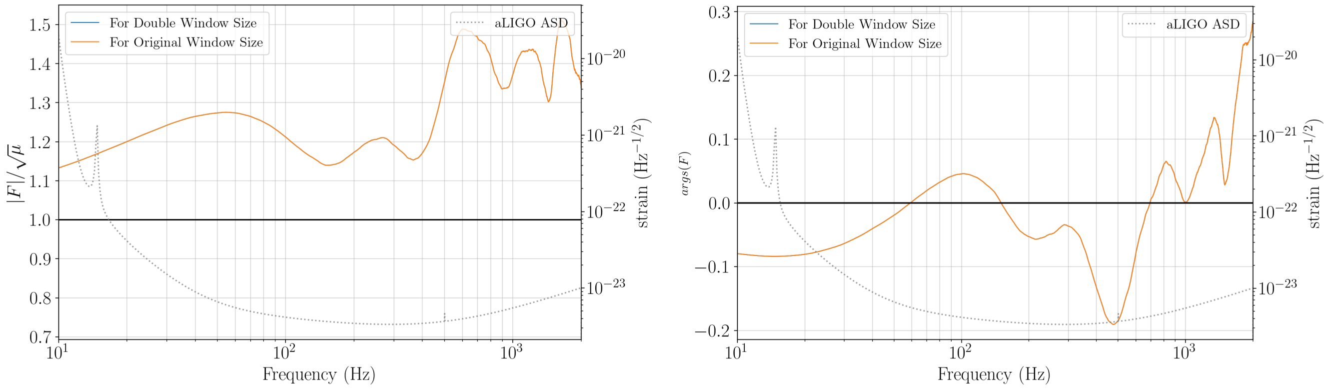

Figure 8.32: The three panels above show amplification factor graphs for different window sizes for respective setups described.

8.6 Variation with the number of lenses

Following (8.33) are the graphs for the amplitude $|F|$ normalised by the strong amplification $\sqrt{\mu}$ and the corresponding phase $args(F)$, varying with frequency for the setup used in section 6.2.1, but now for 300 lenses (in place of 200 lenses used originally).
The corresponding trends for the variation of the phase and amplitude can be described using the same reasoning as discussed in section 6.2.1 therefore, 200 lenses have been used throughout the thesis for the computational efficiency.

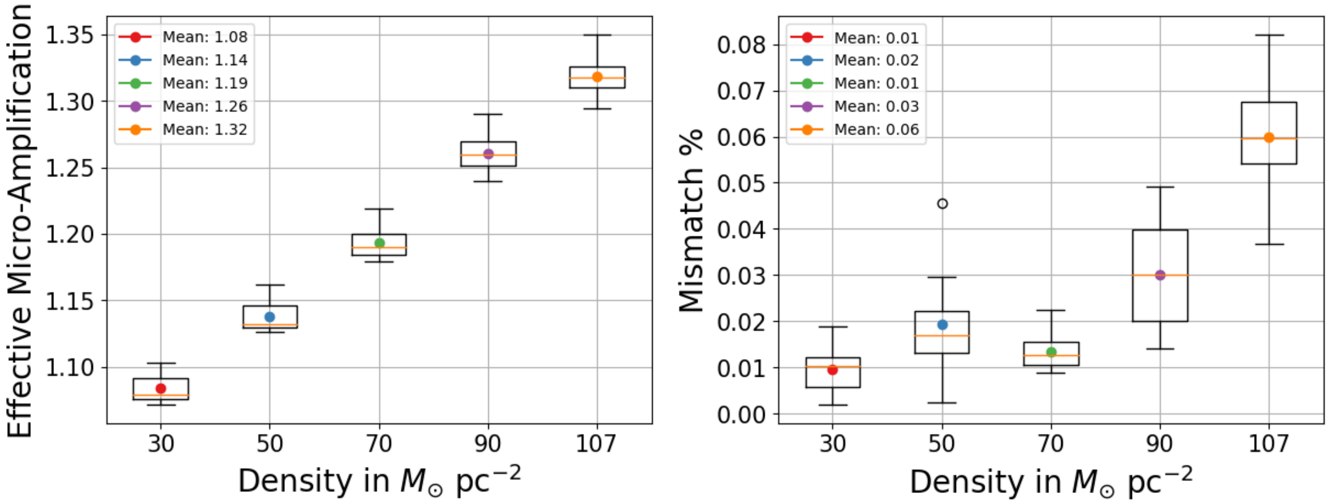

Figure 8.33: Box plot for the variation of effective micro-amplification and mismatch for 300 lenses.

8.7 Link for the main code scripts used for the computation throughout the thesis

The main code scripts used for the computation are available in attached link:
url: `https://colab.research.google.com/drive/1Hw5J9fLL865FusKeha7Mf61nORuUwtrB?usp=sharing`

Bibliography

[1] S. Rowan and J. Hough, "The detection of gravitational waves," in *1998 European School of High-Energy Physics*, pp. 301–311, 1998.

[2] "Gravitational waves in general relativity, VII. waves from axi-symmetric isolated system," *Proceedings of the Royal Society of London. Series A. Mathematical and Physical Sciences*, vol. 269, pp. 21–52, Aug. 1962.

[3] R. A. Hulse and J. H. Taylor, "Discovery of a pulsar in a binary system," *The Astrophysical Journal*, vol. 195, p. L51, Jan. 1975.

[4] B. Abbott, R. Abbott, T. Abbott, M. Abernathy, and F. A. et al, "Observation of gravitational waves from a binary black hole merger," *Physical Review Letters*, vol. 116, feb 2016.

[5] LIGO Scientific Collaboration and Virgo Collaboration, "Ligo and virgo announce four new gravitational-wave detections." `https://www.ligo.org/news/images/O4start.pdf`, 2019.

[6] T. L. S. Collaboration, J. Aasi, B. P. Abbott, R. Abbott, and T. A. et al, "Advanced ligo," *Classical and Quantum Gravity*, vol. 32, p. 074001, mar 2015.

[7] J. B. Hartle, "Gravity: an introduction to einstein's general relativity," 2003.

[8] A. K. Meena and J. S. Bagla, "Gravitational lensing of gravitational waves: wave nature and prospects for detection," *Monthly Notices of the Royal Astronomical Society*, vol. 492, pp. 1127–1134, dec 2019.

[9] S. M. Carroll, "Lecture notes on general relativity," 1997.

[10] K. Kuijken, "The basics of lensing," 2003.

[11] G. Pagano, O. A. Hannuksela, and T. G. F. Li, "LENSINGGW: a PYTHON package for lensing of gravitational waves," *Astronomy &amp Astrophysics*, vol. 643, p. A167, Nov. 2020.

[12] J. M. Diego, O. A. Hannuksela, P. L. Kelly, G. Pagano, T. Broadhurst, K. Kim, T. G. F. Li, and G. F. Smoot, "Observational signatures of microlensing in gravitational waves at LIGO/virgo frequencies," *Astronomy &amp Astrophysics*, vol. 627, p. A130, jul 2019.

[13] P. Schneider, J. Ehlers, and E. E. Falco, *Gravitational Lenses.* Springer Berlin Heidelberg, 1992.

[14] O. A. Hannuksela, T. E. Collett, M. Çalışkan, and T. G. F. Li, "Localizing merging black holes with sub-arcsecond precision using gravitational-wave lensing," *Monthly Notices of the Royal Astronomical Society*, vol. 498, pp. 3395–3402, Aug. 2020.

[15] S.-S. Li, S. Mao, Y. Zhao, and Y. Lu, "Gravitational lensing of gravitational waves: a statistical perspective," *Monthly Notices of the Royal Astronomical Society*, vol. 476, pp. 2220–2229, feb 2018.

[16] K. K. Ng, K. W. Wong, T. Broadhurst, and T. G. Li, "Precise LIGO lensing rate predictions for binary black holes," *Physical Review D*, vol. 97, jan 2018.

[17] M. Oguri, "Effect of gravitational lensing on the distribution of gravitational waves from distant binary black hole mergers," *Monthly Notices of the Royal Astronomical Society*, vol. 480, pp. 3842–3855, 08 2018.

[18] R. Abbott, T. D. Abbott, and S. A. et al, "Search for lensing signatures in the gravitational-wave observations from the first half of LIGO–virgo's third observing run," *The Astrophysical Journal*, vol. 923, p. 14, dec 2021.

[19] O. A. Hannuksela, K. Haris, K. K. Y. Ng, S. Kumar, A. K. Mehta, D. Keitel, T. G. F. Li, and P. Ajith, "Search for gravitational lensing signatures in LIGO-virgo binary black hole events," *The Astrophysical Journal*, vol. 874, p. L2, mar 2019.

[20] S. Cao, J. Qi, Z. Cao, M. Biesiada, J. Li, Y. Pan, and Z.-H. Zhu, "Direct test of the flrw metric from strongly lensed gravitational wave observations," *Scientific Reports*, vol. 9, no. 1, p. 11608, 2019.

[21] P. Christian, S. Vitale, and A. Loeb, "Detecting stellar lensing of gravitational waves with ground-based observatories," *Physical Review D*, vol. 98, nov 2018.

[22] M. H. Y. Cheung, J. Gais, O. A. Hannuksela, and T. G. F. Li, "Stellar-mass microlensing of gravitational waves," *Monthly Notices of the Royal Astronomical Society*, vol. 503, pp. 3326–3336, feb 2021.

[23] A. Mishra, A. K. Meena, A. More, S. Bose, and J. S. Bagla, "Gravitational lensing of gravitational waves: effect of microlens population in lensing galaxies," *Monthly Notices of the Royal Astronomical Society*, vol. 508, pp. 4869–4886, oct 2021.

[24] A. Mishra, A. K. Meena, A. More, and S. Bose, "Exploring the impact of microlensing on gravitational wave signals: Biases, population characteristics, and prospects for detection," 2023.

[25] S. Yeung, "wolensing." `https://github.com/manchunyeung/wolensing`, 2020.

[26] C. W. Misner, K. S. Thorne, and J. A. Wheeler, *Gravitation.* San Francisco: W. H. Freeman, 1973.

[27] D. Baumann., "Cosmology. (lecture notes)," *. url: http : / / cosmology . amsterdam / education/cosmology/.*

[28] N. Aghanim and Y. A. et al, "iplanck/i2018 results," *Astronomy &amp Astrophysics*, vol. 641, p. A6, Sept. 2020.

[29] M. Meneghetti, “Introduction to gravitational lensing,” *Springer*, 2021.

[30] O. Arthur, “Gravitational lensing of gravitational waves: Theoretical review and identification with deep learning.” `https://matheo.uliege.be/bitstream/2268.2/14778/4/Master_Thesis_Offermans2022.pdf`, 2022.

[31] R. D. Blandford and R. Narayan, “Cosmological applications of gravitational lensing,” *Annual Review of Astronomy and Astrophysics*, vol. 30, pp. 311–358, Sept. 1992.

[32] R. Narayan and M. Bartelmann, “Lectures on gravitational lensing,” 1996.

[33] R. Takahashi and T. Nakamura, “Wave effects in the gravitational lensing of gravitational waves from chirping binaries,” *The Astrophysical Journal*, vol. 595, pp. 1039–1051, oct 2003.

[34] A. Le Tiec and J. Novak, “Theory of gravitational waves,” 07 2016.

[35] M. Maggiore, *Gravitational Waves. Vol. 1: Theory and Experiments.* Oxford University Press, 2007.

[36] A. Buonanno, L. E. Kidder, and L. Lehner, “Estimating the final spin of a binary black hole coalescence,” *Physical Review D*, vol. 77, jan 2008.

[37] B. P. Abbott, R. Abbott, and T. D. A. et al., “GW170817: Observation of gravitational waves from a binary neutron star inspiral,” *Physical Review Letters*, vol. 119, Oct. 2017.

[38] B. A. et al., “The basic physics of the binary black hole merger GW150914,” *Annalen der Physik*, vol. 529, p. 1600209, oct 2016.

[39] V. Ferrari and L. Gualtieri, “Quasi-normal modes and gravitational wave astronomy,” *General Relativity and Gravitation*, vol. 40, pp. 945–970, jan 2008.

[40] soundsofspacetime, “soundsofspacetime.” `https://www.soundsofspacetime.org/coalescing-binaries.html`, visited, 2023.

[41] C. Garcí a-Quirós, M. Colleoni, S. Husa, H. Estellés, G. Pratten, A. Ramos-Buades, M. Mateu-Lucena, and R. Jaume, “Multimode frequency-domain model for the gravitational wave signal from nonprecessing black-hole binaries,” *Physical Review D*, vol. 102, sep 2020.

[42] M. Maggiore, *Gravitational Waves. Vol. 2: Astrophysics and Cosmology.* Oxford University Press, 3 2018.

[43] R. S. Shankland, “The michelson-morley experiment,” *Scientific American*, vol. 211, no. 5, pp. 107–115, 1964.

[44] C. Lab. `https://www.ligo.caltech.edu/system/media_files/binaries/237/original/Basic_michelson_labeled.jpg?1435862648`, visited, 2023.

[45] C. J. Moore, R. H. Cole, and C. P. L. Berry, “Gravitational-wave sensitivity curves,” *Classical and Quantum Gravity*, vol. 32, p. 015014, dec 2014.

[46] C. Cahillane and G. Mansell, “Review of the advanced LIGO gravitational wave observatories leading to observing run four,” *Galaxies*, vol. 10, p. 36, Feb. 2022.

[47] K. Somiya, “Detector configuration of KAGRA–the japanese cryogenic gravitational-wave detector,” *Classical and Quantum Gravity*, vol. 29, p. 124007, jun 2012.

[48] Y. Aso, Y. Michimura, K. Somiya, M. Ando, O. Miyakawa, T. Sekiguchi, D. Tatsumi, and H. Yamamoto, “Interferometer design of the KAGRA gravitational wave detector,” *Phys. Rev. D*, vol. 88, no. 4, p. 043007, 2013.

[49] T. Akutsu, M. Ando, S. Araki, and A. A. et al, “Construction of KAGRA: an underground gravitational-wave observatory,” *Progress of Theoretical and Experimental Physics*, vol. 2018, jan 2018.

[50] C. S. Unnikrishnan, “IndIGO and LIGO-India: Scope and plans for gravitational wave research and precision metrology in India,” *Int. J. Mod. Phys. D*, vol. 22, p. 1341010, 2013.

[51] A. L. Tiec and J. Novak, “Theory of gravitational waves,” in *An Overview of Gravitational Waves*, pp. 1–41, WORLD SCIENTIFIC, feb 2017.

[52] K. Haris, A. K. Mehta, S. Kumar, T. Venumadhav, and P. Ajith, “Identifying strongly lensed gravitational wave signals from binary black hole mergers,” 2018.

[53] A. K. Li, R. K. Lo, S. Sachdev, J. Chan, E. Lin, T. G. Li, and A. J. Weinstein, “Targeted subthreshold search for strongly lensed gravitational-wave events,” *Physical Review D*, vol. 107, jun 2023.

[54] B. P. Abbott, R. Abbott, and T. D. A. et al, “GWTC-1: A gravitational-wave transient catalog of compact binary mergers observed by LIGO and virgo during the first and second observing runs,” *Physical Review X*, vol. 9, sep 2019.

[55] M. A. Varvella, M. C. Angonin, and P. Tourrenc, “Increase of the number of detectable gravitational waves signals due to gravitational lensing,” *General Relativity and Gravitation*, vol. 36, pp. 983–999, May 2004.

[56] T. T. Nakamura and S. Deguchi, “Wave Optics in Gravitational Lensing,” *Prog. Theor. Phys. Suppl.*, vol. 133, pp. 137–153, 1999.

[57] C. Baraldo, A. Hosoya, and T. T. Nakamura, “Gravitationally induced interference of gravitational waves by a rotating massive object,” *Physical Review D*, vol. 59, Mar. 1999.

[58] R. Blandford and R. Narayan, “Fermat's principle, caustics, and the classification of gravitational lens images,” *The Astrophysical Journal*, vol. 310, p. 568, Nov. 1986.

[59] L. Dai and T. Venumadhav, “On the waveforms of gravitationally lensed gravitational waves,” 2017.

[60] J. M. Ezquiaga, D. E. Holz, W. Hu, M. Lagos, and R. M. Wald, “Phase effects from strong gravitational lensing of gravitational waves,” *Physical Review D*, vol. 103, mar 2021.

[61] M. Vogel, "Astrophysics in a nutshell (2nd edition), by dan maoz," *Contemporary Physics*, vol. 58, pp. 193–193, Feb. 2017.

[62] K. R. Lang and K. R. Lang, *Essential astrophysics.* Springer, 2013.

[63] P. Jain, *An introduction to astronomy and astrophysics.* CRC Press, 2016.

[64] G. Chabrier, "The galactic disk mass budget. i. stellar mass function and density," *The Astrophysical Journal*, vol. 554, pp. 1274–1281, June 2001.

[65] T. Treu, M. W. Auger, L. V. E. Koopmans, R. Gavazzi, P. J. Marshall, and A. S. Bolton, "THE INITIAL MASS FUNCTION OF EARLY-TYPE GALAXIES," *The Astrophysical Journal*, vol. 709, pp. 1195–1202, Jan. 2010.

[66] A. Sonnenfeld, A. T. Jaelani, J. Chan, A. More, S. H. Suyu, K. C. Wong, M. Oguri, and C.-H. Lee, "Survey of gravitationally-lensed objects in HSC imaging (SuGOHI)," *Astronomy &amp Astrophysics*, vol. 630, p. A71, Sept. 2019.

[67] P. Kroupa, "On the variation of the initial mass function," *Monthly Notices of the Royal Astronomical Society*, vol. 322, pp. 231–246, apr 2001.

[68] G. Chabrier, "Galactic stellar and substellar initial mass function," *Publications of the Astronomical Society of the Pacific*, vol. 115, pp. 763–795, jul 2003.

[69] G. Chabrier, "The galactic disk mass budget. ii. brown dwarf mass function and density," *The Astrophysical Journal*, vol. 567, no. 1, p. 304, 2002.

[70] T. Maschberger, "On the function describing the stellar initial mass function," *Monthly Notices of the Royal Astronomical Society*, vol. 429, pp. 1725–1733, dec 2012.

[71] R. P. Brent, "An algorithm with guaranteed convergence for finding a zero of a function," *The computer journal*, vol. 14, no. 4, pp. 422–425, 1971.

[72] P. L. Kelly, J. M. Diego, S. Rodney, N. Kaiser, T. Broadhurst, A. Zitrin, T. Treu, P. G. Perez-Gonzalez, T. Morishita, M. Jauzac, J. Selsing, M. Oguri, L. Pueyo, T. W. Ross, A. V. Filippenko, N. Smith, J. Hjorth, S. B. Cenko, X. Wang, D. A. Howell, J. Richard, B. L. Frye, S. W. Jha, R. J. Foley, C. Norman, M. Bradac, W. Zheng, G. Brammer, A. M. Benito, A. Cava, L. Christensen, S. E. de Mink, O. Graur, C. Grillo, R. Kawamata, J.-P. Kneib, T. Matheson, C. McCully, M. Nonino, I. Perez-Fournon, A. G. Riess, P. Rosati, K. B. Schmidt, K. Sharon, and B. J. Weiner, "Extreme magnification of a star at redshift 1.5 by a galaxy-cluster lens," 2018.

[73] J. M. Diego, N. Kaiser, T. Broadhurst, P. L. Kelly, S. Rodney, T. Morishita, M. Oguri, T. W. Ross, A. Zitrin, M. Jauzac, J. Richard, L. Williams, J. Vega-Ferrero, B. Frye, and A. V. Filippenko, "Dark matter under the microscope: Constraining compact dark matter with caustic crossing events," *The Astrophysical Journal*, vol. 857, p. 25, Apr. 2018.

[74] M. Wright and M. Hendry, "Gravelamps: Gravitational wave lensing mass profile model selection," *The Astrophysical Journal*, vol. 935, p. 68, Aug. 2022.

[75] A. Nitz, I. Harry, D. Brown, C. M. Biwer, J. Willis, T. D. Canton, C. Capano, T. Dent, Larne Pekowsky, G. S. C. Davies, Soumi De, M. Cabero, Shichao Wu, A. R. Williamson, D. Macleod, B. Machenschalk, F. Pannarale, Prayush Kumar, S. Reyes, Dfinstad, S. Kumar, M. Tápai, L. Singer, Veronica-Villa, S. Khan, S. Fairhurst, Bhooshan Uday Varsha Gadre, P. Kumar, Koustav Chandra, and A. Nielsen, "gwastro/pycbc: v2.2.1 release of pycbc," 2023.

[76] S. Birrer, "lenstronomy." `https://github.com/sibirrer/lenstronomy`, 2018.

[77] W. Press, S. Teukolsky, W. Vetterling, and B. Flannery, "Numerical recipes 3rd edition: The art of scientific computing," 01 2007.

[78] G. Pagano, "lensinggw." `https://gitlab.com/gpagano/lensinggw`, 2020.

[79] A. Ulmer and J. Goodman, "Femtolensing: Beyond the semiclassical approximation," *The Astrophysical Journal*, vol. 442, p. 67, mar 1995.

[80] LIGO Scientific Collaboration, "Publication on O3b astrophysical distributions."

[81] I. Mandel and A. Farmer, "Merging stellar-mass binary black holes," *Physics Reports*, vol. 955, pp. 1–24, apr 2022.

[82] G. E. Miller and J. M. Scalo, "The initial mass function and stellar birthrate in the solar neighborhood," *The Astrophysical Journal Supplement Series*, vol. 41, p. 513, Nov. 1979.

[83] G. Chabrier, "Galactic stellar and substellar initial mass function," *Publications of the Astronomical Society of the Pacific*, vol. 115, pp. 763–795, July 2003.

Department of Physics and Astronomy
Celestijnenlaan 200 D - bus 2412
3001 LEUVEN, BELGIË
tel. + 32 16 32 71 24
www.kuleuven.be